1996

Growth and Properties of Chemically Deposited CdS Thin Films

Edward A. Gluszak
Edith Cowan University

Edith Cowan University

Copyright Warning

GROWTH AND PROPERTIES OF CHEMICALLY DEPOSITED CdS THIN FILMS

A Thesis submitted to the

Faculty of Science, Technology & Engineering

Edith Cowan University

Perth, Western Australia

by

Edward A. Gluszak

In Fulfilment of the

Requirements for the Degree

of

Bachelor of Science Honours (Physical Sciences)

November 1996

USE OF THESIS

The Use of Thesis statement is not included in this version of the thesis.

ABSTRACT

Polycrystalline thin films of undoped CdS and In doped CdS (i.e. CdS:In) have been deposited by chemical bath on glass slides and high purity silicon wafers. The effect of different processing conditions (e.g. substrate temperature, doping and air annealing) on film growth, optical transmittance and electrical properties were correlated with the film microstrucutre.

The mechanism of chemical bath deposition of CdS thin films from the ammonia-thiourea system is studied. The influence of reaction parameters (i.e. concentration of reactants and pH) on film growth were determined and modeled. Thin film growth is thermally activated with an energy $\approx 5 \times 10^{23}$ eV·mol^{-1} where it initiates a sequential reaction mechanism. A kinetic study is presented resulting in the formulation of a growth rate formula.

As deposited CdS films exhibited high resistivities typically $\approx 10^5$ - 10^6 Ω·cm that decreased with increasing [Cd] and [TU] concentrations. Optical band gap energies of the mixture hexagonal and cubic structures were ≈ 2.46eV. The band energies were found to be proportional to [Cd] concentrations and inversely proportional to [TU] concentrations.

CdS:In films were formed by in-situ chemical doping with In ions. The resulting films revealed a more organized crystal structure than the undoped films. A comparison of the optical transmittance spectra for undoped and doped films indicated improved film crystallinity and a marginal impurity absorption band at In dopant concentrations < 10^{19} atoms·cm^{-3}. The n-type conductivities were typically ~ 0.1 Ω^{-1}·cm^{-1} (as deposited) and ~ 10 Ω^{-1}·cm^{-1} (air annealed at 200°C) band gaps differ in the range of 2.46 to 2.37 eV.

Films annealed in air at < 200°C exhibit a fast photoresponse, and a photoconductivity to dark current ratio of $\approx 10^4$. Annealed films show an optical transmittance increase of about 8 - 12% at the band edge and caused the band edge and a shift in the band edge to higher wavelengths. Optical band gaps of the films were found to decrease from 2.46 eV for (as deposited) to 2.38 eV for films annealed at 395°C for 1hr. Film resistivity decreased by a factor of ~ 10^5 as a result of impurity phases and improved crystal orientation. The higher conductivity of the air annealed films were attributed to the presence of the conducting CdO phase. XRD studies of the annealed films confirmed the presence of a mixture of CdO and $CdSO_4$ related phases.

DECLARATTION

I certify that this thesis does not incorporate without acknowledgment any material previously submitted for a degree or diploma in any institution of higher education; and that to the best of my knowledge and belief it does not contain any material previously published or written by another person except where due reference is made in the text.

Signature

Date ....28NOV96.....

ACKNOWLEDGEMENTS

First I'd like to express my profound thanks to my mentor and honours supervisor Dr. Steven Hinckley, for his support and "go hard or go home" attitude to life. His inspiring motivation has not only showed me the value of lateral thinking but also that the search for knowledge is not about grades but the search for understanding and truth.

At Curtin University of Technology I would like the opportunity to thank the Peter Chapman at the Vibrational Spectroscopy Facility, for his inspiration and access to the contained facilities. Dr. Li and Dr. Vanrissen at the Department of Physical Sciences for use of the X-ray Diffractometer and introducing me to such and powerful analytical instrument.

At the Surface Science Facility (Murdoch University), I would also like to express much thanks to the very friendly staff, higher degree students and especially Dr. Steve Thurgate and Tom for access to the Atomic Force Microscope.

Thanks is also extended to the technical staff of the Department of Applied Science, of Edith Cowan University (ML) for your support and continual encouragement.

To my family, thankyou for your patience, close support and encouragement through a demanding chapter of my degree. I can understand now that knowledge is truly the gateway to life and opportunity.

For any person reading this thesis I will end in simply stating that, Physics is the greatest science and there is not such thing as a problem that cannot be solved!

"The only easy day was yesterday!".....
Edward A. Gluszak (1996)

CONTENTS

1. INTRODUCTION

Binary II-VI semiconductors are compounds consisting of elements exclusive to groups II and VI of the Periodic Table. Cadmium Sulfide (CdS), Cadmium Selleunide (CdSe) and Cadmium Telluride (CdTe) are promising materials for a variety of optoelectronic applications, including photoconductive, photoluminescent, electroluminescent and photovoltaic devices. Semiconductor thin films possess high optical absorption coefficients (so that light can be absorbed by layers as thin as a few micrometers,) and electrical properties that can be easily controlled over a broad range by doping with impurities.

A wide range of binary II-VI semiconductors are under investigation for use in photovoltaic applications. In recent years, there has been considerable interest in II-VI semiconductors for use in the manufacture of CdS/CdTe thin film solar cells (Jayakrishnan *et al.*, 1996), CdS/InP solar cells (Saito *et al.*, 1994) and CdS/CdSe gas-sensors (Smyntyna *et al.*, 1994). CdS films have a large direct band-gap which enables a large proportion of light (>80%) to pass through the material to participate in photovoltaic conversion with either a CdTe or $CuInSe_2$ absorber layers . As a result, CdS is an ideal semiconductor windows layer competing II-VI thin film solar cell technologies.

Semiconductor materials such as CdS require particular properties for optimum solar cell performance, and hence, the choice of its use is governed by the existing processing technique and the properties that can be achieved under these conditions.

A variety of thin-film deposition techniques are suitable for producing photovoltaic device quality layers of CdS. These include spray pyrolysis, evaporation, sputtering, metallorganic chemical vapour deposition (MOCVD), chemical bath deposition (CBD), and electrodeposition (Chopra & Das, 1983). A comparison of some of these deposition techniques relative advantages and disadvantages, is shown in Table 1. Thin films prepared by these methods can differ significantly from each other in terms of their crystal structure, grain size and structural defects.

Table 1: Common Deposition processes for thin film semiconductors

Process Type	Advantages	Disadvantages
Chemical Vapour Deposition	High deposition rates; Easy to dope insitu	High substrate temperatures required; difficult to control uniformity of deposit
Sputtering	Large surface area coverage; negligible impurities due to vacuum conditions	High cost involved to operate & properly maintain equipment
Spray Pyrolysis	Uniform coverage; High deposition rates	Complex experimental setup; Difficult to maintain stoichiometry
Electrodeposition	Medium-to-high deposition rates	Requires conductive substrate; Difficult to dope with impurities
Chemical Bath Deposition	Simple setup; Uniform coverage over substrate surface	Requires post-deposition drying; Deposition rate dependent upon concentration of species

Chemical Bath Deposition (CBD), a solution growth process, allows low temperature deposition, chemical interaction with the substrate, and ionic precursor interaction. CdS films are formed through the reaction of adequately dissolved precursors, under conditions where deposition on the substrate is favoured. The unit species of the material to be deposited (Cd^{2+}) is present in ionic form (e.g. $CdAc_2$) and dispersed in a aqueous medium. This chemical immersion technique involves the dipping of the substrate into the reaction mixture for a time depending on the thickness required.

CBD is an attractive technique in this respect as it permits low temperature depositions with the added advantage of doping *in-situ*. Creating photovoltaic devices using high temperature deposition techniques such as CVD (i.e. T>400°C), allows impurities to diffuse into the film (e.g. O_2), and undesirable interactions between the substrate and the film. Annealing at high temperatures and the need to intentionally to dope the material at these temperatures may adversely affect the device performance. These drawbacks are absent in the CBD technique.

Despite the simplicity with which CdS films can be prepared using this chemical immersion technique, there has been little experimental and theoretical justification of the kinetics and growth mechanism with which these films deposit. Recent literature concerning chemical bath deposition of CdS thin films techniques and *in-situ* doping have had a more empirical approach to the solution chemistry of the deposition process. The kinetics of the deposition process and the effects of different deposition and post deposition processed on film properties have not been fully explored. This study will contribute to both the theoretical knowledge and practical aspects of the solution chemistry involved in producing quality CdS films, and at the same time, complement the study of the thin-film solid and its properties.

2. SEMICONDUCTOR PHYSICS

It is important to understand the properties of semiconductors to link theory to the applications which drive much of the research in this area. The main emphasis of this section is to review those aspects of semiconductor theory, related to the optical and electrical properties of the materials be examined.

2.1 BAND THEORY OF SEMICONDUCTORS

In quantum theory, the electron can be represented by a wavefunction, and the interaction between electrons can be predicted by interfering wavefunctions. Quantum theory predicts (and experimental observations confirm) that the electron states in atoms have discrete energy levels. When atoms are brought together to form a solid, various atomic interactions such as Coulomb repulsion/attraction and electronic wavelength overlap (interference) occur among the neigbouring atoms. The subsequent atomic forces of attraction and repulsion eventually equilibrate at a particular interatomic spacing for the crystal. This equilibrium of forces causes changes to occur in the electronic energy level configurations, which gives rise to characteristic electrical and optical properties (Streetman, 1990).

When two atoms are isolated from one another, the electronic wavefunctions can be considered as non-interacting and they will have identical electronic structures. However, as the interatomic distance is reduced, the respective wavefunctions overlap. According to the Pauli Exclusion Principle, no two electron wavefunctions can have the same quantum state. This results in a splitting of the discrete energy levels of the associated atoms into new levels as atoms are brought together. These new energy levels are exclusive to the particular atom combination (Thorton & Rex, 1993).

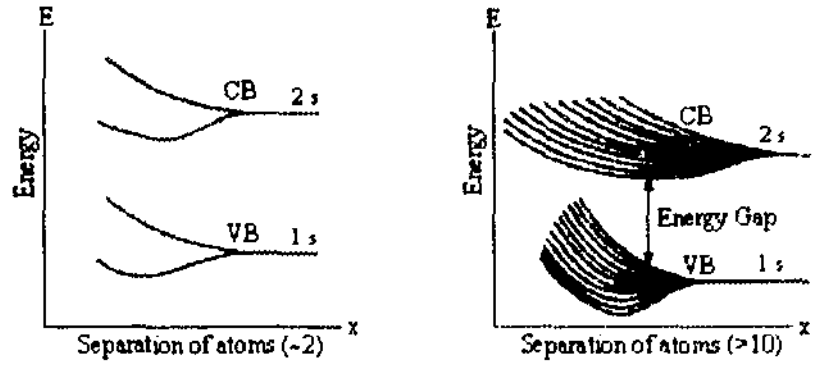

Figure 2-1 Energy level splitting vs interatomic distance between atoms

In a solid, many atoms are in close proximity, resulting in numerous splitting of the energy levels (see Figure 2-1). These new levels are so closely spaced that they appear to be continuous "bands". Any atoms joining this array brings additional electrons, each of which enters the band at a higher energy. The energy at which the last electron resides at absolute zero is called the Fermi energy (Perkowitz, 1993, p.18). This results in many energy bands, the top two of which are the most important in the conduction process.

The upper-most, band called the *conduction* band (CB), defines the allowed electron states of "free" electrons within the solid. That is, the electrons that contribute to carrier movement and current flow in the solid. These are not entirely "free", but are very loosely bound to the lattice. The lower band, called the *valence* band (VB), represents the energy states of the atomic valence electrons which form covalent bonds that define the solid. Both bands are separated by a forbidden region where there are no allowed electron states. The width of the forbidden region is called the energy bandgap (E_g), as shown in Figure 2-2.

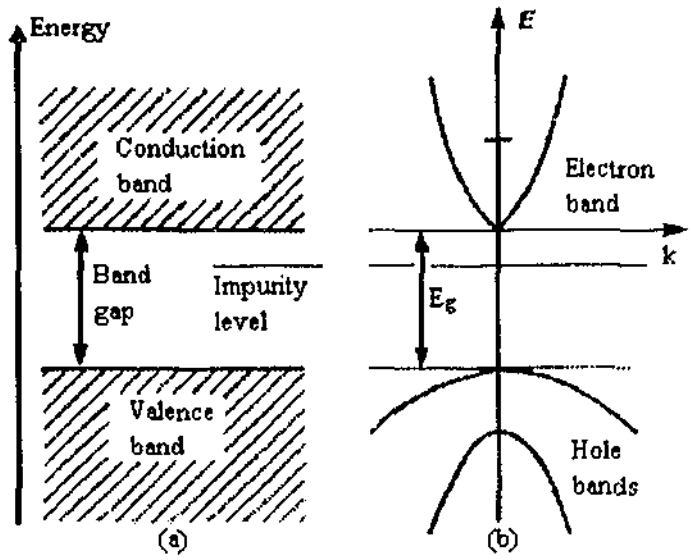

Figure 2-2 Representation of energy band structure in a semiconductor; (a) in terms of x (including an impurity level within the forbidden band) and (b) in terms of the wave vector (k).

The corresponding electronic energy band does not range from zero to the Fermi energy without quantum interference. Electrons have wavelength and direction that matches the geometric constraints of the lattice as they traverse through the structure, while others are canceled by destructive interference. These canceled wavelengths correspond to lost momenta, and hence, missing energy. It is this which creates forbidden regions or gaps in the continuous range of allowed electron energies.

Semiconductor materials at 0 Kelvin have an energy band structure similar to that of an insulator, having a filled valence band separated from a conduction band containing no filled energy states. The basic difference between insulators and semiconductors is that the forbidden bandgap (E_g) is much smaller in semiconductors than insulators. This relatively small bandgap allows the transition of electrons from the valence band to the conduction band, provided there is sufficient thermal or optical excitation energy. Therefore, in a semiconductor, the number of electrons available for conduction (i.e. electron excited to the conduction band) can be increased dramatically by thermal or optical energy. In the case of insulators, this is impossible due to the relatively large energy gap that the electrons must traverse for conduction (Streetman, 1990).

Band properties affect the optical and electrical behaviour of a semiconductor. Electrons can be elevated from the valence band to the conduction by optical excitation provided the energy of the absorbed photon (hν) is greater than or equal to the energy-gap (E_g). Since momentum (**p**) must be conserved, the absorption and emission processes near the gap are affected by whether the semiconductor is direct (vertical transition) or indirect (non vertical transition).

2.2 EFFECTIVE MASS

Those electrons that are successful in traversing to the conduction band are free to move within any applied electric field (ξ) as they will experience a force $\underline{\mathbf{F}} = q\xi = m_o\underline{\mathbf{a}}$, where q is the electron charge, m_o is the electron mass and $\underline{\mathbf{a}}$ is the acceleration vector.

Consider a non-relativistic electron moving in free space. That is, an electron moving in space without any influence of electric or magnetic fields. These free electrons have an energy-momentum relationship:

$$E = \frac{p^2}{2m_o} = \frac{\hbar^2\mathbf{k}^2}{2m_o} \qquad [2\text{-}1]$$

where the electron momentum is replaced by the quantum description given by the de Broglie relation $\mathbf{p} = \hbar\mathbf{k}$, where $\hbar = h/2\pi$, h is Planck's constant, $\mathbf{k} = 2\pi/\lambda$ is the electron wavevector, and λ is the wavelength of the wave representing the electron in the de Broglie concept. As seen in Figure 2-2(b), this results in the bands taking on a parabolic shape, in momentum or k-space.

Electrons in the conduction band of a semiconductor can be approximated as "free" since they have a similar quadratic relationship at the bottom and top of a band. However, due to the interaction with the lattice, the classical electron mass (m_o) must be replaced by an effective mass (m^*). The effective mass is not an actual mass, but describes the

interaction of an electron in a lattice including all quantum effects. The correct approach is to solve Schrodinger's Equation for all electrons and atoms in the solid, which is impossible at present. Since there are many electrons, we can use quantum statistics to look at the average behaviour, which is defined by m*.

The calculation of effective mass (m*) accounts for the shape of the energy bands in a 3-dimensional vector-space (**k**), taking appropriate averages over the various energy bands. The electron mass is inversely related to the curvature (2nd derivative) of the $E(\mathbf{k})$ relationship [2-1]:

$$\frac{d^2E}{d\mathbf{k}^2} = \frac{\hbar^2}{\mathrm{m}} \qquad [2\text{-}2]$$

Although electrons in solids are not free, the energy bands are generally parabolic at their extrema (i.e. minima for conduction bands and maxima for valence bands). The effective mass (m*) can be approximated near those band extrema from the curvature of the band. Thus the effective electronic mass (m*) in a band, given the $E(\mathbf{k})$ relationship, is:

$$m^* = \frac{\hbar^2}{d\mathbf{k}^2 / d^2E} = \hbar^2\left(\frac{d^2E}{d\mathbf{k}^2}\right)^{-1} \qquad [2\text{-}3]$$

Hence, substituting m* for m_o results in the energy-wavevector quantum relationship:

$$\mathrm{E} = \frac{p^2}{2m^*} = \frac{\hbar^2\mathbf{k}^2}{2m^*} \qquad [2\text{-}4]$$

The effective mass (representing the average of all the quantum effects), allows us to use Newtonian mechanics to explain the motion of carriers in semiconductors under the influence of applied or internal electric and magnetic fields.

2.3 HOLES

The motion of charged particles is not confined to the conduction band. An electron promoted from the valence band leaves behind an empty state, or an effective positive charge, which moves opposite to the electron when an electric field is applied. This resulting empty state, known as a *hole* (h$^+$), also contributes to the electrical behaviour of the semiconductor (Perkowitz, 1993, pg.18). This is conveniently illustrated by the electron and hole $E(\mathbf{k})$ parabolas shown in Figure 2-2. If the conduction band electrons and the valence band holes are created by the excitation of a valence band electron to the conduction band, they are called an electron-hole pair (EHP).

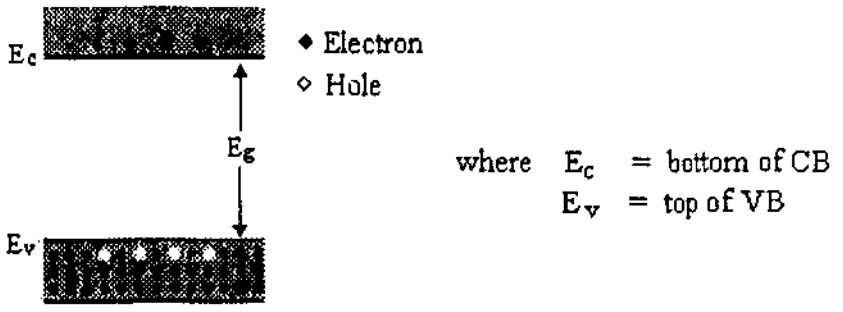

Figure 2-3 Electron-hole pair production in a semiconductor.

A more rigorous explanation of the hole concept is obtained by looking at the curvature of the E(**k**) diagram. Here $\frac{d^2E}{d\mathbf{k}^2}$ is negative for the valence band maxima and positive for the conduction band minima. Hence, the electrons near the top of the valence band must have *negative effective mass* according to Equation.[2-4]. This concept can be simplified by stating that valence band electrons with negative mass (-m*) and negative charge move under an electrical field in the same direction as holes with positive mass and positive charge. (i.e $e^- \equiv (m, -q) \Leftrightarrow h^+ \equiv (+m, +q)$)

2.4 INTRINSIC & EXTRINSIC SEMICONDUCTORS

Intrinsic semiconductors are perfect semiconductor crystals with no impurities or lattice defects. In such materials, there are no charge carriers at 0 Kelvin, since the valence band is filled with electrons and the conduction band is empty. At higher temperatures, electron-hole pairs are generated as valence band electrons are thermally excited across the band gap to the conduction band. It is these electron hole pairs that form the charge carriers in intrinsic materials (Streetman, 1990, pg. 65).

Since the electrons and holes are created in pairs, the conduction band electron concentration (n) equals the valence band hole concentration (p). For convenience this is called the intrinsic carrier concentration (n_i); that is, $n_i = n = p$ in an intrinsic semiconductor. If the semiconductor is subject to thermal excitation, the carrier concentration varies as a function of temperature as shown in Figure 2-4.

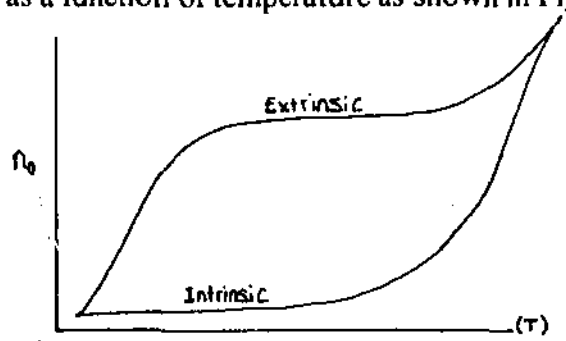

Figure 2-4 Carrier concentration vs temperature in intrinsic and extrinsic semiconductors

Additional charge carriers can be created by the introduction of impurity atoms into the crystal. This *doping* process is an effective technique of tailoring the electrical properties of a semiconductor. By doping, a crystal can be altered so that it has a predominance of either electrons or holes as charge carriers. As a consequence, there are two types of doped semiconductors; n-type where the majority of carriers are electrons, and p-type where the majority of carriers are holes. When a crystal is doped such that the "equilibrium" (or steady state) carrier concentrations (n_o , p_o) are different from the intrinsic carrier concentration(n_i), the material is called *extrinsic*.

The introduction of impurities or lattice defects into a perfect crystal causes additional energy levels to be created in the energy band structure, usually within the forbidden energy gap. For example, doping a group IV semiconductor (such as silicon, Si) with group V atoms (P, As or Sb), creates a defect energy level close to the conduction band within the forbidden energy gap. This particular energy level is filled with electrons at 0 Kelvin, and requires little thermal energy to excite electrons across the reduced energy gap to the conduction band (Figure 2-5). These impurities are therefore conveniently known as *donor* atoms. Thus an n-type material is a semiconductor doped with a significant number of donor atoms, having an equilibrium majority carrier concentration $n_o \gg (n_i , p_o)$ at room temperature.

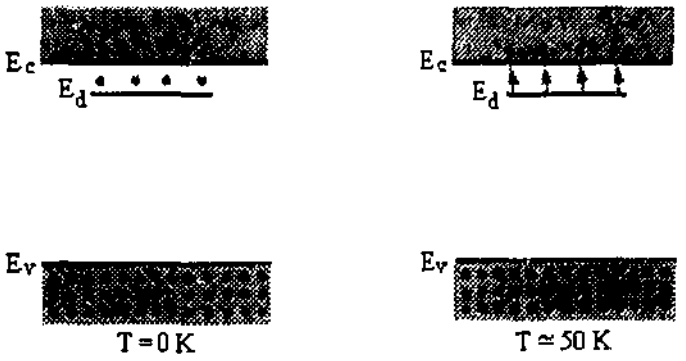

Figure 2-5 Donor energy level: (a) at 0 K and (b) its effect at T > 0 K

Similarly, group III atoms (B, Al, Ga or In) introduce energy levels close to the valence band in group IV semiconductors. At low temperatures, electrons from the valence band are thermally excited and accepted into the impurity level leaving a vacancy or hole in the valence band (Figure 2-6). These impurities are therefore known as *acceptor* atoms. Hence doping a semiconductor with acceptor atoms causes the hole carrier concentration (p_o) to be greater than the conduction band electron concentration(n_o), and is known as a p-type material (Streetman, 1990). The majority carrier concentration for an extrinsic material as a function of temperature (see Figure 2.4) is different to that of intrinsic materials.

The situation is slightly more complex in a binary semiconductor (such as CdS), compared to elemental semiconductors (such as Si), because the presence of two atoms (i.e. Cd & S) with different valence states.

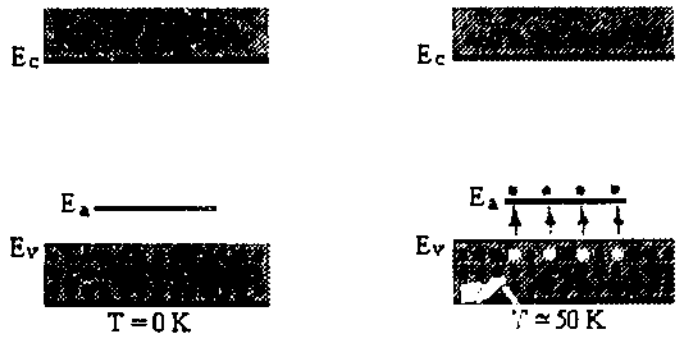

Figure 2-6 Acceptor energy level: (a) at 0 K and (b) its effect at T > 0 K

2.5 CARRIER GENERATION & RECOMBINATTION

In equilibrium, without any applied electric field (ξ), there will be no current flow. In a semiconductor there is a certain concentration of electron-hole pairs (n_i) at a given temperature. This steady carrier concentration is maintained by *recombination* of electron hole pairs at the same rate as they are generated. The generation-recombination of excess carriers in the conduction band via optical or thermal excitation energy (Figure 2-7) is the basis of carrier transport in semiconductor devices.

The recombination process occurs when an electron in the conduction band makes a transition to a hole in the valence band. This hole may have been generated as a result of thermal or optical energy exciting a valence band electron to either a defect state or the conduction band, as shown in figure 2-7(a). If the generation rate of electron hole pairs is defined as g_i (in EHP/cm^2-s) and recombination rate as r_i, then at equilibrium these must be equal. Since both rates are temperature dependent, we can write:

$$g_i(T) = r_i(T) \qquad [2\text{-}5]$$

When the temperature is increased, $g_i(T)$ increases and a new carrier concentration (n_i) is formed, so that a higher recombination rate $r_i(T)$ results to balance the generation. The

rate of recombination of holes (p_o) and electrons (n_o) is proportional to the number of carriers present, can be predicted in relation to the equilibrium intrinsic carrier concentration (n_i) according to:

$$r_i = g_i = \alpha_r n_o p_o = \alpha_r n_i^2 \qquad [2\text{-}6]$$

where α_r is a proportionality constant depending upon the type of transition (direct or indirect).

Electrons in the conduction band can make transitions to the valence band (i.e recombine with holes in the valence band) directly or indirectly. In direct recombination (Figure 2-7(b)), excess electrons and holes decay by electrons falling from the conduction band to empty states or holes (h^+) in the valence band. In doing so, energy is lost by the electron as a photon. Direct recombination is a *spontaneous* process; that is, the probability that an electron and a hole will recombine is constant with time.

However, with indirect recombination (Figure 2-7(c)), a majority of the recombination events occur via recombination levels within the forbidden bandgap (i.e. at some energy-level E_t). The resulting energy loss by recombining electrons is given up as heat to the lattice. Impurities or lattice defects serve as recombination centers, capable or receiving one type of carrier and capturing the other, thereby annihilating the pair.

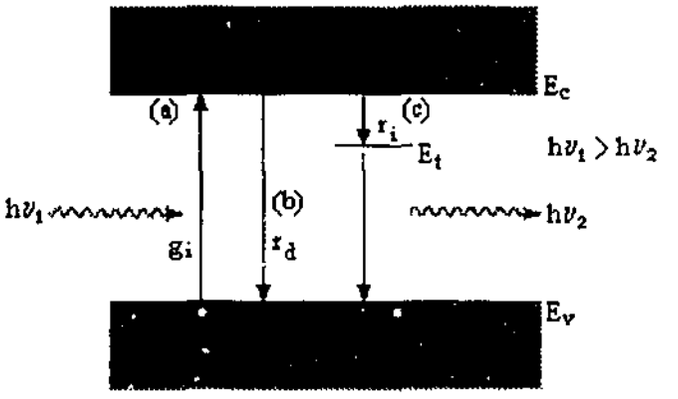

Figure 2-7 EHP generation-recombination processes: (a) optical excitation, (b) direct band-to-band recombination & (c) indirect recombination

This time-independent recombination probability leads us to expect an exponential temporal decay of the excess carriers. The decay rate of electrons at any time (t) is proportional to the number of electrons remaining at t with some constant of proportionality for recombination (α_r). The net rate of change of the conduction band electron concentration (n_o) is determined by the thermal generation rate ($\alpha_r n_i^2$) less the recombination rate, according to:

$$\frac{dn(t)}{dt} = \alpha_r n_i^2 - \alpha_r n(t)p(t) \qquad [2\text{-}7]$$

If the initial excess of electron (Δn) and hole (Δp) concentrations are equal, then when they recombine in pairs, the instantaneous concentration of carriers $\delta n(t)$ and $\delta p(t)$ are also equal. As a result, the total concentration of relationship [2-7] can be written, including the equilibrium values (n_o , p_o) and the excess carrier concentrations [$\delta n(t) = \delta p(t)$], as:

$$\frac{d\delta n(t)}{dt} = \alpha_r n_i^2 - \alpha_r[n_o + \delta n(t)]\,[p_o + \delta p(t)] \qquad [2\text{-}8a]$$

$$= -\alpha_r[(n_o + p_o)\,\delta n(t) + \delta n^2(t)]$$

If there are small excess carrier concentrations, the $\delta n^2(t)$ term can be neglected. Also, if the material is an extrinsic n-type material ($n_o \gg p_o$), the equilibrium minority carriers can be neglected, so that equation [2-8a] becomes:

$$\frac{d\delta n(t)}{dt} = -\alpha_r(n_o)\delta n(t) \qquad [2\text{-}8b]$$

The solution of this equation results is an exponential decay of the initial excess carrier concentration $\Delta n(0) = \Delta n(t)$ at t=0, given by:

$$\delta n(t) = \Delta n \exp(-\alpha_r n_o t) = \Delta n \exp(-t/\tau_p) \qquad [2\text{-}9]$$

where the excess holes recombine with a decay constant (or *recombination lifetime*) equal to $\tau_p = (\alpha_r n_o)^{-1}$. This is also known as the *minority carrier lifetime*. For direct recombination processes, the rates of decay of excess majority carriers and minority carriers are equal.

2.6 CONDUCTIVITY

In a semiconductor, the average momentum per electron (i.e. average $\langle p_x \rangle$ of the entire group of electrons) traveling in the x -direction is (Streetman, 1990):

$$\langle p_x \rangle = \frac{p_x}{n} = -q\,t\,\xi(x) \qquad [2\text{-}10]$$

where t is the mean free time between electron scattering events, and n is the concentration of conduction band electrons (cm^{-3}). Also, the electrons have a constant net velocity in the negative x-direction:

$$\langle V_x \rangle = \frac{\langle p_x \rangle}{m_n^*} = \frac{-qt}{m_n^*}\xi = \mu_n \xi \qquad [2\text{-}11]$$

where $\mu_n = qt/m_n^*$ is the *electron mobility*, which describes the ease with which the carriers drift through the material.

The electron drift current density resulting from a net drift of carriers due to an electric or "drift " field (ξ) is determined by the number of electrons crossing a unit area per unit time ($n\langle V_x \rangle$) multiplied by the charge on the electron ($-q$); i.e.

$$J_n = -qn\langle V_x \rangle = \frac{nq^2 t}{m_n^*}\xi = qn\mu\xi \qquad [2\text{-}12]$$

According to Ohm's Law, the conductivity (σ, units of Ω-cm^{-1}) can be written as:

$$\sigma_n = \frac{nq^2 t\xi}{m_n^*} = qn\mu_n \qquad [2\text{-}13]$$

Hence, assuming electron carriers (n), the electron current density at any position x in the semiconductor can be written in terms of mobility as:

$$J_n(x) = \sigma_n \xi(x) = qn\mu_n \xi(x) \qquad [2\text{-}14]$$

The above analysis also holds if holes are present. If holes are the majority charge carriers, the hole drift current density is:

$$J_p(x) = \sigma_p \xi_x = qp\mu_p \xi_x \qquad [2\text{-}15]$$

If both electrons and holes participate in the conduction process, then: the total current density in the sum of the electron and hole contributions:

$$\begin{aligned} J(x) &= J_n + J_p = \sigma\xi \\ &= q(\mu_n n + \mu_n p) \end{aligned} \qquad [2\text{-}16]$$

where $\sigma = \sigma_n + \sigma_p$ is the total conductivity.

Consider a block of uniform semiconductor material of width w, length L and thickness t, as shown in Figure 2-8. The applied potential difference V, within the material is related to the electric field by:

$$\xi = \frac{V}{L} \qquad [2\text{-}17]$$

Therefore the magnitude of the current density is:

$$J = \sigma\xi = \frac{\sigma V}{L} \qquad [2\text{-}18a]$$

Since J = I/A, where A = wt is the area of the sample, the potential difference is:

$$V = \frac{L}{\sigma} J = \left(\frac{L}{\sigma A}\right) I = IR \qquad [2\text{-}18b]$$

The resistance of the semiconductor, is then obtained by rearranging [2-18b]:

$$R = \frac{L}{\sigma A} = \frac{\rho L}{A} \qquad [2\text{-}18c]$$

where $\rho \equiv 1/\sigma$ is the resistivity (in Ω-cm) of the sample:

$$\rho = \frac{1}{\sigma} = \frac{1}{q(n\mu_n + p\mu_p)} \qquad [2\text{-}19]$$

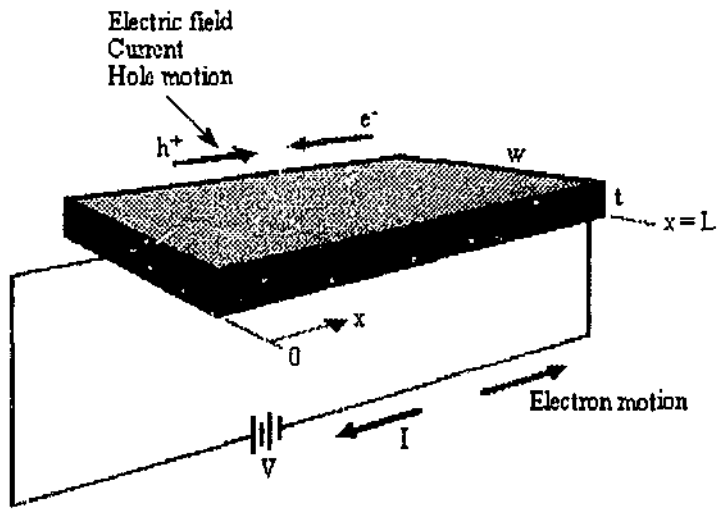

Figure 2-8 Semiconductor containing both types of carriers.

In Figure 2-8, the drift current density is constant throughout the (uniform) semiconductor slab. When an electron leaves the slab at x=0, there is a corresponding electron entering at x=L to maintain the electron concentration n. As the hole reaches the ohmic contact at x=L, it recombines with the electron supplied by the external circuit. As this hole disappears, a hole is created at x=0 in order to maintain space charge neutrality.

2.7 DIRECT AND INDIRECT SEMICONDUCTORS

In general, there are two classes of semiconductor energy transitions; *direct* and *indirect* (Figure 2-9). A simple mathematical picture of these two classes can be constructed using the wavefunction. The wavefunction $\psi_k(\underline{r})$ is assumed to be a plane wave moving with respect to the x-coordinate with a propagation constant or wave vector (**k**). This movement can be represented by the space-dependent wave function of the electron:

$$\Psi(r,t) = \psi_k(\underline{r}).f(t)$$

where $\psi(\underline{r})$ ~ is the wavefunction spatial dependence and f(t) ~ is the wavefunction time dependence. In a crystal lattice, the space dependent wavefunction can be written using Bloch's Theorem (Boer, 1990) as:

$$\psi_k(r) = U(\underline{k},\underline{r})\exp(i\underline{k}\bullet\underline{r}) \qquad [2\text{-}20]$$

where the function $U(\underline{k},\underline{r})$ modulates the wavefunction according to the periodicity of the lattice. This description enables allowed values of energy (E) to be plotted against the propagation constant **k**.

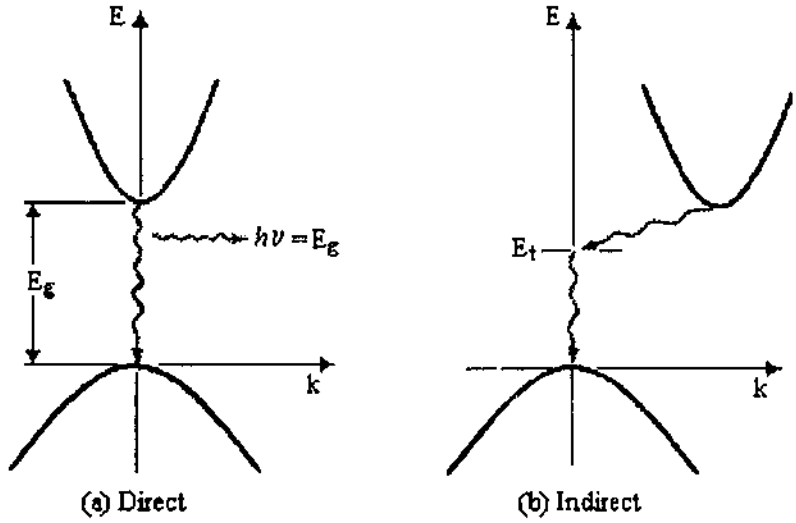

Figure 2-9 Plot of E(k) relationship for direct and indirect electron transitions in semiconductors

In *direct* semiconductors, such as CdS, an electron in the conduction band can fall into a hole in the *valence band*, emitting a photon of the energy difference (E_g). However, for an *indirect semiconductor*, the electron is incapable of the direct transition and must undergo a momentum change, and hence an energy change through some defect state. Indirect transitions (which involve a change in **k**), generally forfeit the energy as heat to the lattice (Streetman, 1990, pg. 57). In optoelectronic applications such as semiconductor lasers, it is required that the semiconductors are capable of direct band-to-band transitions or indirect with vertical transitions between suitable defect states. The beauty of CdS is that it is a direct semiconductor, which offers a wide range of uses.

The bandgap energy of a semiconductor can be determined from the absorption of incident photons on the material. Since photons with energies greater than the bandgap energy are absorbed, while photons (light) with energies less than the bandgap are transmitted, determination of the absorption coefficient (α) and forbidden energy-gap (E_g) is possible by measuring the transmittance of light through the semiconductor as a function of wavelength,

Incident photon energies $h\nu \geq E_g$ are absorbed, since there are numerous valence band electrons and the conduction band contains many empty states into which these electrons can be excited. A photon with energy $h\nu < E_g$ is unable to excite a valence band electron to the conduction band. Thus, for pure (*intrinsic*) semiconductors, there is negligible absorption of photons with $h\nu < E_g$. This explains why some semiconductors are transparent in certain wavelength (λ) ranges. For example, CdS with a bandgap of roughly 2.4 eV (i..e. $\lambda \approx 500$nm), is transparent over the infra-red region down to about the green portion of the visible spectrum.

When a beam of photons with $h\nu \geq E_g$ is incident on a semiconductor, there is some predictable absorption, determined by the properties of the material. There is a dependence of the ratio of transmitted to incident photon intensity that depends on photon

wavelength and thickness of the material. This dependence, known as the Beer-Lambert Law (Skoog, 1990), can be shown as:

$$\frac{-d\Phi(x)}{dx} = \alpha\Phi(x) \qquad [2\text{-}21]$$

where the absorption of a semiconductor is directly related to the absorption coefficient $\alpha(\lambda)$ (in cm^{-1}) and the incident photon intensity Φ_o (in photons/cm^2-s) at constant wavelength (λ). The solution to this dependence gives:

$$\Phi(x) = \Phi_o \exp[-\alpha(\lambda)x] \qquad [2\text{-}22]$$

An experiment based upon this relationship will enable the determination of the absorption coefficient (α), which is important for the determination of other optical properties.

The fundamental absorption process, where an electron is excited from the valence band to the conduction band, is affected by whether the energy-gap transition is direct or indirect. In a direct semiconductor, when an electron at the valence band maximum executes a vertical transition to the conduction band minimum, energy is conserved according to:

$$h\nu = E_f - E_i \qquad [2\text{-}23]$$

where $h\nu$ is the photon (light) absorbed or emitted, E_f and E_i are the final and initial electron energy states, respectively.

Near the absorption edge, the dependence of the absorption coefficient on photon energy can be written as:

$$\alpha = \frac{A(h\upsilon - E_g)^m}{E} \qquad [2\text{-}24]$$

where E = hν is the photon energy with frequency ν, E_g is the bandgap, and m determines the type of material according to quantum selection rules. For direct transition semiconductors m = 1/2 or 3/2, and for indirect semiconductors m = 2.

2.8 SUB-BAND GAP ABSORPTION

In some cases, the fundamental absorption edge for direct band-gap semiconductors is not a sharp transition. Impurities present during the deposition process or after post-deposition processing affect the shape of the band edges of a semiconductor. The distribution of valence and conduction band states will "smear out" at the band gap edges (see Figure 2-10), creating "band tails" which effectively reduce the width of the bandgap (E_g). As a result, electron transitions between band tail states become possible (Moller, 1993). The optical bandgap in polycrystalline semiconductors have been observed with a substantial tailing of defect states.

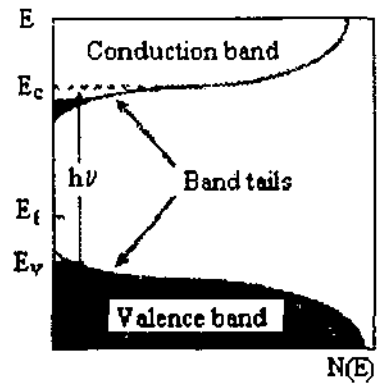

Figure 2-10 Representation of compensated semiconductor band structure showing possible transitions between tail states between the conduction and valence band edge (Moller, 1994, pg. 17).

For photon energies (hν) less than the bandgap energy (E_g), the absorption drops off slower compared to the energy dependence extrapolated from higher energies. The increased sub-band absorption is similar to the absorption in a heavily doped crystalline semiconductor and can be described by the Urbach Law (Moller, 1993):

$$\alpha_{tl}(\nu) = C(\nu) \exp\left\{-\frac{E_g - h\nu}{E_u}\right\} \qquad [2\text{-}26]$$

where C(ν) is the constant of proportionality and (E_u) is the Urbach energy parameter, which is directly related to the characteristic distribution or width of the band tail states. (Boer, 1990, pag.349)

3. CHEMICAL DEPOSITION & PROPERTIES OF CdS FILMS

Since chemical bath deposition is a growing avenue for producing device grade thin films it is important to review some of the recent findings in order to postulate on possible links to the properties which drive much of the research in this area. A summary of some related chemical bath deposition studies and processing parameters are shown in Table 3.1 and Table 3.3 respectively. The main emphasis of this section is to review previous related works and the techniques used for characterization.

3.1 EFFECT OF CdS-GROWTH ON MORPHOLOGY

The growth of chemically-deposited CdS thin films occurs as a result of both ion-by-ion condensation and colloidal particle formation of CdS adhering to the substrate surface. However, it was not known what is the dominant nature of the CdS growth. Sebastian[2] *et al.*, (1995) revealed that the particulate nature of CdS may manifest at the early developmental stage of film growth. Their study also indicated that the particulate nature of CdS films is directly related to the abundance of Cd^{2+} ions in solution. It could be postulated that the abundance of Cd^{2+} ions in solution promotes the acceleration of colloidal CdS particle formation, which both adhere to the substrate as well as precipitating out of solution. This same analogy could be applied to the release of S^{2-} anions. The structural and morphological properties (topology of surface) of chemically grown CdS determined by scanning electron microscopy (SEM) (Sebastian[2] *et al.*, 1995), have shown its importance in verifying growth theory. Part of the aims of this study is to extend this knowledge through use of atomic force microscopy.

Table 3.1 Chemical Bath Deposited CdS film - past research (Qualitative Description)

CBD Type	Description of Study	Comments	Ref. (....et al)
CdS - Dep	Modelling of the kinetics of CdS film-growth under Ammonia-Thiourea(TU) systems	Growth Kinetics of atom-by-atom growth allows quantitative descr. CdS formation differs from diss. Model; involves surface intermediate complex with $Cd(OH)_2$	Borges
	Optical, structural(XRD & ED) & electrical properties of CdS thin films	CdS film grown from iodides more transparent than chlorides. Type-A films (heterogeneous) better optoelectronic properties than type-B (homogeneous)	Nakanishi
	Thermodynamic conditions for optimum growth of chemically deposited CdS thin-films.	$Cd(OH)_2$ produced in reaction mixture forms an integral component in the development of quality thin films	Kiteav
Co-dep (CdS/CdTe) $[Cd_xS_yTe_{1-y}]$	Composition, structure and morphology of CdS/CdTe films & devices XPS, XRD & SEM	Thermal Annealing advantageous encourages CdS film regrowth	Jayakrishnan
Co-dep (CdS/ZnS) $[Cd_{1-x}Zn_xS]$	Optical and structural characterization (XPS, TEM, EDS) chemical bath co-deposited CdS-ZnS thin films	Film composition varies linearly with bath composition. ZnS Dep. process, slower & dominates	Duran

Table 3.2 CBD CdS film - past research parameters summarized

CBD Type	$[Cd^{2+}]$ Source	$[S^{2-}]$ Source	Complexing Agent	Buffering Agent	Catalyst Type	Ref. (....et al)
Co-dep (CdS/CdTe) $[Cd_xS_yTe_{1-y}]$	$CdCl_2$	TU	$[NH_4Cl]$	-	-	Jaakrishnan
Co-dep (CdS/ZnS)	$CdSO_4$	TU	$[NH_3]$	-	undef.	Dona
CdS - Dep $[Cd_{1-x}Zn_xS]$	$CdSO_4$	TU	$[NH_3]$	-	Hydrazine	Borges
CdS-dep	$Cd(Ac)_2$	TU	$[NH_4OH]$	$[NH_4Cl]$	-	Lanning
	$CdSO_4$	TU	$[NH_3]$	$[NH_4Cl]$	-	Lincot
	$CdCl_2$	TU	$[NH_4Cl]$	-	-	Nakanishi
	CdI_2	TU	$[NH_4I]$	-	-	Nakanishi
	$Cd(Ac)_2$	TU	$[NH_4OH]$	-	-	Kuranouchi
	CdX_2	TU	$[NH_3]$	-	-	Kitaev

Note: (AC) ~ Acetate (CH_3COO^-) and X ~ undefined species

3.2 STRUCTURE AND MORPHOLOGY OF CdS THIN-FILMS

The optical and electrical properties of thin-films are influenced by the crystallographic and microstructural characteristics of the film (Chopra & Kaur, 1983). The microstructure and morphology of thin-film semiconductors is dependent on a variety of parameters, such as the growth kinetics, the source of the impinging particles, chemical nature of source, and the topography of substrate surface. Also, physical properties of thin films used in device applications depend to a considerable degree on the structure of the film. It is therefore important to know how particular factors influence the structure during film growth.

Brief X-ray diffraction (XRD) studies of Sebastian[2] *et al.*, (1995) indicate that CBD CdS thin-films can contain both cubic and hexagonal crystal structure phases (see Figure 3.1). As a consequence, CdS films produced by this deposition technique, consist of a continuous part and a particulate structure and that the corresponding crystal structure includes both the cubic and hexagonal variations of CdS.

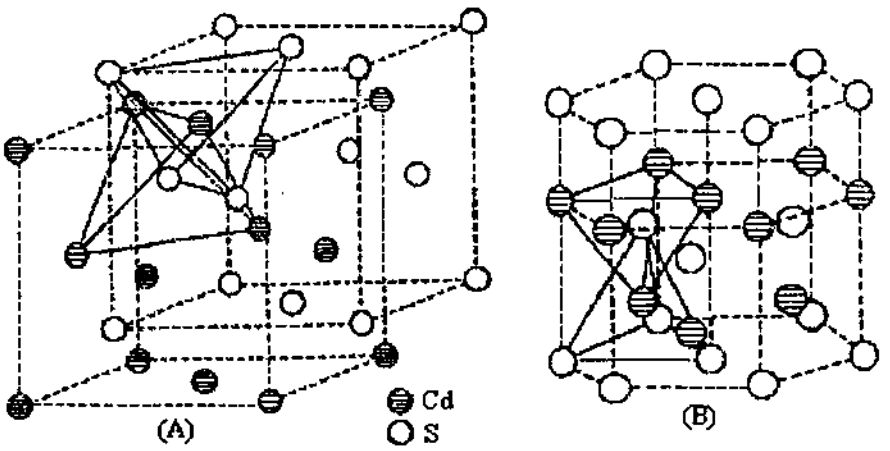

Figure 3.1 (a) Zinc-blende lattice (CdS) constructed from two interpenetrating face-centered cubic sublattices of Cd and S with a displaced origin. (b) Wurtzite lattice (CdS) constructed from two interwinned hexagonal sublattices of Cd and S.

In respect to structural variations of chemically deposited CdS films, there has been limited understanding of why both of these structures co-exist and the lack of dominance of a particular structure. To compliment previous studies (Sebastian[1-3] *et al*) , further XRD on film structure, and microscopy using AFM, will be included in this study.

3.3 INFLUENCE OF DOPING ON CdS-STRUCTURE

The structural characterization of co-deposited CdS-ZnS films (which can be written as $[Cd_{1-x}Zn_xS]$) by X-ray Diffraction, indicate that the films are more disordered after Zn-doping (Sebastian[2] *et al.*, 1995). In past publications (Chu *et al.*, 1992), the incorporation of dopants into group II-VI semiconductors have been mainly restricted to the method of application and the optoelectronic properties associated with this additive. As a result of this concentration, there has been an incomplete study of the structural significance of doping with donor and acceptor impurities on the structure and properties of CdS.

Post deposition annealing in gaseous environments have revealed, via XRD, that impurities diffuse into the film grain boundaries. The abundance of the impurity phase was found to be directly related to annealing temperature. Changes in electrical conductivity and photoresponse have been attributed to impurity phases in CdS thin films (Sebastian & Hu 1994). A decrease in film resistivity after annealing at high temperatures in air was thought to be attributed to the growth of a CdO phase in the film according to:

$$2CdS + 3O_2 \rightarrow CdO + SO_2 \qquad [3\text{-}1]$$

Additional impurities, including a sulfate phase, have been observed at annealing temperatures around 400°C. The abundance of the sulfate phase was attributed to the decomposition of $Cd_3O_2SO_4$ to $CdSO_4$ according to:

$$Cd_3O_2SO_4 \rightarrow 2CdO + CdSO_4 \qquad [3\text{-}2]$$

and

$$CdS + 2O_2 \rightarrow CdSO_4 \qquad [3\text{-}3]$$

3.4 ELECTRICAL PROPERTIES OF CdS FILMS

From a previous study (Sebastian, 1995), intrinsic CdS thin film exhibited high photosensitivity however, the films display poor dark conductivity. In addition, it was revealed that the degree of photosensitivity was directly related to the Zn-dopant concentration. Annealing the samples at temperatures in excess of 200°C also improved the dark current observed in the semiconductor. The improved photosensitivity of CdS after doping with Zn was attributed to the increase in vacancies caused by the Zn which lead to photosensitization centers in the film. The increase in dark current and annealing could be explained as being due to the loss of S atoms due to diffusion. Hence, the loss of S atoms from the film creates additional S vacancies and hence contributes to the improved dark conductivity.

4. METHOD

4.1 SUBSTRATE PREPARATION

The substrates used for deposition the deposition process were boro-silicate glass and silicon. Boro-silicate glass substrates were adopted for optical transmittance measurements and silicon wafers were used for XRD, FTIR and AFM analysis. Glass and silicon slides (75mm x 25mm x 1mm) were cleaned initially with an 60:40 mixture of reagent grade H_2SO_4 and H_2O_2 in a fume hood for > 2hrs prior to the deposition. Prior to deposition substrates were firstly cleaned ultrasonically with Milli-Q grade H_2O followed by an 80:20 mixture of ethanol and water and then air dried. The clean substrates were then mounted vertically in the reaction cell supported by the walls of the beaker by bulldog clips to which the mixture was transferred.

4.2 DEPOSITION SOLUTION AND REAGENTS

All reagents were of analytical grade and their corresponding dilution's were performed with Milli-Q grade H_2O. Deposition compounds of cadmium acetate ($Cd(CH3COO)_2$), ammonia (NH_3) ammonium acetate $NH_4(CH_3COO)_2$ and thiourea ($CS(NH_2)_2$) were purchased from SIGMA and used as received. Indium chloride ($InCl_3$) solutions that were used to dope the films were purchased from SIGMA and used as received. All participating solutions were heated to the desired reaction temperature before addition into the reaction cell.

Standard solutions of cadmium, thiourea were made by accurately dissolving the desired mass of the respective compounds in solution. Ammonia solutions of the concentrations investigated were prepared by diluting the 23% grade stock solution. Buffered Ammonia solutions were prepared in the similar fashion but with the addition of ammonium acetate salt. All stock solutions of cadmium, thiourea and ammonia were prepared by dissolving

or diluting quantities to obtain the required concentrations and their pH was modified using NaOH or HCl accordingly.

Dopant solutions of concentrations from 0.2 and 2% of total the cadmium ion concentration (i.e. 10^{15} to 10^{20} atoms·cm^{-3}) were prepared in a similar fashion.

4.3 CHEMICAL BATH DEPOSITION APPARATUS

The experimental setup constructed and used for the deposition of CdS thin films is shown in Figure 4-1. The design incorporates a 500mL heating mantle (Electrothermal) coupled to a thermocouple controlling unit (RS Model BTC-2220) and a type T Thermocouple. To avoid colloidal precipitation in the reaction cell, a mixing unit was designed and used. The unit included an a.c motor and propeller connected to a ceiling fan controller, which provides precisely defined stirring rates. The reaction cell is a modified 250mL pyrex beaker, designed to include an hexagonal outrigging to provide sufficient vertical support for 6 substrates throughout the deposition process.

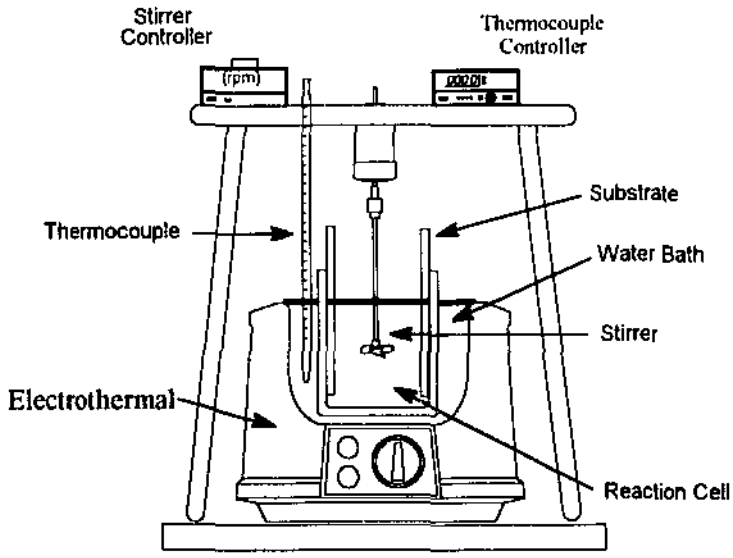

Figure 4.1 Experimental setup of Chemical Bath Deposition System

The 200mL volume of the bath solution was prepared accurately by sequential mixing of firstly the ammonia/ammonium base solution. At reaction temperature of ~ 60°C the precursor compounds of cadmium acetate [$Cd(CH_3COO)_2$] followed by thiourea [$CS(NH_2)_2$] were added under the influence of rapid stirring of mixing unit. Depositions identified for doping were complimented by an additional volume of $InCl_3$ after precursor addition. The depositions in call cases were performed in a fumed hood.

4.4 POST-DEPOSITION TREATMENT

At the end of the deposition runs, to avoid continued reaction the slides were taken out of the reaction cell and subject to quenching process using Milli-Q grade H_2O at 12°C. Films were then ultrasonically cleaned for 5min at room temperature and finally dried by blowing hot air. All films collected were stored in a vacuum desiccate to reduce impurity prior to optical analysis.

Films deemed for air annealing were placed in a furnace preheated to the desired temperature and timed. Annealed films for specific durations were removed and rapidly cooled in a vacuum desicator for approximately 10 minutes prior to storage.

4.5 OPTICAL TRANSMITTANCE SPECTROSCOPY

The optical transmittance characteristics of the CdS films were measured with a Varian dual beam spectrophotometer (model UV/VIS-300) in the spectral range 200 - 900nm. In addition to this, the sample chamber was modified to carry slides and a pc computer interface was modified and utilized as a data acquisition system. The schematic of the characterization apparatus is shown in Figure 4.2.

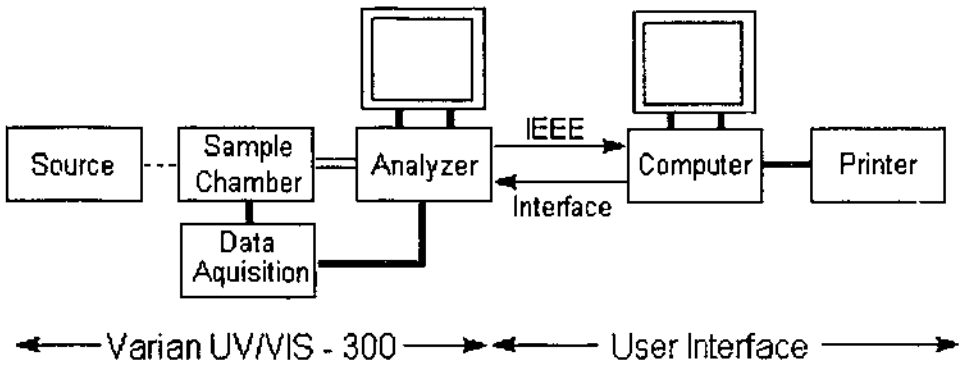

SAMPLE CHAMBER	: Reference and CdS Coated Reference
COMPUTER	: 386SX-33 PC
SOFTWARE	: Matlab, Excel and Minitab
PRINTER	: Cannon Bubble jet

Figure 4.2: Experimental setup for the measurements of optical transmittance.

Prior to optical analysis, CdS films deposited on the back side of the substrates were removed with HCl. The films were then subject to a purging process using Milli-Q H_2O then cleaned with ethanol and air dried. All spectra were recorded with simulanteously with the "reference beam" passing through the uncoated glass to nullify the absorption losses and the coated glass in the "sample beam".

4.6 OPTICAL ANALYSIS

The CdS transmission curves exhibit what is best described as a "sigmoidal" curve (see Figure 4.3), in addition regions of these curves correspond to the electronic band structure of the semiconductor.

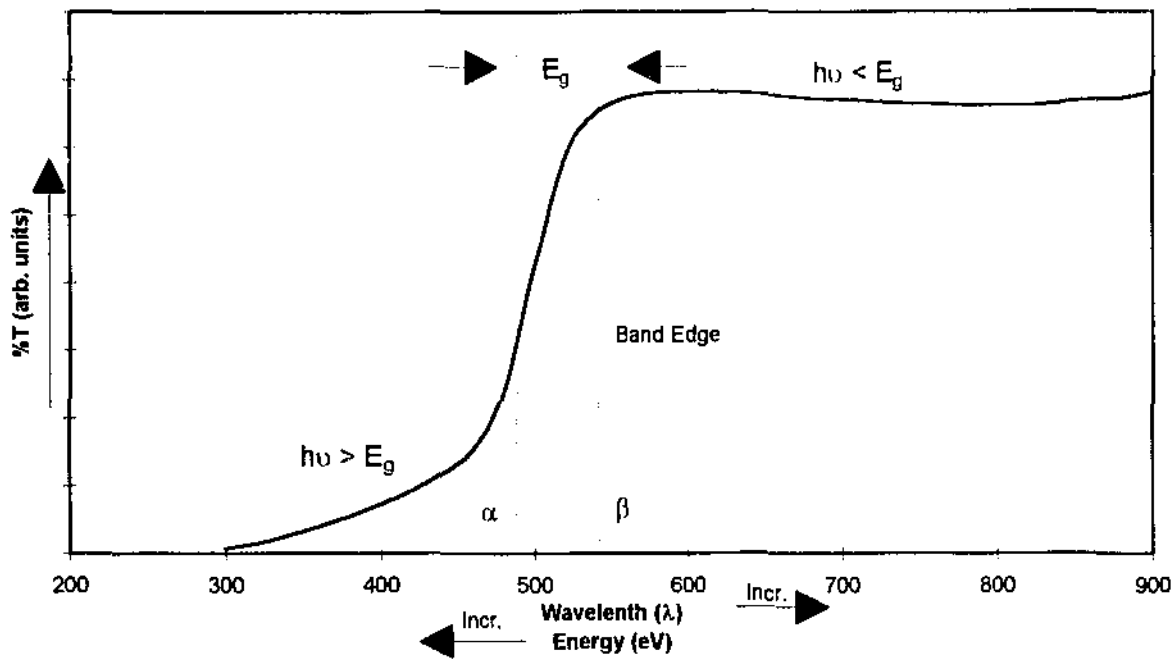

Figure 4.3: Transmission curve of an arbitrary transparent thin film semiconductor.

Photons (E = hν) incident on this semiconductor with energies greater than the bandgap energy (i.e. $h\nu > E_g$) show some predictable absorption, determined by the properties of the film (e.g. thickness & impurities). The region with the greatest rate of change of transmission (i.e. $\alpha \rightarrow \beta$) is associated with photon absorption by the intrinsic band gap.

A photon with energy $h\upsilon < E_g$ is unable to excite a valence band electron to the conduction band, and as consequence they are transmitted. Thus as we can see from Figure 4.3, that in intrinsic semiconductors there is negligible absorption with $h\nu < E_g$. This is in agreement with the experimental data that CdS is transparent in certain wavelength ranges (i.e. $\lambda \geq \beta$ nm) and opaque at the band edge (i.e. $\lambda \alpha <$ nm). As shown in Figure 4.4, analysis using this phenomena gives an accurate measure of the band gap energy.

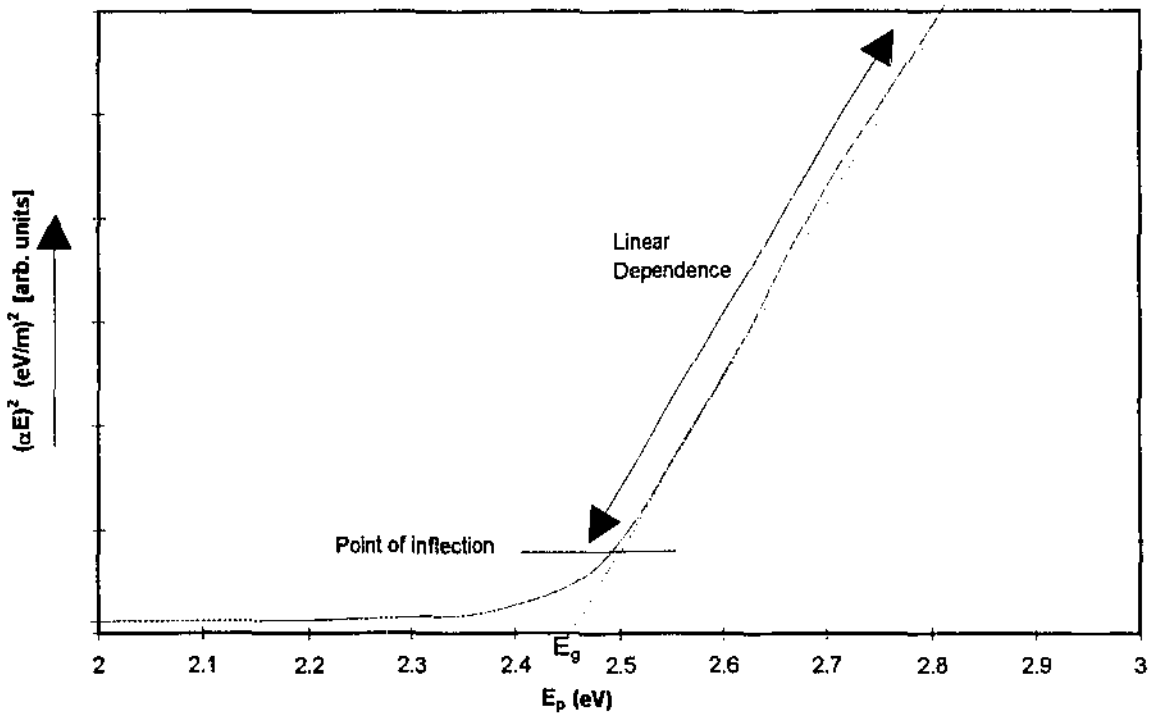

Figure 4.4 Absorption Coefficient Plot an arbitrary transparent thin film semiconductor.

The absorption coefficient, α, of the studied CdS was found to follow the relation:

$$\alpha E = A(E_p - E_g)^{0.5} \qquad [4\text{-}1]$$

where A is a constant, E_p is the photon energy and E_g is the band gap energy. A more detailed study of the α^2 dependence on hν by graphically means, reveals a region where the α^2 dependence on hν indicates a linear behaviour. This linear relationship can be interpreted as the presence of a direct optical transition between bands. Hence this linear relationship is a clear indication that the materials investigated are direct band gap semiconductors.

The bandgap energy of these semiconductors can be determined by extrapolating the linear portion of the absorption spectrum. Figure 4.4 shows the plot of $(\alpha E)^2$ versus hν, where the line of best fit intercepts the energy axis giving the bandgap energy. In general absorption coefficient plots of intrinsic CdS films show a straight line portion indicating it is a direct semiconductor.

Sub band-gap absorption due to a "tailing" effect is not evident in a optical absorption spectrum plotted from relationship [4-1]. A plot of the absorption coefficient versus band-gap energies in a semi-logarithmic graph according to:

$$\ln\alpha = \ln C + \left\{-\frac{E_g - h\nu}{E_o}\right\} \qquad [4\text{-}3a]$$

$$\ln\alpha = \ln C - \left(\frac{E_g - h\nu}{E_o}\right)$$

$$\therefore \quad \ln\alpha = \ln C + \left(\frac{h\nu - E_g}{E_o}\right) \qquad [4\text{-}3b]$$

produces a straight line of slope $\approx \frac{1}{E_o}$ from which the *Urbach parameter* can be deduced. The *Urbach parameter* (E_o), gives the steepness of the level of distribution near the band-edge (Boer, 1990).

4.7 FOURIER TRANSFORM INFRARED (FTIR) CHARACTERIZATION

Infrared characterization of the samples were performed at the Vibrational Spectroscopy Facility, Curtin University. The infrared absorbance/transmittance characteristics of the CdS films deposited on Si were measured using a Bruker single beam FTIR (Model IFS66) coupled with a data acquisition system. The investigated wavenumber coverage for the films were in the range 400 - 4000cm^{-1}.

Prior to analyzing the separate Si reference and film signals, the samples were placed into the analyzing chamber and purged with oxygen at a pressure ≈0.8mm Hg for approximately 20 minutes. When the atmospheric CO_2 signal stabilized at a minimum value the signals were then separately recorded over an average of 4000 scans of the specified wavenumber range.

Infrared absorbance/transmission spectroscopy of the prepared films were obtained from the subtraction of the absorption due to the silicon reference. Identification of impurity phases present in the films were based on systems software recognition algorithms and manual comparison to standard reference IR spectra

4.8 ELECTRICAL PROPERTIES

4.8.1 Dark and Photoconductivity (σ_p,σ_d) Characteristics

The conductivity characteristics of the various prepared films were investigated using a home-made setup as shown in Figure 4.5.

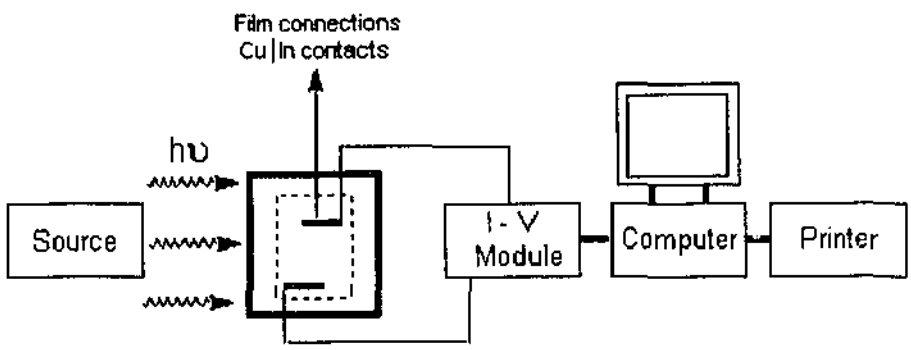

SOURCE : Phillips Tungsten-Halogen lamp 600W
SAMPLE-CELL : CdS Film on substrate with opaque backing
DATA ACUISITION : BBC ADC (Analog to Digital converter)
I -V MODULE : 9V DC Voltage source, OPAMP and Kiethley 619 Electrometer
COMPUTER : BBC and 486DX-33 PC
PRINTER : CANNON BUBBLE JET

Figure 4.5: Experimental setup for the measurements of photocurrent response in CdS thin films.

Using a modification to the Van der Pauw technique, a combination In|Cu contacts were arranged symetrically on the surface of the films at a separation of ≈ 22mm. Copper wires were attached to the contacts using silver paste and alligator clips. All leads were shielded to minimize induced currents and temperatures were maintained across the films using a crude heating element to eliminate feed back voltage. In order to check that the contacts were ohmic, a series of measurements were made on the voltage developed between the

two adjacent contacts as a function of the current drawn between two other introduced contacts.

Prior to the photoresponse measurements being formed, the films investigated were left to stabilize in the dark with an applied bias of 9V for 10 minutes. The current measurements were then taken 50 seconds in darkness (I_d), 150 seconds under solar illumination (I_p) and a further 100 seconds in the dark to show the photocurrent decay.

4.8.2 Dependence of Dark Conductivity [$\sigma_d(T)$] Measurements on Temperature

Due to the absence of a cryostat, the dark photoconductivity (σ_d) measurements were performed using a home-made cryostat whose schematic is shown in Figure 4.6. The temperatures of the samples were satisfactorily controlled using a modified steel thermos flask filled with liquid nitrogen at close to vacuum conditions

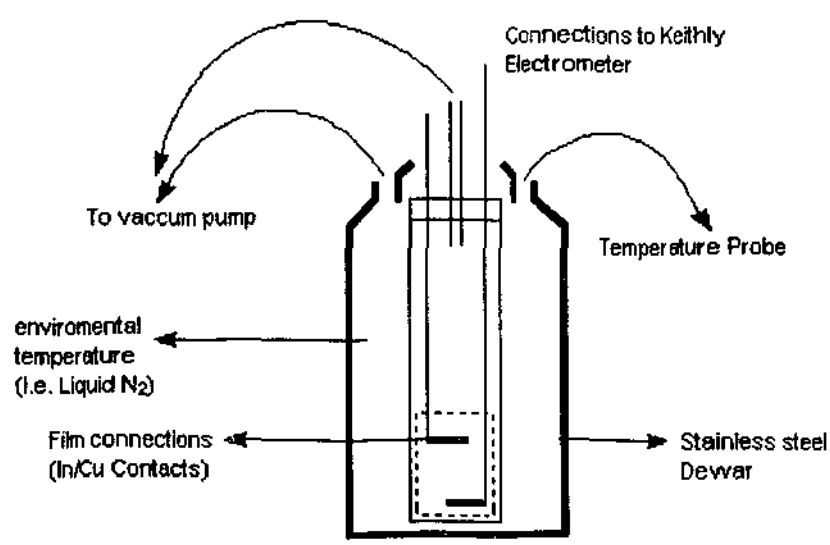

Figure 4.6: Schematic diagram of home-made cryostat

Temperatures were measured using a T-Type thermocouple with the existing thermocouple control unit (Model BTC-2220), and were varied by raising the sample at different levels. The temperatures that were investigated varied from 180 to 300K

4.8.3 Conductivity Type Determination (n-CdS)

The "Hot Probe" measurements were employed for determining the type of conductivity in the as deposited, doped and annealed films. For these measurements, two indium dots pressed onto the film with copper leafs at a separation of 5mm were used as electrodes. One electrode was kept at room temperature while the other was kept in contact with a soldering iron and the corresponding voltage defections were observed using a combination analog voltmeter and electrometer.

4.9 ELECTRICAL ANALYSIS

Using photoresponse curves obtained in section 4.8.1, the values of the relative photosensitivity factor S, can be defined as:

$$S = \frac{\Delta\sigma}{\sigma_d} = \frac{\sigma_p - \sigma_d}{\sigma_d} = \frac{R_p - R_d}{R_d} \qquad [4\text{-}4]$$

Since $\sigma_p >> \sigma_d$, $S \approx \sigma_p/\sigma_d$

where σ_d and R_d are the calculated dark conductivity and dark resistance, respectively, and σ_p and R_p represent similar parameters under photon illumination.

4.10 STRUCTURAL CHARACTERIZATION

Structural properties of the investigated films were determined by analyzing the X-ray Diffraction patterns (XRD) obtained by a Seimens Diffractometer (Model D-500) using CuK_{α} radiation. The scanning preferences and data acquisition format were controlled by an HP 216 PC using an IEEE interface. Signals recorded were both stored in the raw format and if there was a high noise to signal ratio a Gaussian Transform was used and also recorded.

Signals downloaded from the diffractometer to the HP 216A PC were stored in binary and were converted to ascii format. Peak recognition and comparison using the JPCDS database were performed on the signals using a program written in basic to change the ascii format into a 2 column format of 2θ and d-space (see APPENDIX I).

4.11 MORPHOLOGICAL CHARACTERIZATION

Morphological properties of the investigated films were obtained using a Park Scientific Instruments Atomic Force Microscope and a Digital Instruments Atomic Force Microscope. Determination of film thickness were obtained by chemically etching a series of steps into the film and then performing a cross section analysis along the steps relative to the silicon substrate.

5. CBD PROCESS AND CHARACTERIZATION

5.1 CHEMICAL BATH DEPOSITION

Deposition techniques, and their associated process parameters, have an effect on the nucleation and growth of the microstructure of a thin-film and its physical properties. A thin-film deposition technique involves three steps (Chopra & Kaur, 1983, pg. 2): (1) production of appropriate atomic/molecular/ionic species, (2) transportation of the unit species through a medium, (e.g. liquid) to a substrate, and (3) condensation of the unit species upon a substrate.

Thin-film growth in forming discontinuous structures can hence be considered as a group of nucleation and controlled surface-diffusion nuclei growth processes. Microscopy of thin films deposited under different thermodynamic conditions has revealed three broad growth stages (see Figure -1); (1) island type, (2) lateral type and (3) mixed (Stranski-Krastanov) type (Chopra & Kaur, 1983, pg3.).

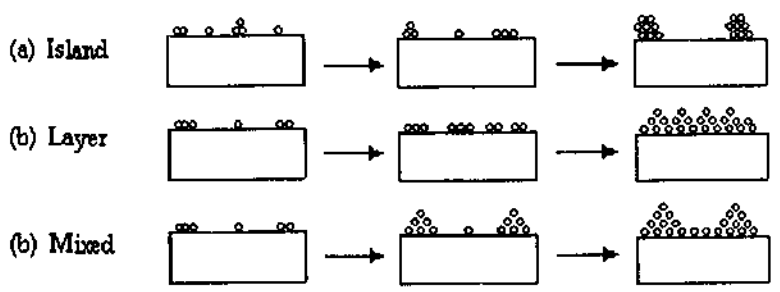

Figure 5.1 Film growth processes

There has been no substantial evidence to date that film growth is limited by any of the above mechanisms for a particular deposition technique. It is evident however, that under different forms of deposition, process parameters have a major influence on the way in which thin-films grow. With the solution deposition techniques, there are a number of chemical and physical parameters which define the growth mechanism. In order to

determine the effect of these parameters on growth type, further experimentation and analysis is required.

In chemical bath deposited CdS thin-films, the scientific literature indicates that the film morphology consists of a continuous and a particulate phase. The dominance of one of these phases determines the optical characteristics (e.g. transparent or opaque) of the film. Studies of the growth of CBD CdS thin films have show that film growth occurs by an ion-by-ion condensation of the impinging particles ($[Cd^{2+}]$ & $[S^{2-}]$) and by colloidal particles of CdS adhering to the substrate surface. These colloidal particles grow in size with time and form the particulate part of the film (Sebastian & Hu, 1994).

5.2 DEPOSITION CHEMISTRY

In theory chemical bath deposition of the CdS thin film semiconductor can be obtained by the direct reaction between $[Cd^{2+}]$ and $[S^{2-}]$ precursor species in solution. This chapter aims to improve the knowledge and associated reaction mechanisms that form the deposition process. This chapter will review previous works in correlation to this studies analysis.

There are a number of reaction schemes available for the formation of CdS films, the system we considered involves the following reaction stages:
[1] precipitation of cadmium hydroxide,

$$Cd^{2+} + 2OH^- \Leftrightarrow Cd(OH)_2 \qquad [5\text{-}1]$$

[2] formation of sulfide ions by the hydrolysis of thiourea with hydroxide ions,

$$CS(NH_2)_2 + 2OH^- \Rightarrow S^{2-} + C\,H_2N_2 + 2H_2O \qquad [5\text{-}2]$$

[3] release of cadmium ions by the decomplexation,

$$Cd(NH_3)_4^{2+} \Leftrightarrow Cd^{2+} + 4NH_3 \qquad [5\text{-}3]$$

and [4] replacement of hydroxide ion by sulfide ion,

$$Cd(OH)_2 + S^{2-} \Leftrightarrow CdS + 2OH^- \qquad [5\text{-}4a]$$

or the direct interaction of the impinging species

$$Cd^{2+} + S^{2-} \Rightarrow CdS \qquad [5\text{-}4b]$$

When the ionic product exceeds the solubility product of CdS (i.e. $[Cd^{2+}][S^{2-}] \geq K_{sp}$), CdS precipitates out either as a colloid in the solution or as a film on the substrate by the previously mentioned nucleation processes.

The global reaction representing the above staged reactions (i.e. [5-1] to [5-4]) can be written as:

$$Cd(NH_3)_4^{2+} + CS(NH_2)_2 + 2OH^- \Rightarrow CdS + CH_2N_2 + NH_3 + 2H_2O \qquad [5\text{-}5]$$

The addition of ammonium acetate produces hydroxide ions and ammonia according to the equilibrium reaction:

$$NH_3 + H_2O \Leftrightarrow NH_4^+ + OH^- \qquad [5\text{-}6]$$

Ammonia also permits the controlled precipitation of CdS by complexing the "free" cadmium ions (Equation 5-7 where n is the number of ligand species) and by dissolving cadmium hydroxide according to:

$$Cd^{2+} + \alpha NH_3 \Leftrightarrow Cd(NH_3)_n^{2+} \qquad n \in [1,6] \qquad [5\text{-}7]$$

$$Cd(OH)_2 + 4(NH_3) \Leftrightarrow Cd(NH_3)_4^{2+} + 2OH^- \qquad [5\text{-}8]$$

Equations [5-1] to [5-8] are related to the film formation process and are interdependent. It is evident from this work that the hydroxide concentration, as measured from pH, plays a vital role in the process. It affects the formation of cadmium hydroxide, thiourea decomposition and the relative concentrations of both ammonia and "free" cadmium ions. Ammonia concentration affects the concentration of the cadmium ions, precipitation of cadmium hydroxide and consequently, the pH of the deposition solution

In support of Lanning *et al.*, (1990), it was revealed that the deposition of CdS is directly related to the cadmium hydroxide [$Cd(OH)_2$] in solution. When cadmium hydroxide is present in small concentrations ($\leq 10^{-2}$M) within the solution, it absorbs preferentially on the substrate surface and catalyses the decomposition of thiourea to form CdS. Also, any soluble "free" cadmium ions not associated with hydroxide ions should be complexed with another ligand such as ammonia, to minimize the concentration of unallocated "free" cadmium ions. Large concentrations of "free" cadmium ions risk promoting excessive precipitation of $Cd(OH)_2$. This consequently enables CdS to form indiscriminately in the bulk solution as opposed to the formation of a film on the substrate surface.

The quality of the film, morphology and the deposition rate of the process are intimately related to the solubility equilibria in the solution. Specifically, film uniformity and structure are directly related to the preferential precipitation of cadmium hydroxide on activated surfaces (heterogeneous nucleation) as opposed to precipitation in the bulk solution (homogeneous nucleation).

It has been observed throughout this study that the depositions investigated generally involve three distinct phases of growth. At the early stages of the reaction, where the deposition time $t \leq 8$min (i.e. induction period), the growth is very slow. Since all the stage reactions differ in nature, they also require differing reaction energies to overcome

their respective activation energy barriers. As a result, the induction period is similar to a countdown, where at the end of the period all the reactions have sufficient energies to interact with one another. It is this flaw in the process, where the staged reactions await their participation, that highlights the need to investigate the effects of possible catalysts.

In the next growth phase, of growth usually occurring between 8 - 12 minutes, growth of the characteristic yellow film (CdS) through ion-by-ion condensation is evident. It is this period where ideal growth is achieved and should be maximized. Unfortunately as the reaction progresses and deposits film, concentrations of aqueous compound sources decline. As a result, deposition times where $t \geq 50$min on average show an indication that the deposition process is becoming unstable as evidenced by the presence of traces of particulate CdS. Since the "as deposited" films are hard and coherent and unable to return to solution the imbalance only increases, which is evident of deposition times $t > 60$min.

5.3 KINETIC MODELING OF THE DEPOSITION PROCESS

Thermodynamic analysis of the equilibrium conditions that favour thin film growth allows us to select the optimum composition of the reaction mixture. The mechanics of the formation of CdS thin films can be obtained by graphical solutions of the equations describing the solubility equilibria (Kaur, 1983):

$$Cd(OH)_2 \Leftrightarrow Cd^{2+} + 2OH^- \qquad [5\text{-}9]$$

and

$$Cd(NH_3)_4^{2+} \Leftrightarrow Cd^{2+} + 4NH_3 \qquad [5\text{-}10]$$

These two solubility expressions can further be quantitatively characterized by the solubility product (SP) of cadmium hydroxide:

$$SP = [Cd^{2+}][OH^-]^2 \qquad [5\text{-}11]$$

and the instability constant (K_i) of cadmium tetrammine:

$$K_i = \frac{[Cd^{2+}][OH^-]^2}{[Cd(NH_3)_4^{2+}]} \qquad [5\text{-}12]$$

Taking the logarithm of Equation [5-11], converting to concentration exponents, and solving for pH, we obtain:

$$pH = \tfrac{1}{2}p[Cd] - \tfrac{1}{2}p[SP] + pK_w \qquad [5\text{-}13]$$

where K_w is the ionization constant ($\approx 10^{-14}$) of water.

This mathematical expression we define as the "Hydroxide Line", where pH of the solution is plotted against the concentration exponent of the cadmium ions $p[Cd^{2+}]$.

A similar treatment performed with [5-12] yields:

$$4p[NH_3] = pK_i + p[Cd(NH_3)_4^{2+}] - p[Cd^{2+}] \qquad [5\text{-}14]$$

Ammonia forms an additional solubility equilibrium reaction in aqueous solutions:

$$NH_3 + H_2O \Leftrightarrow NH_4^+ + OH^- \qquad [5\text{-}15]$$

From the above equilibrium reaction, the proportion of ammonium and hydroxide ion concentrations are equal (i.e. $[NH_4^+] = [OH^-]$). Since Equation [5-14] is an expression of $p[NH_3]$, an identity describing $p[NH_3]$ as a function of pH needs to be derived. We make use of Equation [5-15] and the ionization constant of ammonium hydroxide (K_b^*) to form a rudimentary identity:

$$K_b^* = \frac{[NH_4^+][OH^-]}{[NH_3]} \approx \frac{[OH^-]^2}{[NH_3]} \qquad [5\text{-}16]$$

After further rearrangement and substitution of the above quantitative description of Equation [5-16] into [5-17], we can rearrange the expression to include pH, giving:

$$p[NH_3] = 2pK_w - 2pH - pK_b^* \qquad [5\text{-}17]$$

Equating equations [5-14] and [5-17] yields the what we define as the "Complex Line":

$$pH = pK_w - {}^1/_8p[K_i] - {}^1/_2p[K_b^*] - {}^1/_8p[Cd(NH_3)_4^{2+}] + {}^1/_8p[Cd^{2+}] \qquad [5\text{-}18]$$

A graphical representation of both the complex and hydroxide lines is shown in Figure 5.2.

Hydroxide: $pH = {}^1/_2p[Cd] - {}^1/_2p[SP] + pK_w$

Complex: $pH = pK_w - {}^1/_8p[K_i] - {}^1/_2p[K_b^*] - {}^1/_8p[Cd(NH_3)_4^{2+}] + {}^1/_8p[Cd^{2+}]$

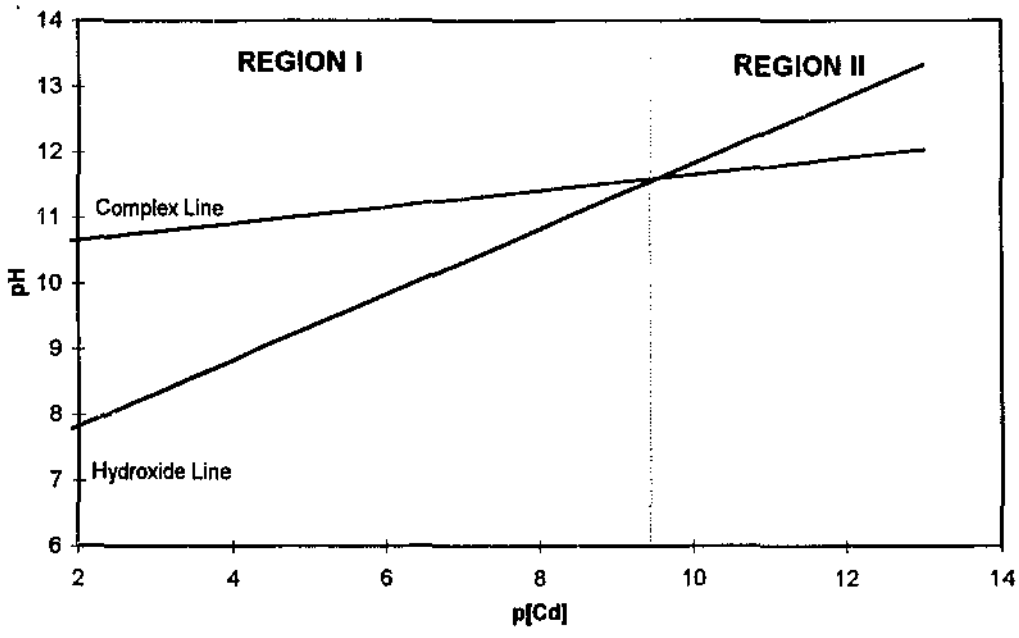

Figure 5.2: Graphical representation of hydroxide line and complex line interaction.

Compound concentrations where the pH value lies above the hydroxide line exhibit stable forms of $Cd(OH)_2$. This is characterized by hard, coherent, specularly reflecting films ($d \leq 1\mu m$). However, below this boundary, $Cd(OH)_2$ is unstable and precipitates out, causing disruption to the deposition system.

It can be seen that the hydroxide and complex lines intersect, and the perpendicular of that intersection forms two distinct regions. In Region I (i.e. to the left of the intersection), the complex line lies above the hydroxide line. This means that solutions with these pH values have stable hydroxide forms which assist in the controlled decomposition of thiourea at reaction temperatures. In Region II, pH values permit the cadmium tetrammine complex to dominate with the absence of an ammonia equilibrium reaction producing $[OH^-]$ ions. As a result, hydroxides must be physically introduced into the system to permit the deposition process.

From solubility expressions [5-10] and [5-11] we see that the cadmium hydroxide ion concentration, and subsequently the hydroxide ion concentration are an integral part of the deposition process. At pH values below the complex line, cadmium tetrammine dominates. This domination masks all available associated and unassociated cadmium ions, suspending any deposition sub-processes.

As mentioned earlier, $Cd(OH)_2$ is an integral player in the deposition process. A closer examination of the associated solubility equilibrium [4-8] reveals a similar treatment can be made. Since we know the numerical values of the instability constant of cadmium tetrammine, and the solubility product of cadmium hydroxide, substituting the cadmium ion concentration from the solubility product into the instability constant we obtain, after rearrangement:

$$p[OH^-] = \tfrac{1}{2}p[SP] + 2p[NH_3] - \tfrac{1}{2}p[K_i] - \tfrac{1}{2}p[Cd(NH_3)_4^{2+}] \qquad [5\text{-}19]$$

5.4 INFLUENCE OF CADMIUM CONCENTRATION ON GROWTH RATE

The measured film thicknesses (d) of deposited CdS film at different deposition times, determined using AFM cross section analysis, are shown in Figure 5.3.

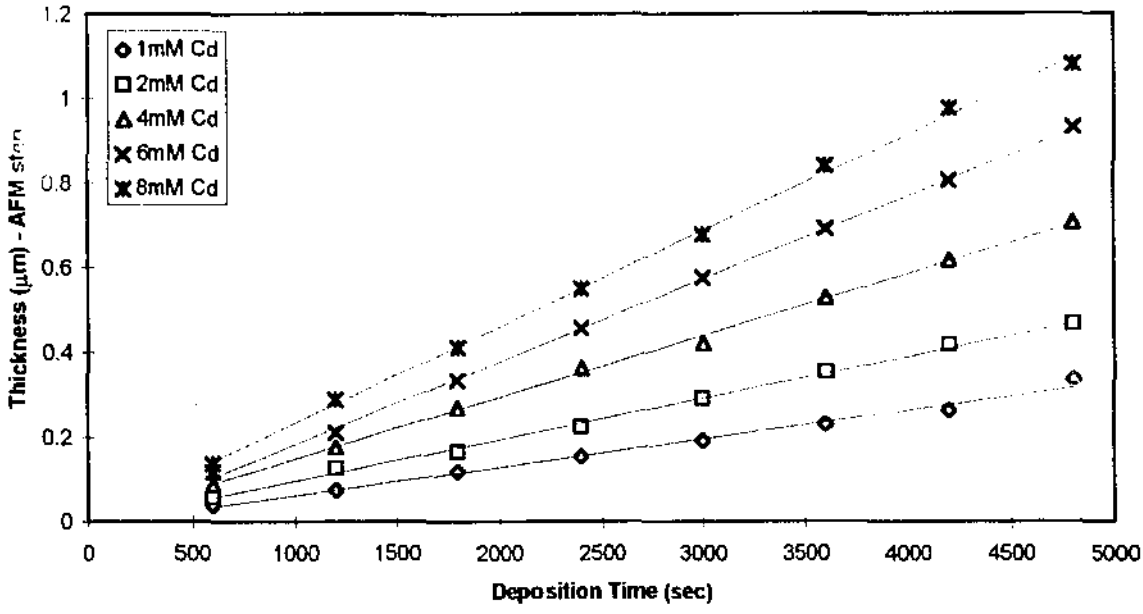

Figure 5.3: Influence of Cadmium salt concentration: Initial conditions [TU] = 10mM, $[NH_3]$ = 0.8M and T = 60°C.

Increasing the cadmium ion concentration increases the growth rate of the CdS thin film. This increase is not entirely without its drawbacks. For example, for [Cd] concentrations ≥ 10mM, film growth becomes masked by the onset of colloidal growth. Initial induction times where growth commences are decreased, however, thin film growth is characterized by a three phase mechanism as described in Section 5.1. At some point in the process, the ionic product of CdS exceeds the solubility product (K_{sp}), thin film growth slows and colloidal growth accelerates. This indicates that there may be an additional equilibrium sub-reaction between these two growth modes which was not the subject of this investigation.

The presence of these colloids, rather like a catalyst, upsets the solubility equilibrium and hence the thin film formation in a way that is not recoverable. The abundance of these colloids, that coalesce to form a CdS powder, draws the unassociated "free" cadmium ions and associated cadmium ions out of solution by electrostatic attraction. Since the $[S^{2-}]$ is more electronegative than $[Cd^{2+}]$ in the form of CdS it would theoretically form a temporary dipole of negative charge. This negatively charged cloud would be at the extremity of the interatomic bond length, attracting cadmium, ions as seen below in Figure 5.4.

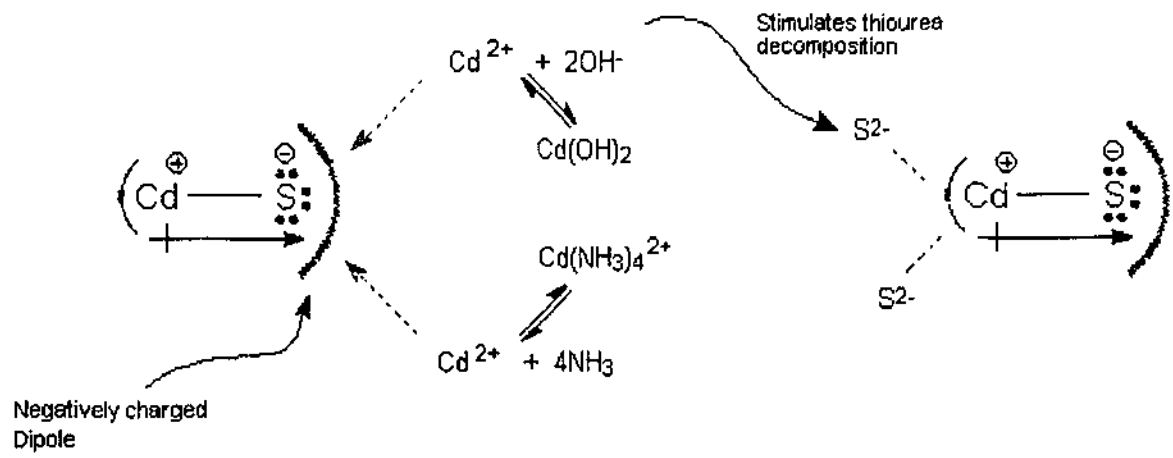

Figure 5.4: Representation of the influence of increased impinging ion concentration of $[Cd^{2+}]$ and $[S^{2-}]$

In addition the corresponding Log(r) curves (were the deposition rate, r = d/dep. time) determining reaction order is shown in Figure 5.32, with a summary of the computations involved in Table 5.1.

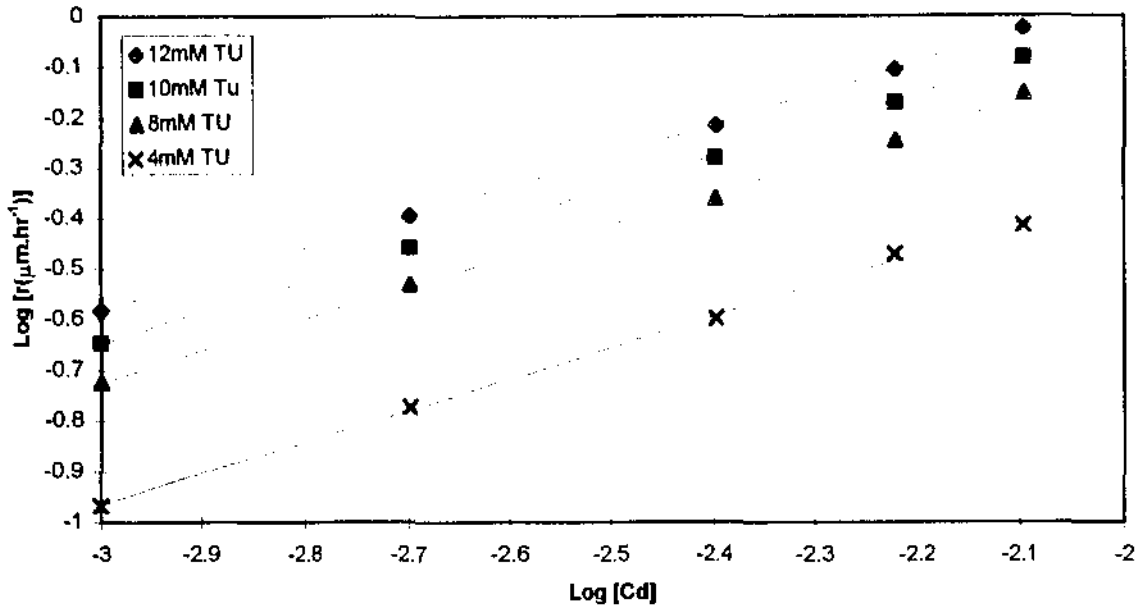

Figure 5.4: Influence of cadmium concentration on growth rate, for different thiourea concentrations at 60°C.

Table 5.1: Influence of Cadmium concentration on film growth

Curve	Thiourea Concentration [Mol-L^{-1}]	Reaction order
[1]	0.004	0.599
[2]	0.008	0.602
[3]	0.01	0.6
[4]	0.012	0.596

As seen in Figure 5.4, the concentration of the cadmium species has a positive effect by increasing film growth. Increasing the Cd species for the range considered reveals a linear effect with a mean reaction order of approximately 0.6. From this interpretation, it implies the other precursor compound (i.e. thiourea) may also have an integral role in the formulation of growth rate equation.

5.5 INFLUENCE OF THIOUREA ON GROWTH RATE

The effect of thiourea concentration on film thicknesses of deposited CdS at different deposition times, is shown in Figure 5.6.

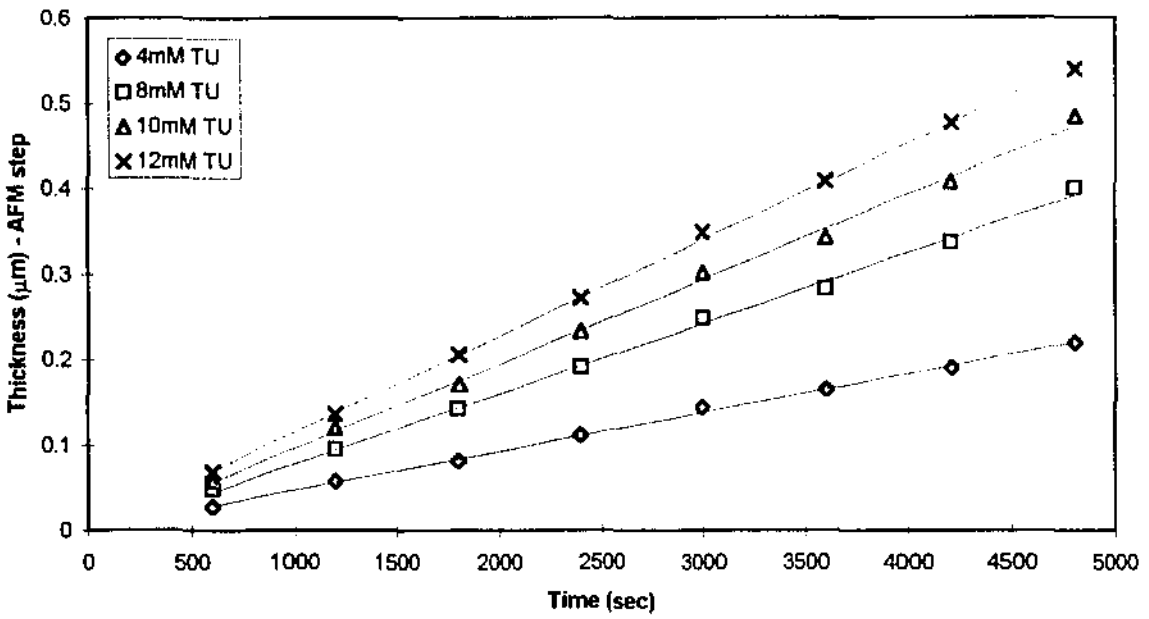

Figure 5.6: Influence of Thiourea concentration: Initial Conditions [Cd] = 2mM, [NH_3] = 0.8M and T = 60°C.

Similar to that encountered in the cadmium species, Figure 5.6 reveals an increase in the thiourea concentration is accompanied by an increased growth rate. The onset of colloidal growth is similarly to the cadmium influence, although it is more pronounced for the thiourea dependence.

During film growth lattice defects arise from the formation of the CdS matrix, possibly producing the temporary dipoles as mentioned earlier. Since sulfur (S) atoms are polymorphic in nature, under the influence of these lattice defects, it is possible that they combine with the unallocated cadmium species, resulting in deviations in the CdS stoichiometry.

The Log(r) curves determining reaction order of the species is shown in Figure 5.7, with a summary of the computations in Table 5.2.

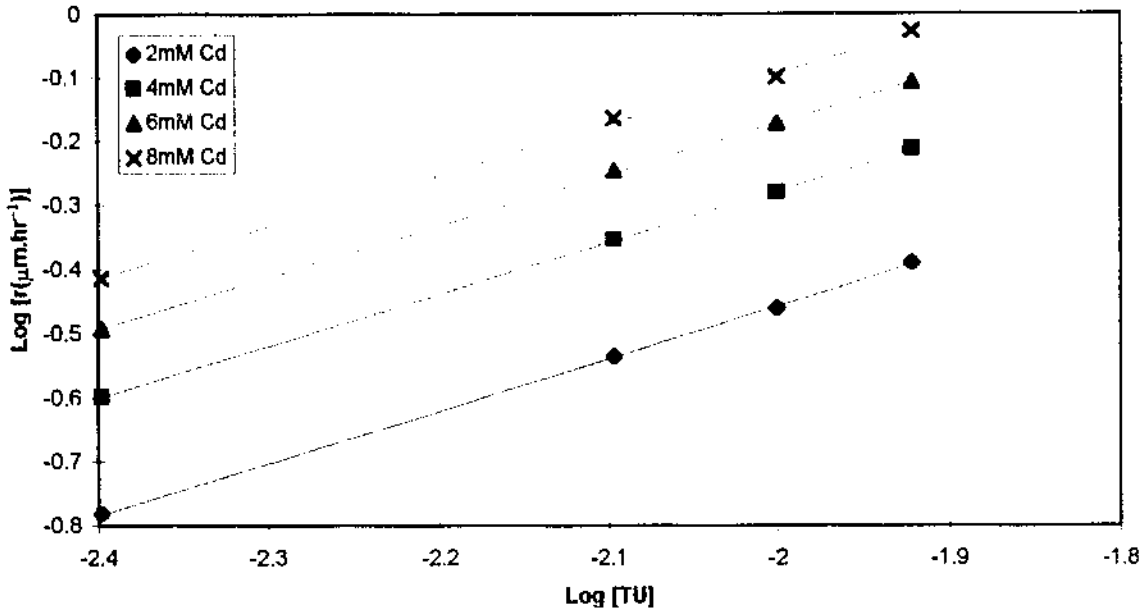

Figure 5.7: Influence of thiourea concentration on growth rate, for different cadmium concentrations at 60°C.

Table 5.2: Influence of Thiourea concentration on film growth

Curve	Cadmium Concentration [Mol·L^{-1}]	Reaction order
[1]	0.002	0.805
[2]	0.004	0.802
[3]	0.006	0.801
[4]	0.008	0.790

As with cadmium, increasing the thiourea concentration increases the film growth rate. The data analysis of the effect of the S species for the range considered reveals a linear effect with a mean reaction order of approximately 0.80. Since sulfur has a reaction order greater than that of the cadmium species, it can be interpreted that thiourea has a greater influence over the deposition system. This is in agreement with the chemistry of thiourea and the polymorphic nature of the atoms it releases.

5.6 INFLUENCE OF AMMONIA CONCENTRATION ON GROWTH RATE

Unlike the impinging ion sources in the formation of CdS, the presence of ammonia does not actively participate in the formation of the CdS matrix. It does however provide an environment for which this process can take place. The influence of ammonia concentrations on film thicknesses of deposited CdS at different deposition times is shown in Figure 5.8.

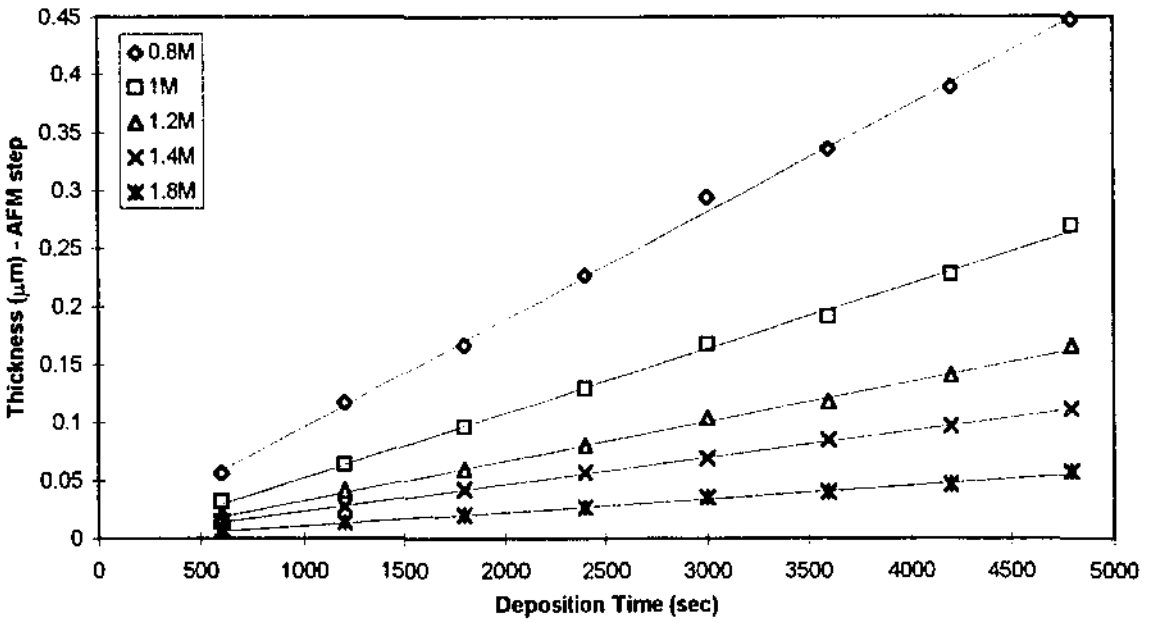

Figure 5.8: Influence of Ammonia concentration: Initial Conditions [Cd] = 2mM, [TU] = 10mM and T = 60°C

Unlike the influence of the impinging ion sources for cadmium and sulfur, Figure 5.8 reveals that increasing the concentration of the ammonia environment decreases the growth rate. A closer examination of this effect reveals that there is a substantial benefit in deposition conditions with high pH environments. The onset of colloidal growth is significantly reduced at increased ammonia concentrations.

The Log(r) curves determining reaction order of the species is shown in Figure 5.9.

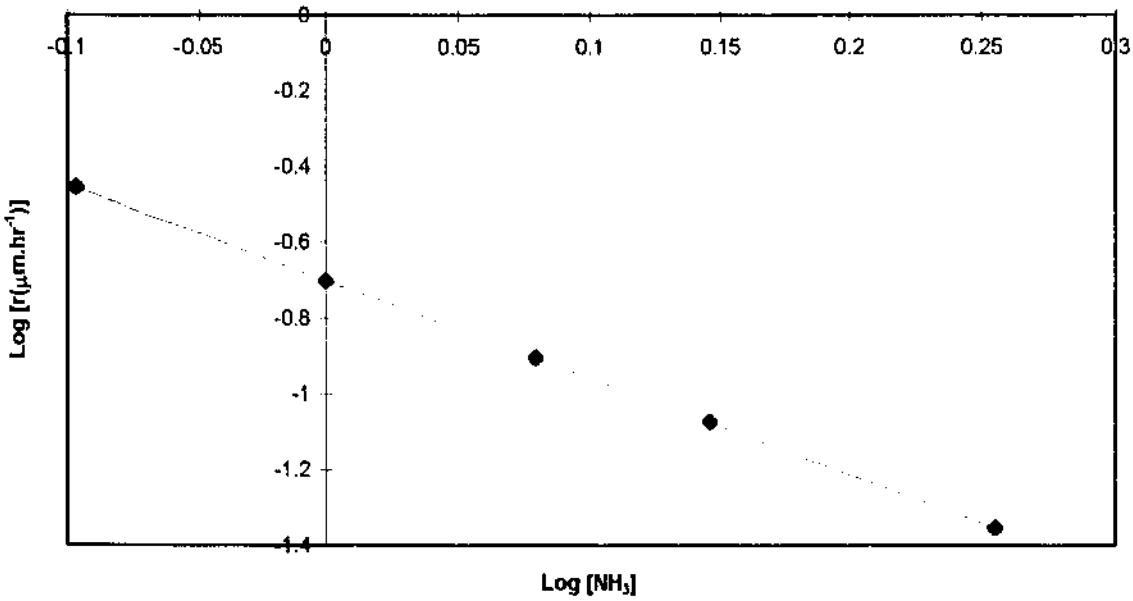

Figure 5.9: Influence of cadmium concentration on growth rate, for different thiourea concentrations at 60°C.

At higher concentrations of ammonia in solution (i.e. ≥ 0.8M), there is a much larger proportion of cadmium complexes (e.g. $Cd(NH_3)_4^{2+}$), avoiding spontaneous hydroxide precipitation. This is desirable since device quality thin films used to be produced by slow deposition rates characteristic of controlled ion-by-ion condensation. Ammonia concentrations that are 100 times greater than the impinging ion sources satisfactorily control the ideal growth mode, that is, of ion-by-ion condensation.

Unlike the participating precursor compounds, increases in ammonia concentration decreases the film growth rate. The data analysis of the effect of the $[NH_3]$ species for the range considered reveals a linear effect with a mean reaction order of approximately 3.2. Since trend is in agreement with explanation of deposition chemistry described in Section 5.2.

5.7 INFLUENCE OF AMMONIUM CONCENTRATION ON GROWTH RATE

The introduction of ammonium salts (i.e. NH_4Ac), as seen in Figure 5.10, results in a strong decrease in the growth rate as ammonium concentration increases. This increase in ammonium concentration leads to a decrease in the pH according to reaction [5-6] and hence, a decrease in growth rate since hydroxide ions are involved in reaction [5-2].

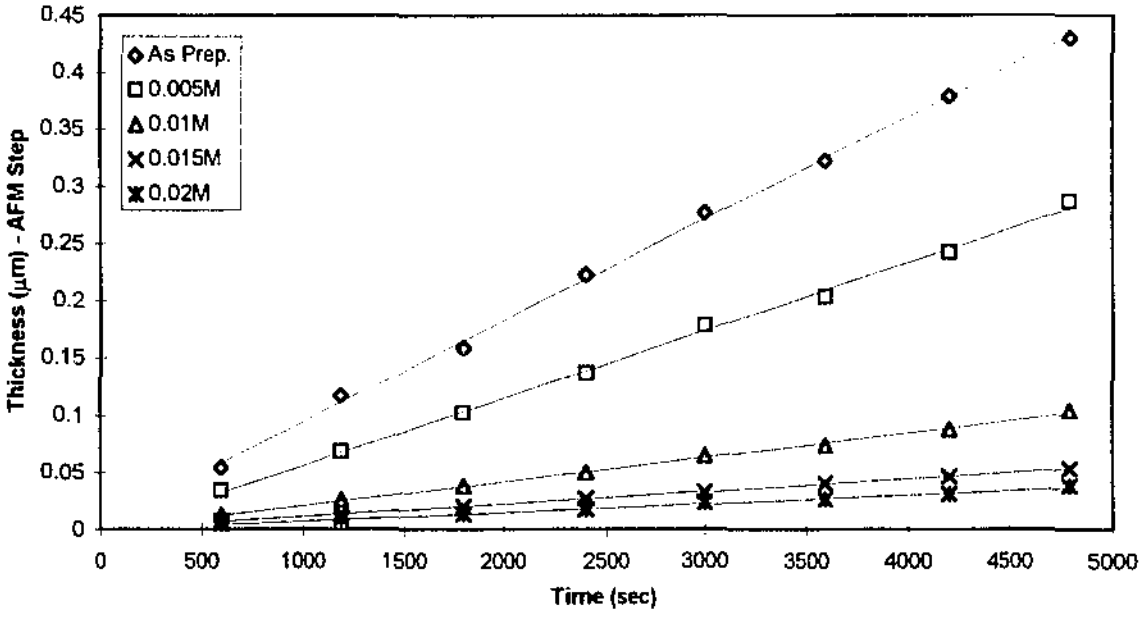

Figure 5.10: Influence of Ammonia concentration: Initial Conditions [Cd] = 2mM, [TU] = 10mM and $[NH_3]$ = 1.80M at T = 60°C.

It has been observed throughout the deposition process that the addition of ammonium salts (i.e. NH_4Ac) changes the particular deposition system's ability to act as a medium for the deposition of CdS. The ammonium ion $[NH_4^+]$ decreases the growth rate as a consequence of increasing its ion concentration (Figure 5.10). The ammonium ions present in this system (as a result of ionization) cause a decrease in the proportion of unassociated hydroxide ions in solution. These hydroxide ions also play the key role in the decomposition of the cadmium tetrammine complex, which as a result releases the cadmium ions.

The corresponding log(r) plot determining the reaction order is given in Figure 5.11.

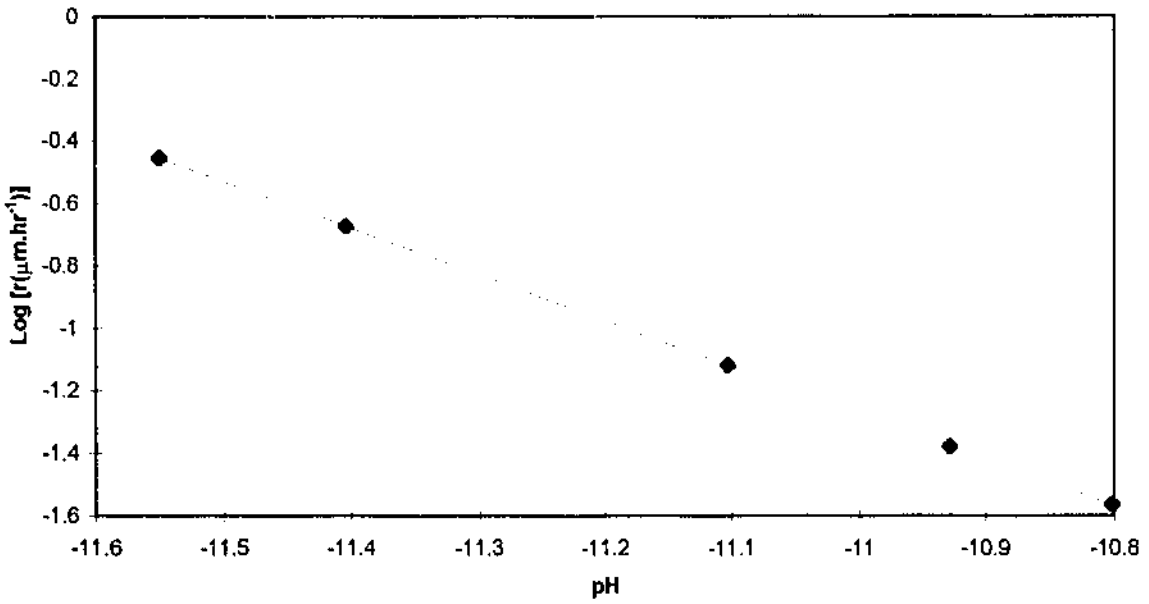

Figure 5.11: Influence of pH on growth rate, for different ammonium salt concentrations at 60°C.

Since the addition of ammonium ions (i.e. NH_4^+) has a direct influence upon the pH of the solution according to Equation [5-6], we can assume for the purposes of this study that $pH \approx p[NH_4^+]$. As seen from the previous study and from the plot growth rate increases as a consequence of an increased pH. A mean reaction order of 1.5 is obtained from the experimental data.

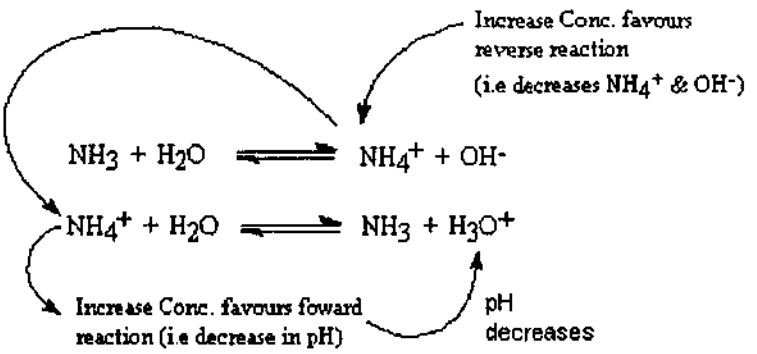

Figure 5.12: Schematic representation of ammonium ion [NH_4^+] interaction in solution

In addition to the reduction of the unassociated hydroxide ions, the pH decreases and consequently the [OH^-] are prevented from performing their decomposition function. The [OH^-] reduction is highlighted reaction schematic in the Figure 5.13.

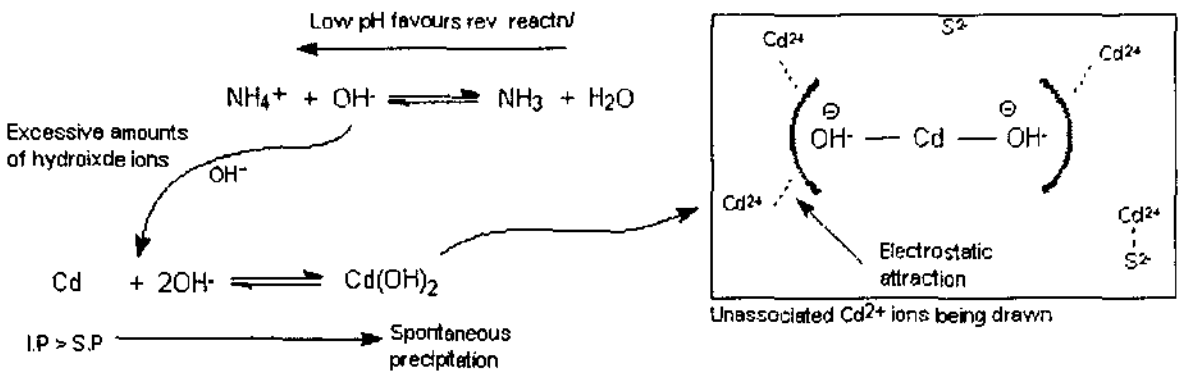

Figure 5.13: Schematic representation of the consequence of increased ammonium ion [NH_4^+] concentration

5.8 MODELING OF GROWTH KINETICS

In order to examine the dependence of the film deposition rate with reaction temperature an Arrhenius based experiment was performed. The Arrhenius plot of deposition rate in Figure 5.14 reveals a strong temperature dependence in concentration range investigated. The basic film growth rate can be written as:

$$R(\mu m \cdot hr^{-1}) = R_o \exp(^{-E_{act}}/_{RT}) \qquad [5\text{-}20]$$

where E_{act} is the activation energy of the process being investigated, R is the growth rate, T the temperature (Kelvin) and R_o is the initial temperature.

Here a plot of lnR versus 1/T should enable us to determine the activation energy (E_{act}) of the particular reaction. For the deposition conditions investigated, the activation energy (E_{act}) for the reaction was determined to be 81.5 kJ·mol^{-1} or 5.09 x 10^{23} eV· mol^{-1} .

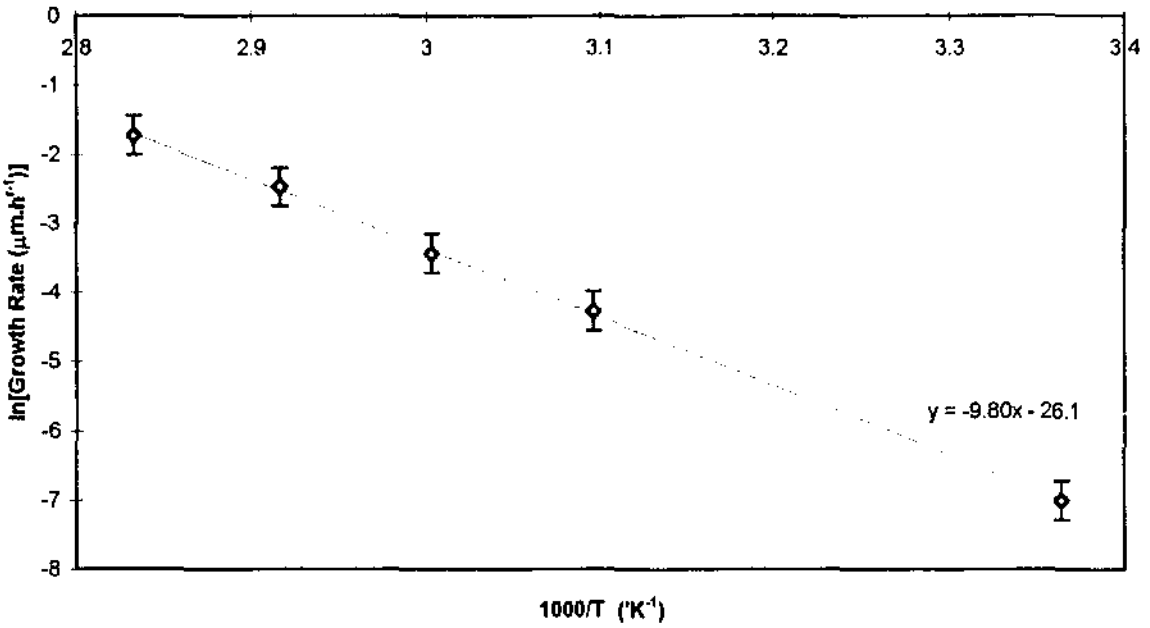

Figure 5.14: Arrhenius plot of growth rates at different operational temperatures

From the given reaction orders determined in Sections 5.3 to 5.6 we can write the film growth rate as a function of solution concentration as:

$$R(\mu m \cdot hr^{-1}) \cong K \frac{[Cd]^{0.6}[TU]^{0.8}}{[NH_3]^{3.2}[H]^{1.5}} \qquad [5\text{-}21]$$

where the equilibrium constant $K \approx 10^{-14.7}$ and the species concentrations [] are in the form mol·L^{-1}.

5.9 DOPING CHEMISTRY

Since doping of CdS thin films through high temperature diffusion methods are causing significant optical response problems, it gives rise to alternative methods. Doping in-situ methods are highly desirable since they theoretically cause marginal broad absorption bands close to the band edge. It is this incentive for photodetector device applications that sets the scene for this small study.

During the deposition process outlined in Sections 5.2, the impinging particles would form a lattice upon the substrate. This lattice is much like a "jig-saw" puzzle (Figure 5.15) consisting of cadmium and sulfide ions, combine in certain orientations which attracts other pieces. This orientation dependency would reflect the dipole strengths of the relevant particles.

At the same time these dipole strengths may attract additional cations within the system. Hence these attractions form the basis of the doping process whereby dopant atoms diffuse from solution into the CdS matrix.

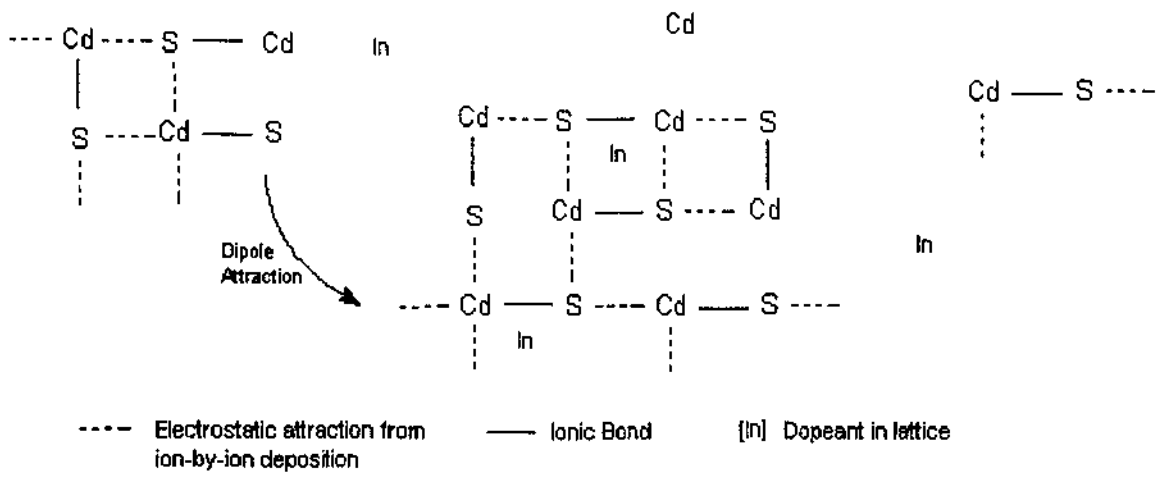

Figure 5.15: Theoretical model of the doping of CdS lattice through film growth

The introduction of indium atoms into the film functions to create an n-type material where the majority carriers are electrons. Small concentrations of these dopants (i.e. <

10^{21} atoms·cm^3) is ideally designed to avoid forming alloyed compounds. In high concentrations these particles would actively participate in formation of the lattice:

$$Cd^{2+} + S^{2-} + In^{2+} \Rightarrow InCdS^{2+} \qquad [5\text{-}22]$$

However in small concentrations these impurities may be trapped in the CdS matrix by overlapping lattices in a 3 dimensional array according to the possible reaction schematic in Figure 5.16.

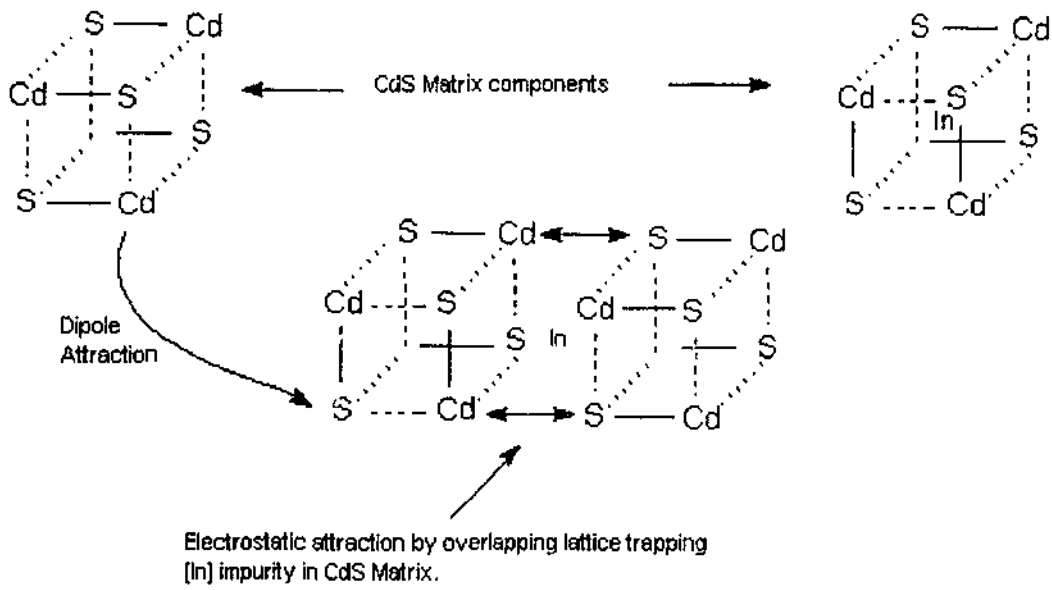

Figure 5.16: Schematic representation of the CdS matrix trapping In atoms.

6. OPTICAL CHARACTERIZATION

6.1 GROWTH RATE DEPENDENCE OF OPTICAL TRANSMITTANCE

The optical transmission for CdS films as a function of deposition time is shown in Figure 6.1. The transmission decreases marginally in the region $\lambda \geq 510$nm as the film thickness increases.

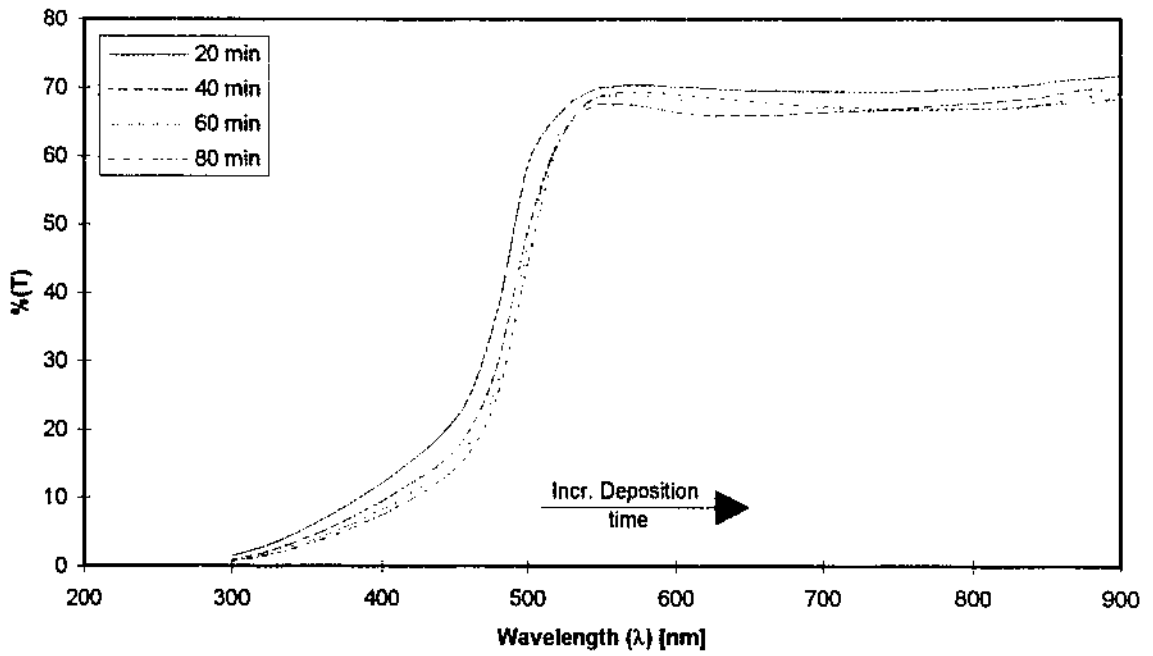

Figure 6.1: Optical transmittance spectrum of as-deposited CdS thin film at various deposition times. Deposition Conditions: [Cd] = 2mM, [TU] = 10mM, [NH_3] = 1.80M and T = 60°C

In addition, the transmission curves observed also reveal the presence of a broad transmission maxima broad peak at $\lambda \approx 510$nm close to the band edge of the film. This transmission enhancement effect at the band edge can be attributed to improved film

uniformity and crystallinity for longer deposition times. It is this uniformity which enhances the ion-by-ion interaction process on the substrate by providing preferred nucleation sites.

As observed from Figure 6.2, there is a linear dependence of the $(\alpha E)^2$ versus hυ at the band edge. It this reproducible property which is prominent throughout all the depositions investigated that indicates the presence of a direct optical transition in the CdS band structure (Kittel, 1996). Hence it can be deduced from this standard feature that the CdS films produced by the CBD process are direct semiconductors in nature.

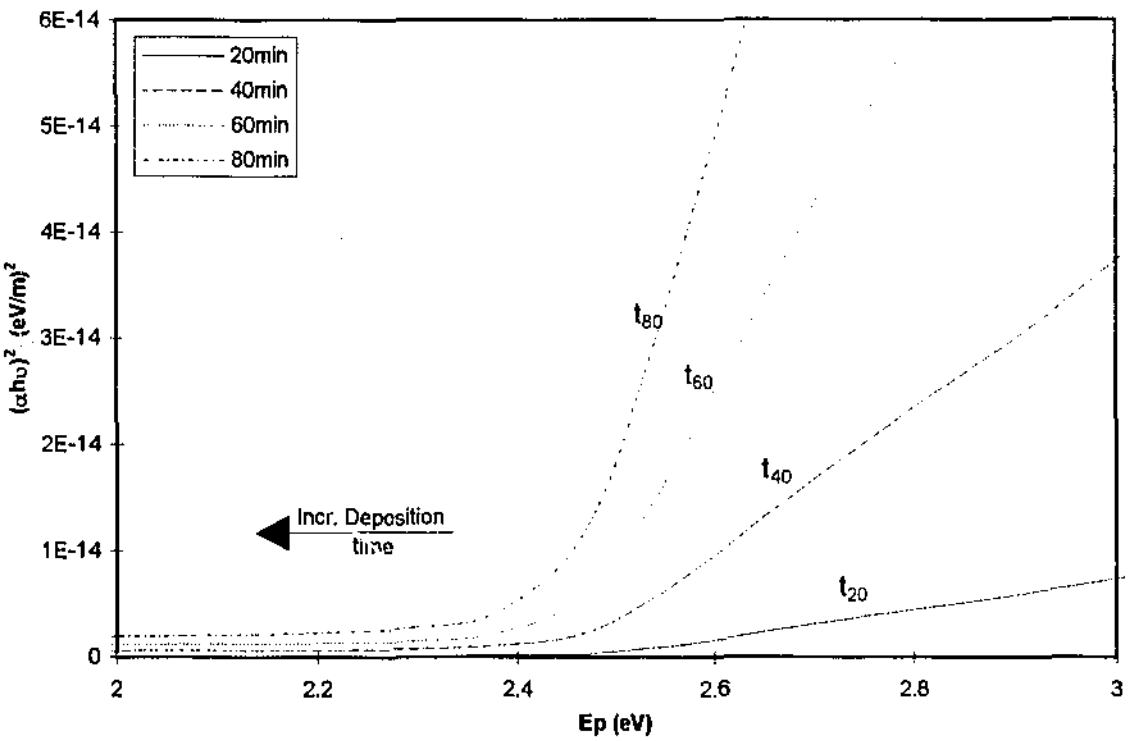

Figure 6.2: Absorption Coefficient plot of $(\alpha E)^2$ versus photon energy of as deposited CdS thin film.

6.2 OPTICAL DETERMINATION OF MORPHOLOGY

Since film uniformity is direct indication of a films specular nature, it can also provide some indication of the amount of diffuse light as a consequence of the material.
In order to confirm this trend, a Helium - Neon laser as a point source was projected through the sample onto an opaque background and the transmitted image examined. At deposition times ≤ 30min which are at the early stages of film growth, the point source of the laser is not well defined and characterized by a diffuse halo surrounding the point. However, at times t ≥ 30min this point source from the laser evolves into a well defined circular point, absent of the diffuse related defect.

It can be noted that surface morphology may influence the optical properties of films through different scattering mechanisms that require further investigation. In addition to optical absorption, transmittance and specular reflectance, there may be additional diffusion mechanisms. There is a considerable amount of diffuse reflectance observed at the film surface dependent upon the deposition time. Since deposition time can be taken as a as direct indication of the surface morphology of the film, it can be deduced that film morphology effects the optical response.

6.3 EFFECT OF CADMIUM CONCENTRATION ON TRANSMITANCE

The optical transmission curves and the corresponding absorption coefficient curves at different cadmium concentrations is given in Figure 6.3. The films investigated were deposited for duration of 60min under the prescribed conditions.

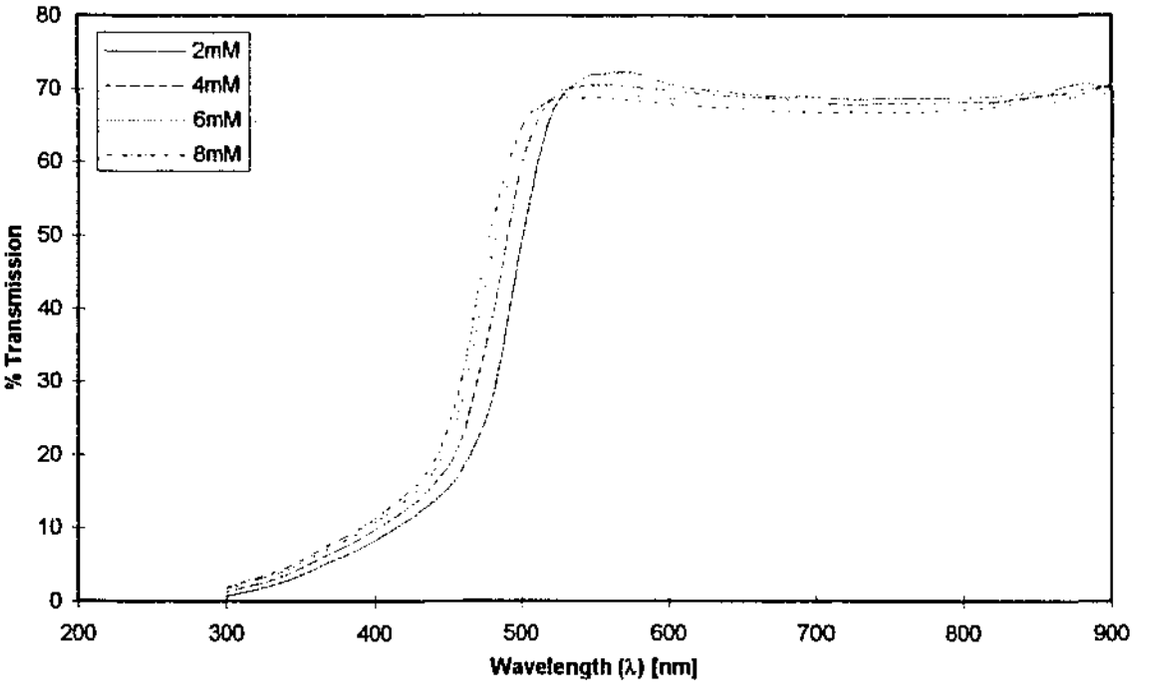

Figure 6.3: Influence of cadmium concentration on the optical characteristics of the film. Deposition Conditions: [TU] = 10mM, [NH_3] = 1.80M and T = 60°C

Figure 6 shows that at increasing cadmium concentrations from 0.002M to 0.01M, there is a marginal change in transmission as a consequence of increased film thickness. However the transmission maxima close to the band edge appears to fluctuate through this concentration transition. Since increased concentrations of the impinging particles increases the rapidity of film growth as observed in Section 5, it may deduced that these deviations are due to the specular uniformity of the film.

Absorption coefficient curves of the influence of cadmium concentration is also shown in Figure 6.4. A summary of the optical and growth characteristics under the concentrations outlined is given in table 6.1.

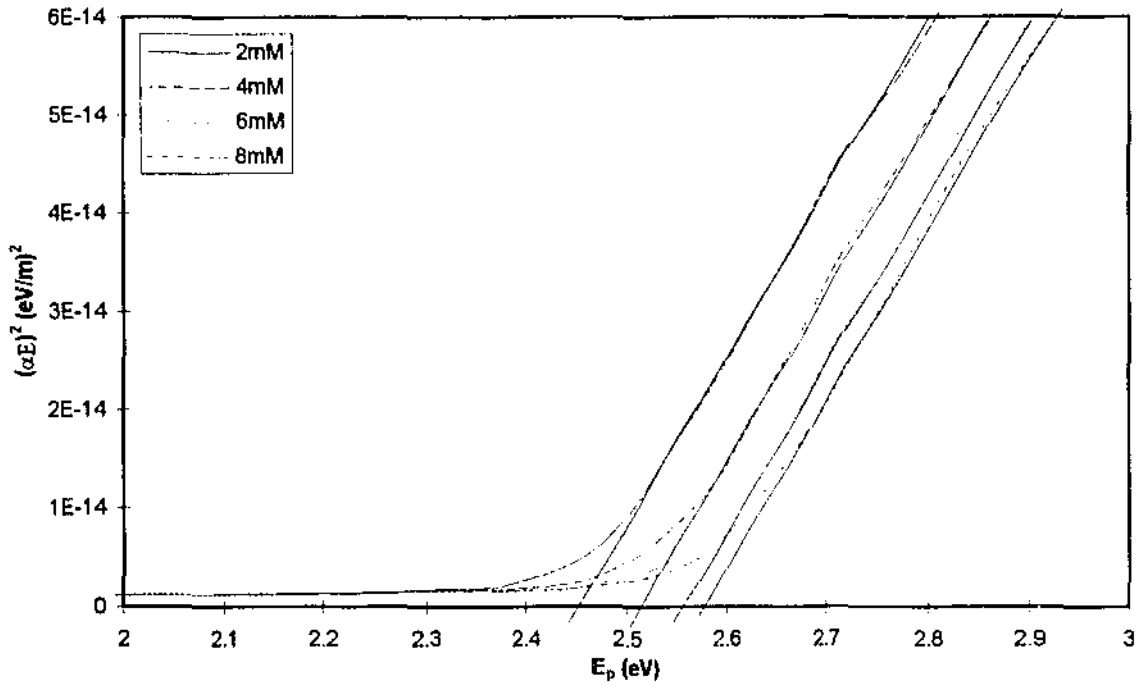

Figure 6.4: Absorption coefficient Plot of $(\alpha E)^2$ versus E_p under the influence of [Cd] concentration.

Table 6.1: Influence of Cadmium concentration on film transmittance

Cadmium Conc. [M]	Deposition Time (sec)	Approx. $\%(T)_{max}$	Impurity Abs. Band	Band Gap (eV)
0.002	60	74	nil	2.45
0.004	60	70	nil	2.51
0.006	60	69	nil	2.56
0.008	60	68	nil	2.58

Note: Band Gap Energy was determined through average of the particular timed run

Interestingly, the observed transmission curves reveal a deviation in the positions of the band edge of the films as a consequence of increased cadmium concentrations. A closer examination of this phenomena in Figure 6.4, reveals that the bandgap energy of 2.46 eV (±0.02 eV), corresponding to the 0.002M [Cd] concentration, is obtained which is larger than the single crystalline value of 2.41 eV (Boer, 1994). Further increases in concentration [Cd] > 0.002M subsequently increases the bandgap energy to ≈2.52 eV, corresponding to 0.004M and reaches a saturation energy of ≈2.58eV (±0.02eV) at 0.008M. Further concentration increases [Cd] > 0.008M has little effect on the band gap energy. This implies that there may be another role that the cadmium species play in the band structure during the deposition.

A possible alternate role of the cadmium species of which no accuracy is claimed, is that the additional Cd vacancies in the lattice through increased concentrations may actively dope the band structure. Since the stoichiometry of the CdS film was not part of this study, it does however, provide another interesting avenue. Formation of bulk compounds in aqueous environments are known to deviate in stoichiometry. However with film deposition processes this phenomena is not entirely known. It is a possibility that during the deposition process where the CdS matrix is formed, the additional Cd vacancies may cause the stoichiometry of the films change. This theory would account for the band gap energy deviations from the crystalline value. In order to investigate this theory it highlights the need for a further investigation using electron diffraction methods in combination with x-ray photoelectron spectroscopy.

6.4 EFFECT OF THIOUREA CONCENTRATION ON TRANSMITTANCE

Unlike the cadmium influence on transmittance, increased thiourea concentration as shown in Figure 6.5 shows that the band gap energy only marginally decreases from the bulk crystalline value. In addition at increased thiourea concentrations the curves show a decrease in transmission maxima at the band edge. This decrease in transmission maxima observed by George *et al.*, (1996) was reportedly an indication of impurity absorption within the bandgap

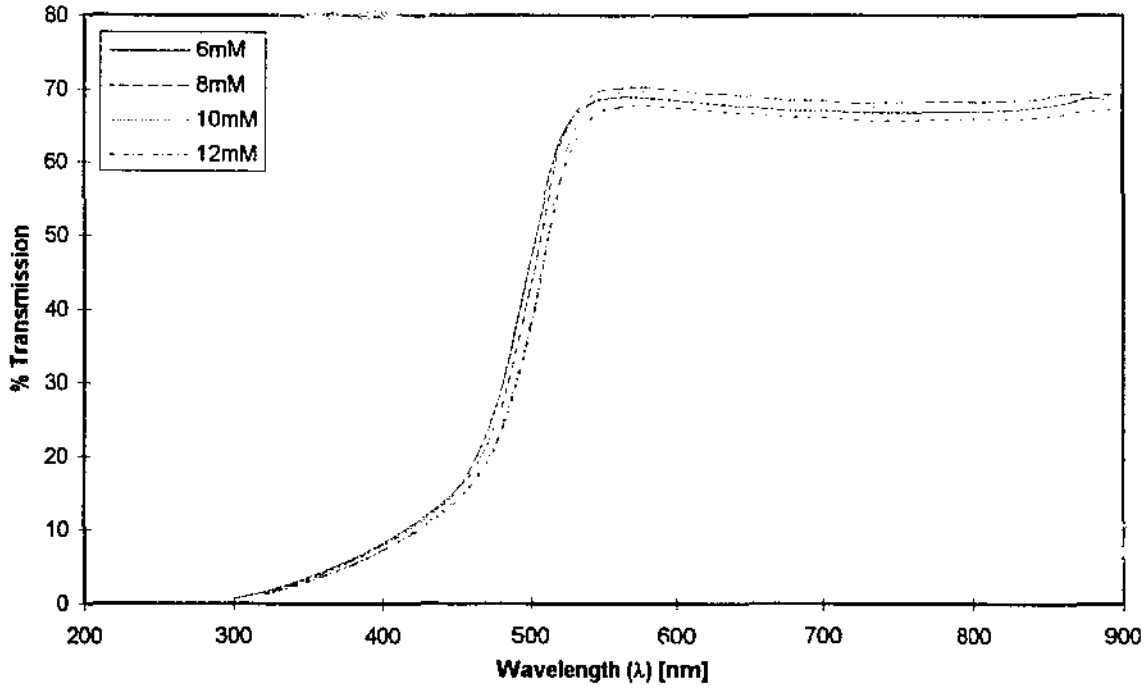

Figure 6.5: Influence of thiourea concentration on the optical characteristics of the film. Deposition Conditions: [Cd] = 2mM, [NH_3] = 1.80M and T = 60°C

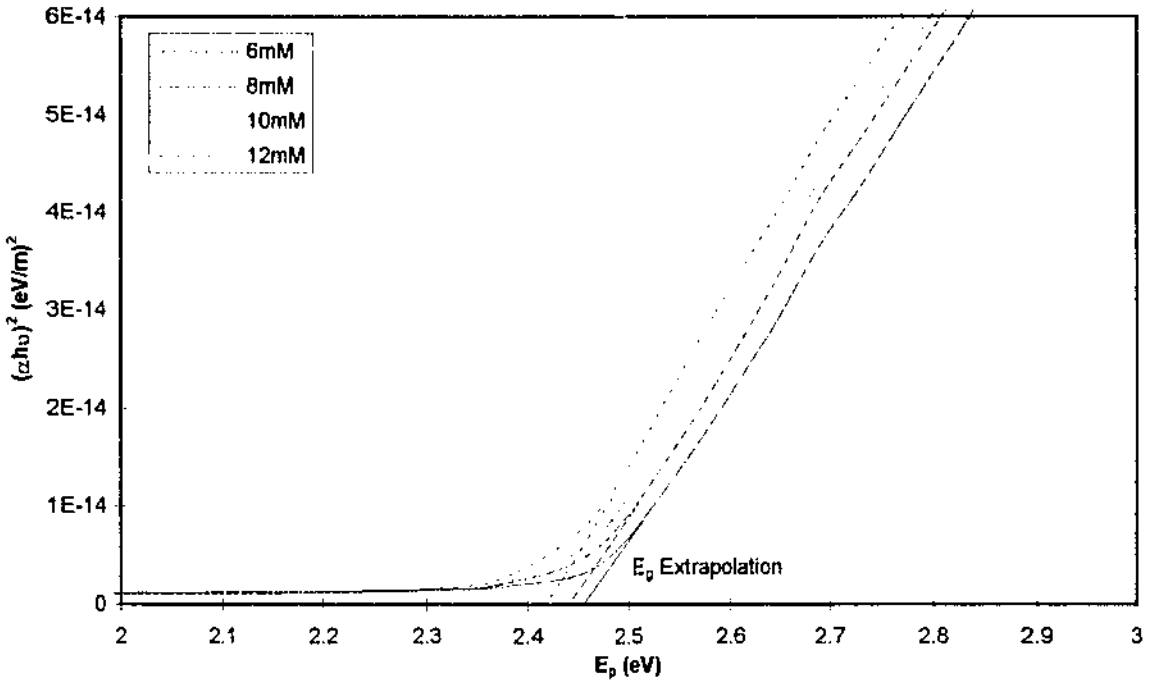

Figure 6.6: Absorption coefficient Plot of $(\alpha E)^2$ versus E_p under the influence of [TU] concentration.

Table 6.2: Influence of Thiourea concentration on film transmittance

Cadmium Conc. [M]	Deposition Time (sec)	Approx. $\%(T)_{max}$	Impurity Abs. Band	Band Gap (eV)
0.006	60	72	nil	2.45
0.008	60	72	nil	2.51
0.010	60	70	nil	2.56
0.012	60	69	nil	2.58

Note: Band Gap Energy was determined through average of the particular timed run

A closer examination of the corresponding absorption coefficient curves show a clear indication that the band gap energy marginally decreases. This decrease in energy from 2.46 eV (±0.02eV) at 0.008M to about ≈ 2.41 eV at 0.012M highlights that sulfur atoms may also play an additional role.

Since S atoms are polymorphic in nature, the additional S vacancies that arise in the lattice have the ability to loose electrons to take up positions in the CdS band structure as traps (E_t).

Using the same analogy as the cadmium influence, additional sulfur atoms that do not actively participate in the formation of the CdS matrix are affected by the influence of dipoles generated by lattice defects. It is these defects that attracts sulfur atoms which as a result caused them to change.

6.5 INFLUENCE OF [In] DOPING

In this section the CdS thin films investigated have their band gap energy modified by the introduction of the [In] impurity. It is this impurity that is of keen interest as it is the most common dopant used in creating n-type CdS window layers in device fabrication. The effect of the introduction of In atoms on transmittance is given in Figure 6.7. In addition a summary of the optical related data is also given in Table 6.3.

When the semiconductor is doped with indium, the optical characteristics of the change owing to the formation of an impurity energy level in the band gap. This is reflected in the optical transmittance spectra of the film. When there is doping by [In] atoms in the range of 10^{18} - 10^{19} atoms·cm^{-3}, the cut-off wavelength is different to that corresponding of the intrinsic case.

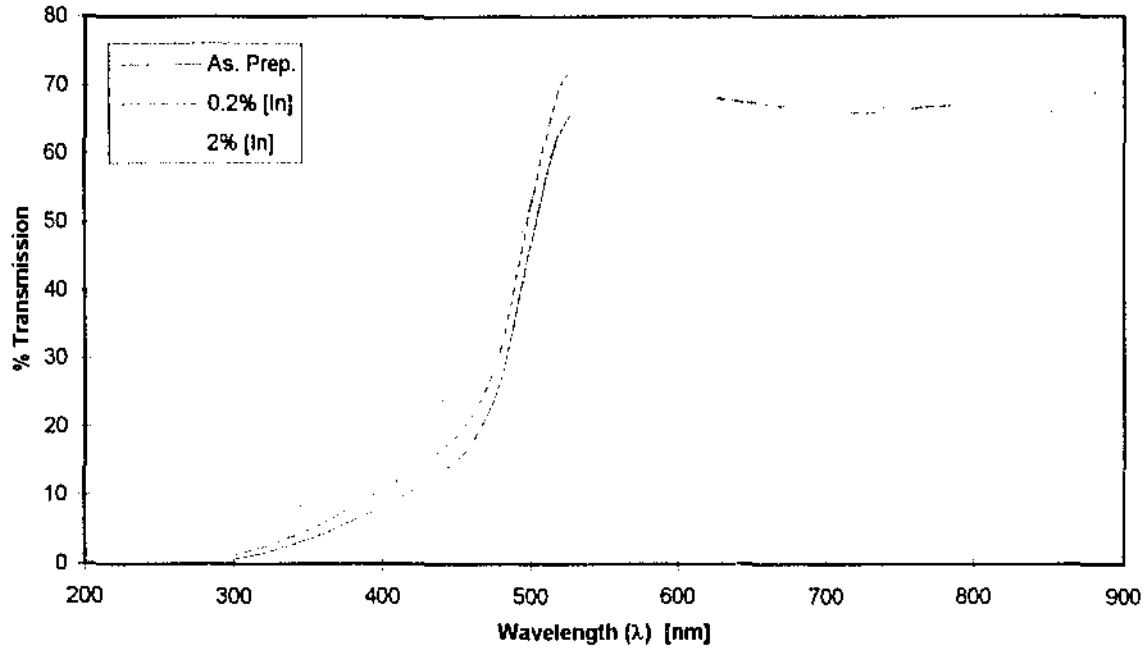

Figure 6.7: Influence of In dopant atoms on film transmittance. Deposition Conditions: [Cd] = 2mM, [TU] = 0.01M, [NH_3] = 1.80M at 60min for T = 60°C

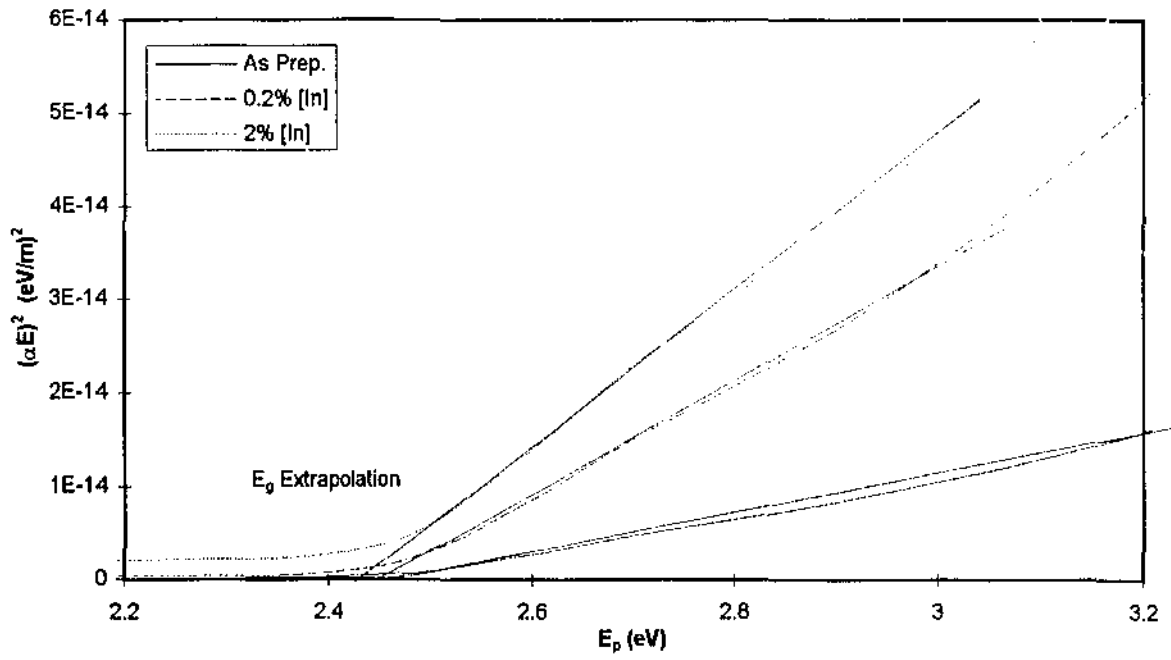

Figure 6.8: Absorption coefficient Plot of $(\alpha E)^2$ versus E_n doped with [In] atoms.

Table 6.3: Influence of Indium [In] concentration on film transmittance

Sample	[In] Conc. (atoms·cm^3)	Approx. %(T)$_{max}$	Impurity Abs. Band	Band Gap (eV)
CdS	-	68	-	2.46
CdS:In [0.2%]	10^{18}	75	-	2.44
CdS:In [2%]	10^{19}	62	>509nm	2.42

Note: Band Gap Energy was determined through average of the particular timed run

The transmittance curves corresponding to as prepared CdS and the compensated cases (CdS:In) in Figure 6.51 clearly show that In concentrations < 10^{18}atoms·cm^{-3} marginally affect the optical transmittance.

Conventional doping via post-deposition treatments at high temperatures has been accompanied by a distinct broad energy absorption edge on the transmission spectrum. It is this defect that indicates the predominance of free carrier absorption due to impurity states of indium and other possible indium based complexes. Identification of these impurity states will be discussed further and analysed in the x-ray diffraction characterization chapter.

Unlike previous methods of doping via thermal diffusion of indium (George *et al.*, 1995), our doped films exhibit few defects in the optical behaviour. It is this achievement that is unique to our study, that indicates a major turning point has been reached in producing extrinsic materials. Doping films via *insitu* methods with impurity concentrations $N_d \leq 10^{18}$ atoms·cm^{-3}, exhibit a small maxima transmittance peak at the band edge. Concentrations > 10^{18} atoms·cm^{-3} exhibits a degradation behaviour of this transmittance peak which. It is possible that this is due to a greater proportion of indium impurities and

the formation of alloyed CdS (i.e. InCdS). This aspect that allows a greater proportion of light to be transmitted, is desirable for sensor device fabrication.

6.6 INFLUENCE OF AIR ANNEALING

The transmittance characteristics of the CdS films resulting from post-deposition annealing at 395°C for various durations is given in Figure 6.9. The transmittance maxima of the annealed films deviate from the band edge characteristic of untreated films to higher wavelengths in no ordered fashion.

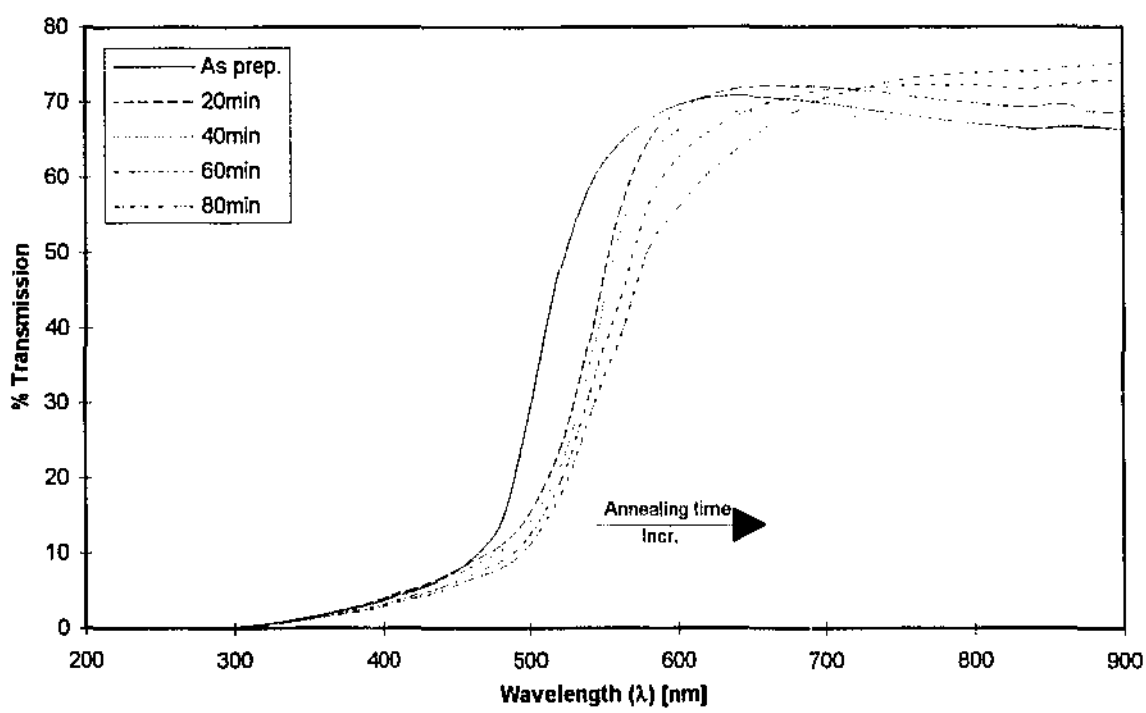

Figure 6.9: Optical transmittance spectra of CdS annealed films at 395°C.

Deposition Conditions: [Cd] = 2mM, [TU] = 10mM [NH_3] = 1.80M and T = 60°C

Also these curves exhibit a broad energy absorption edge, located close to the band edge of the transmission curves, indicating the presence of impurity based free carrier absorption. Since this phenomena is a significant presence in thermal diffusion (George *et al.*, 1996) it is probable that oxidized CdS based impurities are present in the sample.

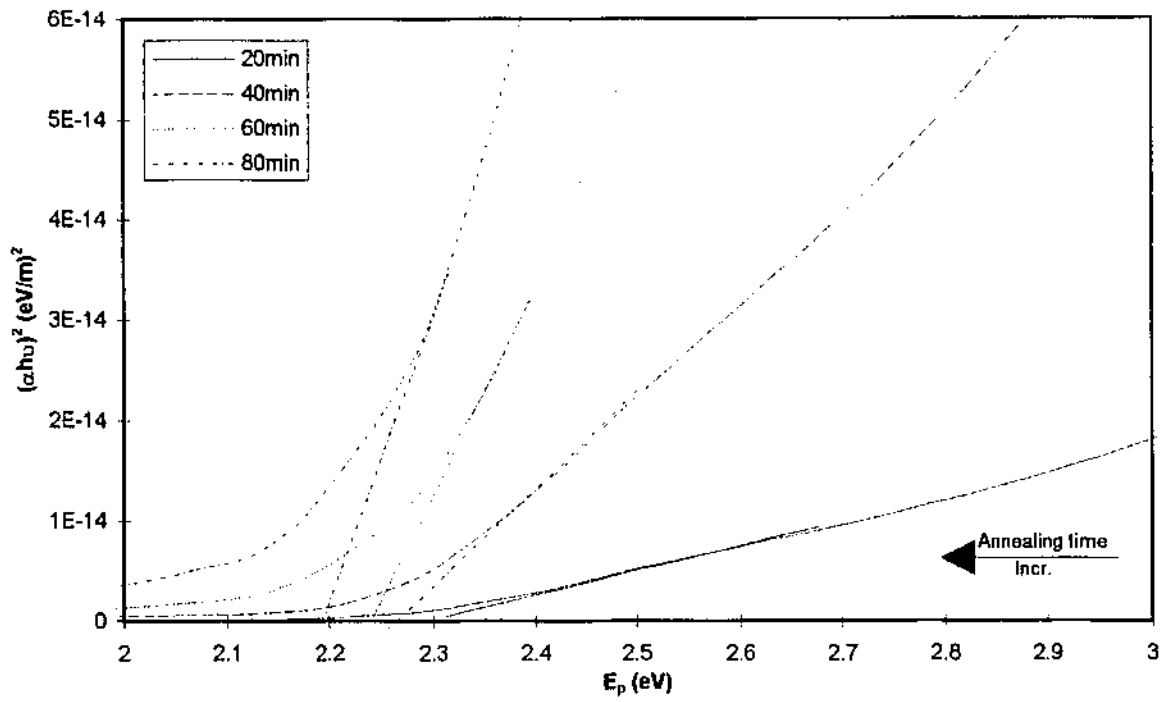

Figure 6.10: Absorption coefficient Plot of $(\alpha E)^2$ versus E_p for annealed films.

Table 6.4: Influence of Air Annealing on Film Transmittance

Sample	Annealing Time (min)	Approx. %(T)max	Impurity Abs. Band	Band Gap (eV)
CdS	-	70	nil	2.46
CdS:Ann	20	72	580 - 730nm	2.31
CdS:Ann	40	69	580 - 730nm	2.28
CdS:Ann	60	72	580 - 730nm	2.24
CdS:Ann	80	75	580 - 730nm	2.19

It is evident from the optical spectra and the corresponding $(\alpha E)^2$ plot that air annealing causes a reduction in the band gap energy of CdS. However this apparent decline in band gap energy, also produces an increased transmittance at the band edge. This accompanied increase on average by about 8 - 12% is common throughout films investigated.

The optical band gap of the as deposited polycrystalline semiconductors is generally higher than the bulk crystalline value of 2.41eV (Boer, 1990), depending upon the deposition environment. However with post-deposition annealing, the band-gap energy of the films decreased significantly. This increase in transmittance at the band edge and its subsequent decrease in band gap energy may be due to the partial conversion of CdS into other compounds. Since the films are air annealed, atmospheric oxygen and water vapour may be absorbed and diffused into the film to interact with the atomic structure.

The formation of cadmium oxide CdO and cadmium sulfate $CdSO_4$ related compounds is probable owing to the presence of atmospheric oxygen and water vapour. This conversion or interaction with impurities was confirmed by an irreversible change in the film's colour from yellow (CdS) to brown then to orange (CdS:CdO:$CdSO_4$).

It is evident from Figure 6.9 that heating CdS:In films at for a time period $t_{anneal} \leq 20$min the film transmittance is > 71% and the band gap energy decreases respectively. This indicates that the In impurity may have undergone a partial conversion into an oxide and the remaining In atoms may have diffused further into the CdS matrix. This oxidation and its subsequent interaction would promote the recrystallization of CdS (George *et al.*,

1995), accounting for the increased transmittance. To further confirm this possible process, a suitable spectroscopy such as XPS coupled with depth profiling would show and identify if any compositional changes occur.

During the early stages of heat treatment, the In impurity could have also diffused into the surface layer because of its low melting point. As a consequence of this diffusion the In atoms would have been subjected to a variety of oxidation processes involving oxygen and other CdS related compounds. Since grain boundaries in polycrystalline films provide easy pathways for the diffusion of impurities, the indium would have diffused faster into the CdS matrix with this heat treatment.

6.7 FOURIER TRANSFORM INFRARED (FTIR) BEHAVIOUR

Because of its wide energy range, infrared radiation interacts with most features of semiconductors. Through interference effects, it is also sensitive to the geometry of semiconductor structures. Infrared spectroscopy over the range 10 - $10^4 cm^{-1}$ can determine band gap, layer thickness, impurity type and dopant concentration. In CdS, for instance, it is essential to know the presence of oxygen and its concentration in the thin film due to annealing, without subjecting the film to destructive analysis. It is this information that provides a picture to the materials modified device characteristics as its performance.

Since infrared behaviour can stimulate impurities, the occurrence of impurity transitions can be best described using the hydrogenic model. When the impurity radius (e.g. O & In) covers several lattice constants of the host matrix, its potential is nearly the same as the Coulomb potential due to a net nuclear charge of one proton. This is like a hydrogen atom whose electron has mass m^*, immersed in a medium with dielectric constant ε. Both factors are readily inserted in the Bohr model for hydrogen , yielding an ionization energy (Perkowitz, 1993)

Since the electron from an In atom can displace an electron from the Cd atom in the lattice, for the purposes of this study we can make this assumption in determining impurity transitions.

The chemical purity of the substrate surfaces and the corresponding CdS thin films has been investigated by Fourier Transform Spectroscopy (FTIR). The FTIR absorbance of the silicon substrate (pattern [1]), CdS as prepared, (pattern[2]), CdS:In (pattern[3]), annealed as-prepared CdS (pattern [4]) is shown in Figure 6.11.

As observed by the silicon and respective CdS signals (patterns [2] to [4]) there is the presence of [C-O] stretches in the range 1260 - 1000cm^{-1} indicating possible vibrations due to an alcohol. Since part of the post deposition annealing cleaning involved uses an ethanol mixture is likely air of the samples may must have produced a fine on the surface of the film and the substrate. Interestingly the annealed CdS film (pattern [4]) also shows the presence of a [C-C] stretch, which supports this idea.

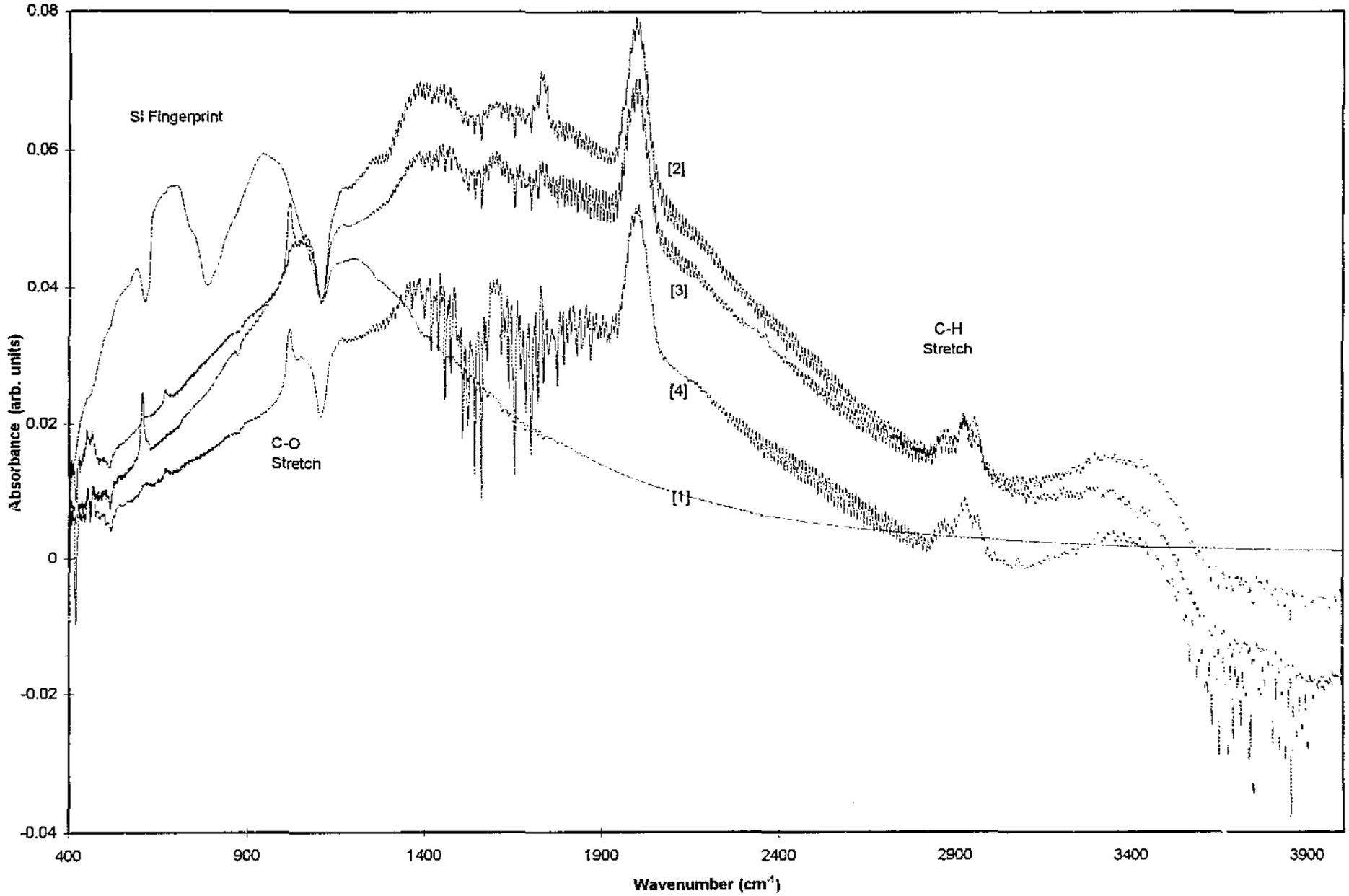

Figure 6.11: Fourier Transform Infrared (FTIR) Absorbance Spectra for CdS based Films.

It is probable that the fine film resulting from ethanol treatment may have been coated on to directly by CdS through the deposition. Hence this would imply that further oxygen related impurities associated with high annealing temperatures (e.g. $CdSO_4$ & SO_2) that diffused through the CdS layer may of further interacted with this alcohol based impurity.

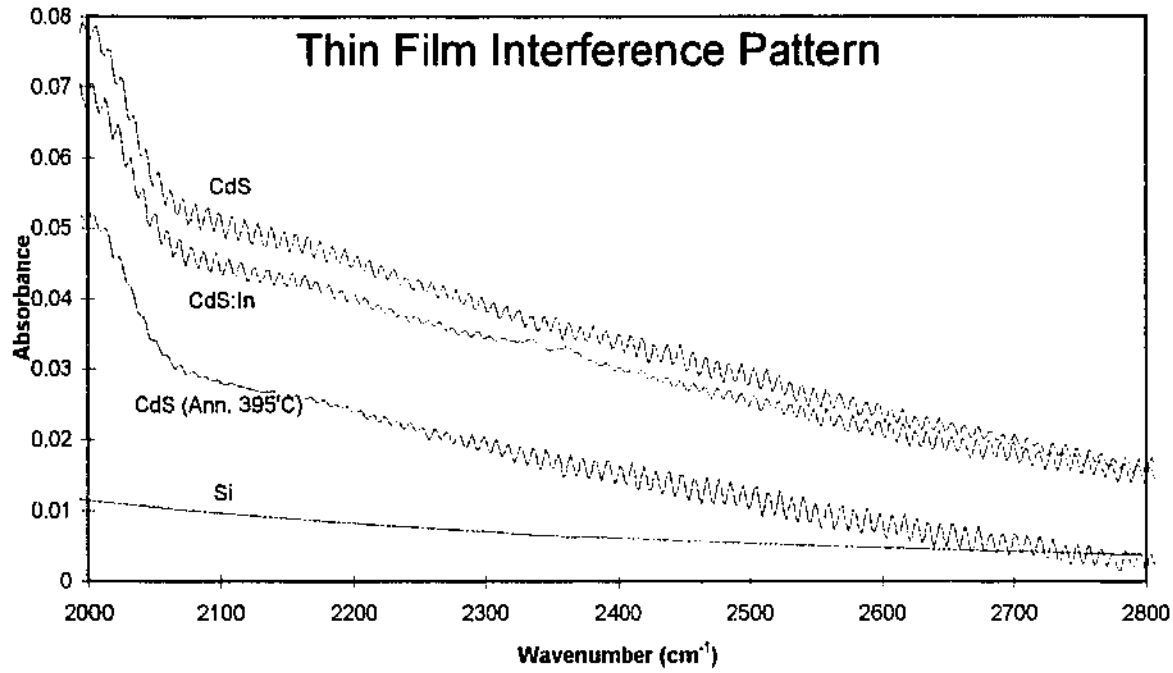

Figure 6.12: FTIR absorbance spectra of silicon and CdS related films

Interestingly, throughout the absorbance patterns [2] to [4] (Figure 6.11) is the common presence of what appears to be a sinusoidal like interference pattern. This interference as shown in Figure 6.12 pattern is not isolated or periodic, it is however present in CdS related films indicating it is not a random phenomena. This CdS related phenomena has not been reported previously and it highlights the need for a detailed study using this technique.

7. X-RAY DIFFRACTION

The crystallographic properties of the chemically deposited CdS, as-prepared and under various conditions deposition and annealing have been investigated by x-ray diffraction using CuK_{α} radiation. This analysis allows us to elucidate the mechanisms that control the crystal structure of CdS films deposited under different conditions. The presence of impurity phases due to the deposited CdS matrix and also the post-deposition treatments (i.e. air annealing) has been reported (Borges *et al.*, 1990). However, there has been little correlation to semiconductor behaviour as a result of these changes.

7.1 EFFECT OF AIR ANNEALING ON FILM CRYSTAL STRUCTURE

From the x-ray diffraction patterns shown in Figure 7.1, CdS exists in two crystalline phases the hexagonal and cubic. The hexagonal phase is the more stable or the preferred orientation as the post-deposition annealing temperature is increased. The polycrystalline hexagonal and cubic forms of CdS form random orientations upon deposition and show many strong diffraction peaks the relative intensities and values of which are summarized in Table 7.1.

The XRD study of the samples indicate the dominant presence of a peak at $2\Theta \approx 26.5°$, indicating a strong preferred orientation. This broad peak at a closer examination using a Gaussian Transform reveals three coalesced peaks; an intense (002) and (100) hexagonal reflections and a marginally less intense (111) cubic CdS peak These two major forms of coexistant CdS phases determine the electrical properties of the material. It therefore can be deduced that the dominance of one phase (i.e. hex or cubic) over the other form a distinction in electrical properties. This is in agreement of previous works of Nakanish *et al* (1994).

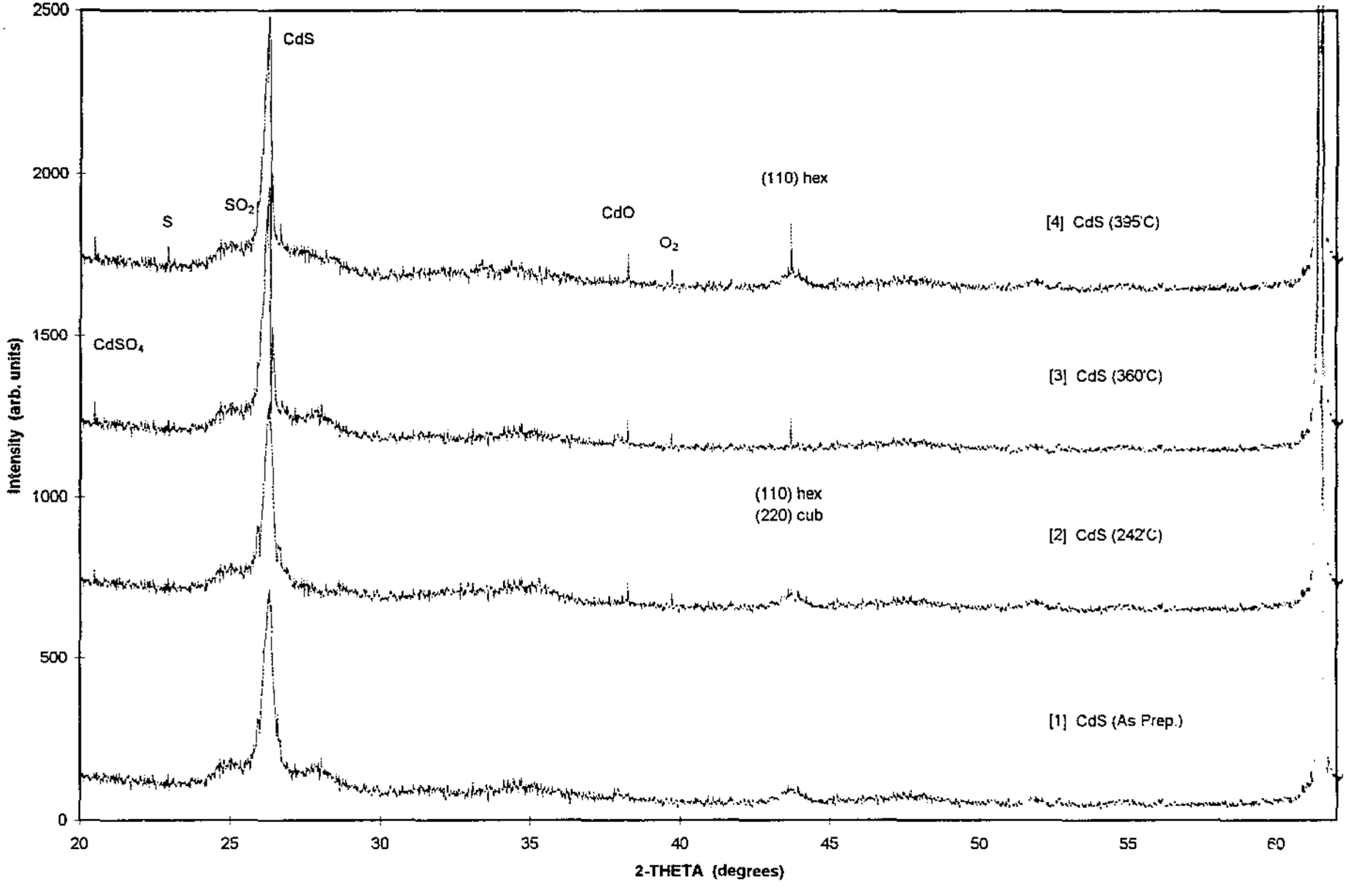

Figure 7.1: X-ray Diffraction Patterns of CdS under the influence of various annealing temperatures.

Table 7.1: Diffraction pattern of CdS at various annealing temperatures using CuKα radiation

SAMPLE	EXPERIMENTAL			REFERENCE JCPDS-ICDD				
	2Θ	d	I	2Θ	d	I		Assign
As Prep.	24.5	3.63	49	24.81	3.59	62	(1 0 0)	CdS HEX
	26.5	3.36	80	26.51	3.36	91	(0 0 2)	CdS HEX
	26.5	3.36	72	26.50	3.36	100	(1 1 1)	CdS CUB
	43.6	2.07	83	43.68	2.07	110	(1 1 0)	CdS HEX
	43.9	2.06	56	43.90	2.06	220	(2 2 0)	CdS CUB
242	26.5	-	-	26.50	-	-	-	CdS H/C
	43.8	-	-	43.80	-	-	-	CdS H/C
	38.4	2.34	52	38.29	2.35	88	(2 0 0)	CdO CUB
	39.7	2.27	22	38.34	2.35	100	(1 0 1)	O_2 HEX
360	26.5	-	-	26.50	-	-	-	CdS H/C
	43.8	-	-	43.80	-	-	-	CdS H/C
	20.4	4.35	23	20.45	4.34	68	(1 0 0)	$CdSO_4$ HEX
	25.9	3.44	14	25.73	3.46	23	(1 1 1)	SO_2 HEX
395	26.5	-	-	26.50	-	-	-	CdS H/C
	43.8	-	-	43.80	-	-	-	CdS H/C
	22.9	3.88	42	23.08	3.85	98	(2 2 2)	S

Note: CdS H/C indicates intensity change between hexagonal and cubic phases

Interestingly, while the essential peaks from the untreated sample [1] remained, the intense peak at $2\Theta \approx 26.5°$ further resolved into two distinct peaks through patterns [2] to [3]. This broad peak area revealed an emerging sharp and intense (002) hexagonal phase at $2\Theta \approx 26.48°$ and a significantly reduced (111) cubic phase at $2\Theta \approx 26.54°$. As the annealing temperature progressively increased the distinction between the hexagonal (110) and cubic (220) reflections forming a broad band at approximately $2\Theta \approx 43.8°$. It is evident that this hexagonal and cubic broad band underwent an evolution, changing from a (110)/(220) mixture at temperatures $T < 360°C$ to predominantly hexagonal (110) at $T > 360°C$. The absence of any other intense cubic related phases, such as (220) at these temperatures implies a strong (002) preferred orientation of the grains parallel to the substrate. It this hexagonal phase of CdS that is desirable for II-VI heterojunction solar cells.

The broadening of the diffraction peaks of the untreated films can clearly be seen in Figure 7.1, indicating that the grain size of the film increases with increasing annealing

temperature. In addition, the amount of [S^{2-}] ions in the film is an important factor in determining the formation of a dominant hexagonal phase.

Increasing the annealing temperature of the films evidently introduces a significant amount of impurity phases. As seen in Figure 7.1, the XRD patterns [2] to [4] conforming to the annealed films show a significant change in the composition compared to that of the untreated film [1].

In pattern [2], corresponding to the annealed film at T ≈ 242°C the (200) and (101) hexagonal reflections of CdO and (O_2) at 2Θ ≈ 38.4° and 39.7° respectively arise. In addition to this, as a result of the increasing CdO proportion, there is also a corresponding marginal decrease in the CdS peak intensity at ≈ 26.5°. It is also evident that the (110) hexagonal and (220) cubic broad band associated with CdS at 2Θ ≈ 43.8° begins to form a distinction between the respective phases.

Patterns [3] to [4] resemble that of pattern [2], however the peak intensities appear to increase marginally as a consequence of the higher converted CdO proportions. Interestingly, patterns [3] to [4] at annealing temperatures T ≥ 360°C show the emergence of a (100) hexagonal reflection of $CdSO_4$ at 2Θ ≈ 20.4°, and a (111) hexagonal reflection at 2Θ ≈ 20.4° corresponding to SO_2.

Unique to pattern [4] at T ≈ 395°C the presence of a (222) reflection due to sulfur atoms at 2Θ ≈ 22.9° is evident. This is an indication of the "out diffusion" process occurring within the film (George *et al* ., 1996). As observed in XRD patterns [3] and [4] the sulfur atoms can indiscriminately dope the existing band structure by itself or in combination with other compounds (i.e. SO_2).

The presence of these impurities in [3] and [4] at these temperatures indicate further reaction processes within the film are taking place as result of the higher thermal energies. These peak intensities found in pattern [4], as with the previous case, increase marginally

owing to a greater proportion of these conversions. As a result it can be deduced that the thermal energy provided through annealing is integral for the breaking of CdS bonds and the formation of others (e.g. $CdSO_4$ & CdO).

It is seen that among the existing hexagonal and cubic phases there are reflections related to CdO, $CdSO_4$, O_2 and SO_2 impurities. The CdO and the $CdSO_4$ phases constitute the impurity changes that take place within the film at high temperatures. In case [2] the CdO impurity phase is present, however the $CdSO_4$ impurity is negligible. At annealing temperatures > 242°C, the (100) hexagonal sulfate phase is increased considerably and the peak intensity corresponding to the CdS phase is decreased. This indicates that increasing the annealing temperatures increases the proportion of impurity phases and their subsequent reactions, leading to a decrease in the CdS present in the samples.

The decrease in film resisitvity (ρ_d) due to annealing as seen in the following electrical properties chapter, can be attributed to the formation of CdO in the film according to:

$$2CdS + 3O_2 \Rightarrow 2CdO + 2SO_2 \qquad [7\text{-}1]$$

In this evident reaction scenario illustrated by pattern [2], conductive CdO is produced, enhancing the electrical properties. The increase in the proportion of the sulfate phase at T > 242°C can be attributed to further oxidation of the CdS according to:

$$CdS + O_2 \Rightarrow CdSO_4 \qquad [7\text{-}2]$$

One particular undesirable feature of annealing at T ≥ 360°C is the cadmium and/or sulfur atoms can undergo "out diffusion". In this process the existing compound breaks down into its constituent atoms which diffuse and are free to interact inside and outside the CdS matrix. As seen in pattern [4] the presence of the (222) sulfur, (101) oxygen and (111) sulfur dioxide seems to conform with this diffusion process and its subsequent reactions. The possible reaction mechanism that occurred at temperatures T > 360°C include:

[1] Thermal breakdown of CdS bonds promoting atom diffusion,

$$CdS + \Delta Heat \Rightarrow Cd^{2+} + S^{2-} \qquad [7\text{-}3]$$

[2] Chemisorbed O_2 interacted with "free" sulfur atoms

$$S + O_2 \Rightarrow SO_2 \qquad [7\text{-}4]$$

7.2 EFFECT OF [In] DOPING ON FILM CRYSTAL STRUCTURE

The x-ray diffraction patterns (Figure 7.3) of the as-prepared films (pattern [1]), and the In doped films (pattern [4]) under similar deposition conditions both share the dominant CdS peak at $2\Theta \approx 26.5°$. These characteristic peaks correspond to the (002) hexagonal and (111) cubic phases of CdS. A summary of the diffraction peaks matched, the relative intensities and d-spacings are summarized in Table 7.2.

It is evident from a comparison between patterns [1] and [2] of Figure 7.2 that there is a strong presence of the (101) indium reflection at $2\Theta \approx 26.5°$. This intensity indicates that the doping process was successful in forcing or capturing the [In] atoms into the CdS matrix. Interestingly, while the essential peaks remain in pattern [2] relative to [1], the CdS peak agglomeration at $2\Theta \approx 26.5°$ appeared to become better resolved as observed in the annealing study. Since both films were produced under similar conditions, the [In] atoms present in pattern [2] must have played a role. This implies that the [In] introduction may have promoted a more structured arrangement to compensate the additional charge. In addition, the absence of any In based compounds in pattern [2] suggests that the impurity was not in sufficient concentrations to actively participate in the CdS matrix construction. That is, In is present in the film as a dopant, and not does not alloy with CdS to form InCdS.

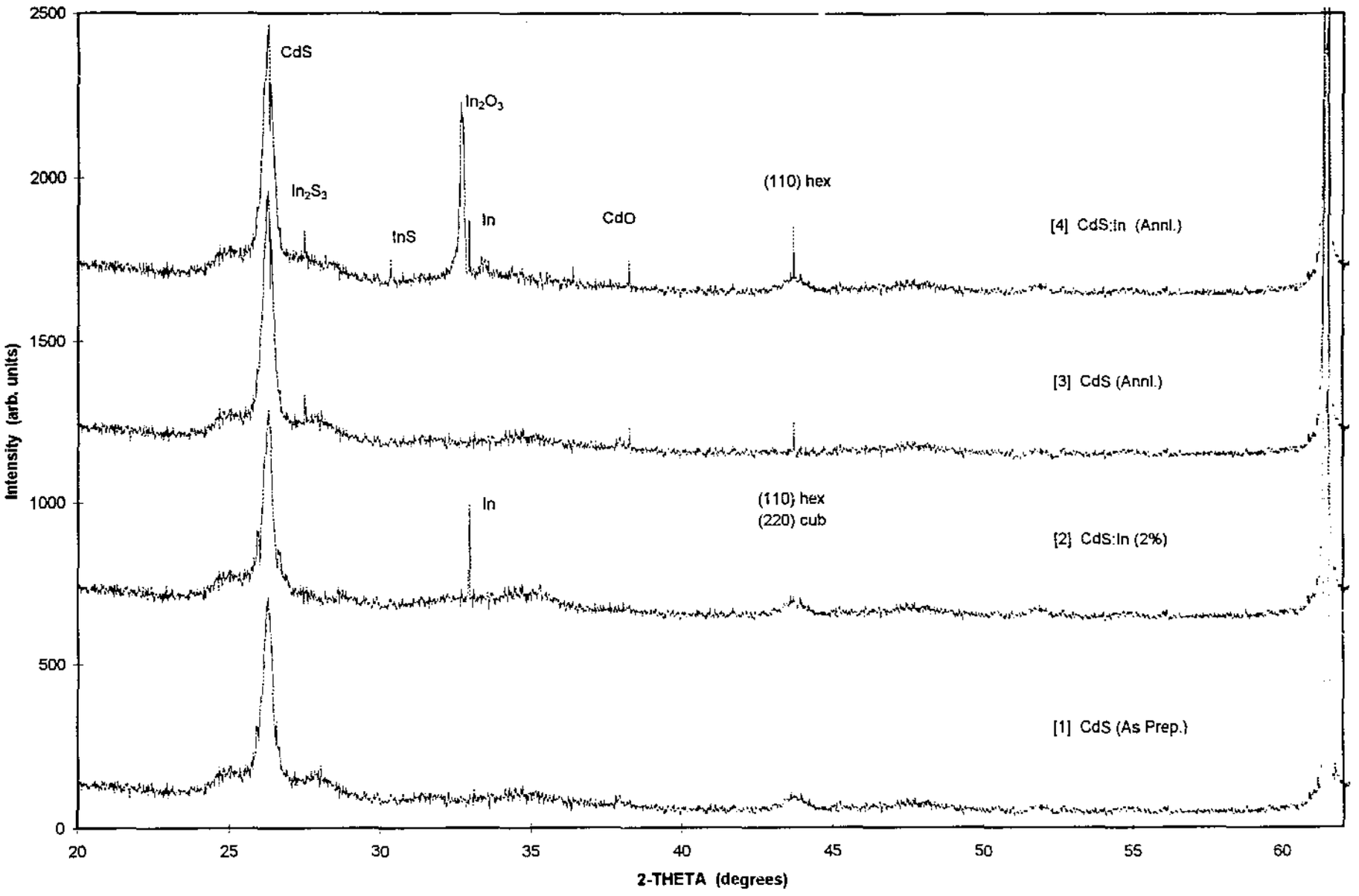

Figure 7.2: X-ray Diffraction Patterns of doped CdS under various conditions.

Table 7.2: Diffraction patterns of CdS and CdS:In (as-prepared and annealed) using CuKα radiation

SAMPLE	EXPERIMENTAL			REFERENCE JCPDS-ICDD				
	2Θ	d	I	2Θ	d	I		Assign
As Prep.	24.53	3.63	49	24.81	3.59	62	(1 0 0)	CdS HEX
	26.48	3.36	80	26.51	3.36	91	(0 0 2)	CdS HEX
	26.54	3.36	72	26.50	3.36	100	(1 1 1)	CdS CUB
	43.6	2.07	83	43.68	2.07	110	(1 1 0)	CdS HEX
	43.92	2.06	56	43.90	2.06	220	(2 2 0)	CdS CUB
CdS:In								
	32.82	2.73	81	32.96	2.71	100	(1 0 1)	In
As Prep.								
(Annl.)	38.32		67	38.29	2.35	88	(2 0 0)	CdO CUB
CdS:In								
(Annl.)	27.44	3.25	41	27.82	3.20	100	(1 0 9)	In_2S_3 TETR
	30.26	2.95	81	30.26	2.95	100	(1 1 0)	In_2O_3 HEX
	32.66	2.74	61	32.62	2.74	95	(1 1 0)	InS
	36.64	2.47	15	36.33	2.47	21	(0 0 2)	In

As observed in XRD pattern [2] (corresponding to CdS:In) and the annealed version, (pattern [4]), the presence of In and In based compounds have undergone a significant change in composition and purity. Pattern [2] reveals the presence of an intense and pure (101) indium reflection at $2\Theta \approx 32.82°$ which is the characteristic dopant used in our n-type materials. The presence of this peak decreases under annealing (as shown in pattern [4]) as a consequence of "out diffusion" and further reactions with other impurities. Since the melting point of indium is ≈ 147°C (Aylward & Findlay, 1994), and the annealing temperature is 220°C, it is therefore highly susceptible to diffusion processes, making the observed impurity combinations possible.

Interestingly, pattern [4] reveals the emergence of indium based impurities such as; a (110) InS reflection at $2\Theta \approx 30.26°$, a (110) In_2O_3 peak at $2\Theta \approx 32.66°$ and a (100) In_2S_3 reflection at $2\Theta \approx 27.44°$. The presence of these impurities is a result of a combined In diffusion and interaction process. As a consequence the growth of these impurities can be linked to the decline in intensity of the (101) metallic indium reflection. Since

temperatures T ≥ 220°C promote this type of combined diffusion and interaction process, a possible reaction scheme that describes the formation of indium oxide includes:

[1] Diffused Indium interacts with chemisorbed O_2,

$$4In + 3O_2 \Rightarrow 2In_2O_3 \qquad [7\text{-}5]$$

The XRD pattern of the annealed CdS:In does show that the CdS peak becomes narrower, indicating improved crystallinity of the film. In addition to the above process, some of the remaining In is diffused into the CdS matrix promoting the recrystallization of CdS.

However the indium sulfide based compounds differ in that rudimentary InS is used as a platform where additional sulfur atoms can attach. Since sulfur is a polymorphic atom it would theoretically loose electrons in order to create a bond. The possible mechanism based on XRD pattern recognition analysis include:

[1] Thermal breakdown of CdS diffusing [S] atoms,

$$CdS + \Delta Heat \Rightarrow Cd^{2+} + S^{-x} + xe^{-} \qquad [7\text{-}6]$$

where x indicates the polymorphic nature of sulfur.

[2] Interaction of In atoms with S atoms forming the base compound,

$$In + S \Rightarrow InS \qquad [7\text{-}7]$$

[3] Further interaction of InS with polymorphic [S] atoms.

$$2InS + S \Rightarrow In_2S_3 \qquad [7\text{-}8]$$

Further indium sulfide based complexes were evident, however in negligible quantities that could be confused as background noise. However it is feasible that at higher temperatures $T >> 220°C$, these complexes may exist. In order to verify this existence and of other impurity complexes further studies using differential thermal analyzers (DTA) would be required.

8. ELECTRICAL PROPERTIES

In this section, the effect of film thickness and doping on the electrical resistivity of chemically deposited CdS films will be discussed. In addition the effect of post-deposition air annealing and the temperature dependence of resistivity is also discussed in correlation to film structural changes.

8.1 EFFECT OF FILM THICKNESS ON FILM RESISTIVITY

The dependence of resistivity on film thickness is shown in Figure 8.1. There is a clear and rapid decrease in film resistivity with increasing film thickness up to 500nm, and then a gradual decrease was observed. The variation of the resistivity with film thickness can be correlated to the structural properties of the prepared films. Although the size of the crystallites introduces an effect on the resistivity, in this case, the effect is negligible since the majority of films are ≤ 0.8 μm thick. The increase in the degree of the (111) hexagonal orientation seems to have a considerable contribution on the sharp decrease in film resistivity. This trend of increased preferred orientation related to the film thickness is supported by the works of Ramadan *et al.*, (1990).

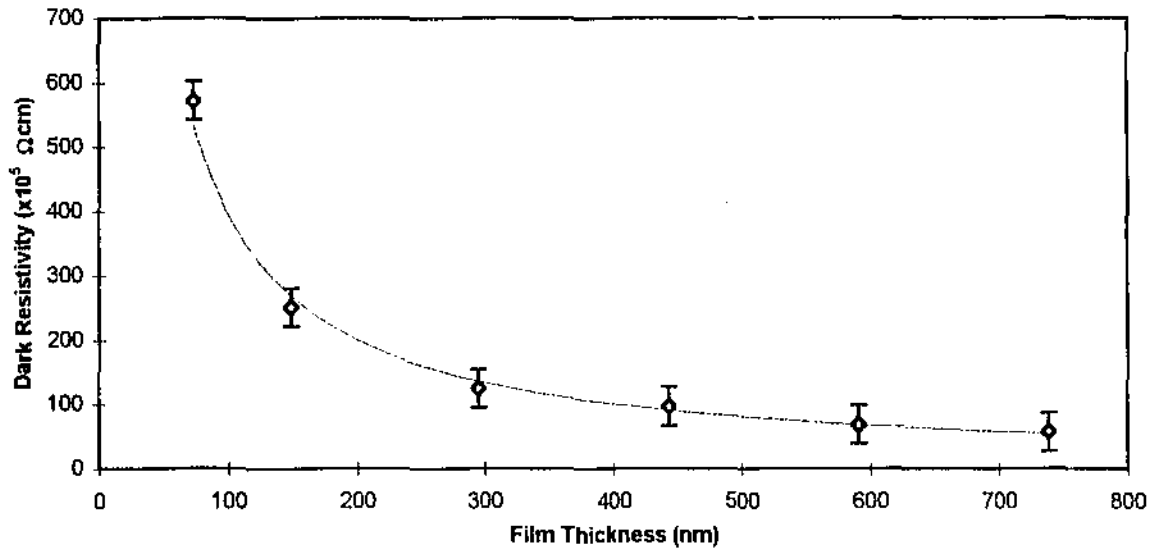

Figure 8.1 Dependence of Dark Resistivity on film thickness

8.2 MODIFICATION OF ELECTRICAL PROPERTIES BY [In] DOPING

The photoconductive characteristics of chemically deposited CdS, with and without In doping, is shown in Figure 8.2. A summary of the computations involving the determination of the relative conductivities (σ_d,σ_p) and the photosensitivity ($S \approx \sigma_p/\sigma_d$) is provided in Table 8.1. There is an observable increase in the dark and photoconductivity when the CdS films are doped in-situ during the deposition, as shown in Figure 6.3. This effect appears to be attributed to the increase in the In dopant concentrations within the CdS matrix.

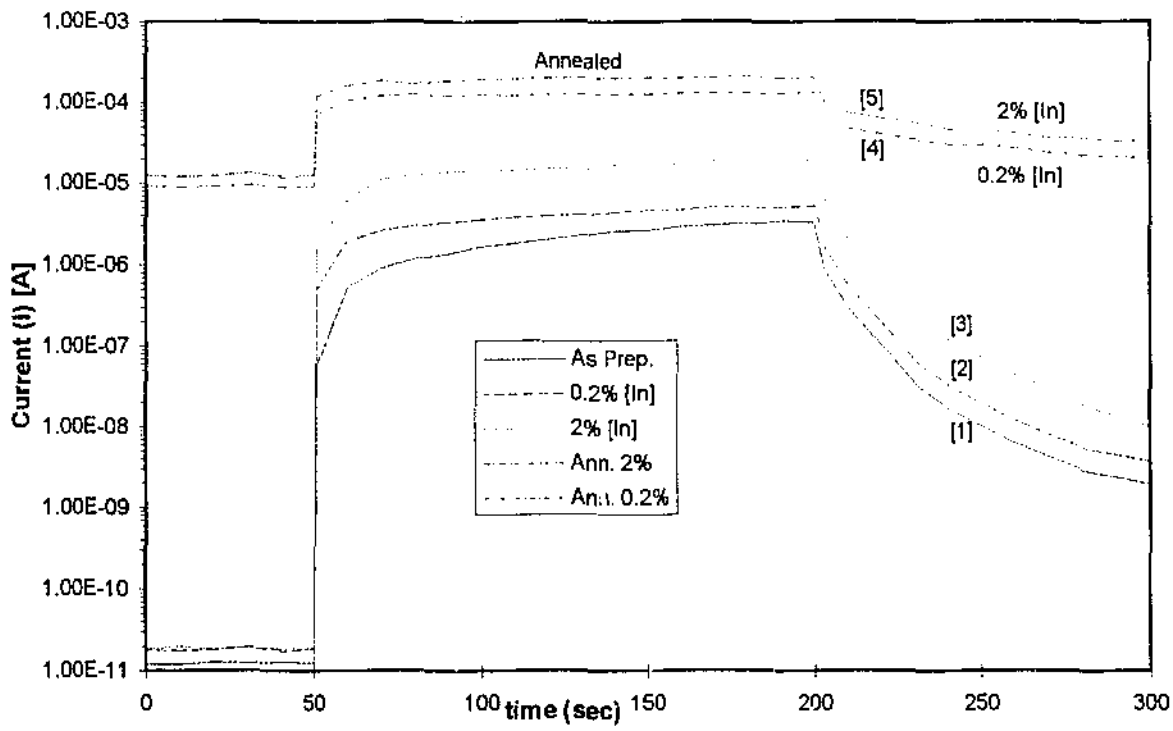

Figure 8.2: Photocurrent response versus time of CdS and CdS:In films heated at 220°C for 60min. Note: The photoresponse (i.e. photocurrent) gives a direct indication of the photoconductivity (σ_p).

Table 8.1: Dark and photoconductivity parameters of CdS:In and CdS thin films

Sample	[In] Conc. (atoms·cm^3)	Ann. Temp (°C)	R_d (Ω)	σ_d (Ω^{-1} cm^{-1})	R_p (Ω)	σ_p (Ω^{-1} cm^{-1})	S (σ_p/σ_d)
CdS	-	-	7.22×10^{11}	3.12×10^{-07}	4.11x106	0.0612	1.76×10^5
CdS:In	10^{18}	-	4.94×10^{11}	4.57×10^{-07}	2.22×10^6	0.169	3.70×10^5
"	"	220	9.82×10^5	0.230	7.17×10^4	5.24	22.8
CdS:In	10^{19}	-	4.73×10^{11}	4.77×10^{-7}	5.88×10^5	0.639	1.34×10^6
"	"	220	7.19×10^5	0.314	4.60×10^4	8.14	25.9

As seen from the photoresponse curves in Figure 6.3, doping the films with In atoms (i.e. CdS:In) only has a marginal influence on the dark photoconductivity (σ_d). Compared to that of the undoped sample, (curve [1] in Fig 6.3), the effective magnitudes differ little from 10^{-10} $\Omega^{-1}\cdot cm^{-1}$. This suggests that dark conductivity is unaffected by in-situ In doping. It is this property which enables the photosensitivity of the film to be enhanced that makes it a desirable process for producing sensor related devices.

Interestingly, the photoconductive region of the doped films (curves [2] &[3]) shows a significant change in the films electrical properties compared to that of the undoped film under illumination. Doping the films with In concentrations of 10^{18} and 10^{19} atoms·cm^3 (i.e. 0.2% and 2%) has had a positive influence on the film photoconductivity. The photoconductivity increased from 0.0550 $\Omega^{-1}\cdot cm^{-1}$ for the intrinsic sample to ~ 0.2 and ~0.8 $\Omega^{-1}\cdot cm^{-1}$ for the 0.2% and 2% In doped samples, respectively. This change in magnitude by a factor of 10 to 10^2 $\Omega^{-1}\cdot cm^{-1}$ is significant, since it not only enhances the photosensitivity by 10^5 to 10^6, but it also improves the films photoresponse.

As observed by curves [1] to [3], corresponding to the untreated and doped samples, the untreated sample once illuminated, is slow to respond in reaching a steady photocurrent (I_p) of 2.19 x 10^{-6}A. However this problem is significantly reduced by the presence of the In atoms in the CdS matrix. As seen from curves [2] and [3], the photoresponse is enhanced and is quick to obtain consistent photocurrents of 4 x 10^{-6} A and 1.53 x 10^{-5} A with negligible current fluctuation.

It addition annealing of the CdS:In samples at temperatures $\geq 220°C$ has lead to an increased photoconductivity ($\approx 0.1\ \Omega^{-1}\cdot cm^{-1}$) and stable photocurrents of $\approx 10^{-4}$ A. However, an undesirable site effect of this annealing process is the high dark currents of $\approx 10^{-5}$ A. The corresponding high dark conductivities have significantly reduced the photosensitivity by a factor of $\sim 10^{5}$, reducing the effectiveness of this material for solar cell and sensor applications.

The increased photoconductivity in CdS is most probably due to the material being n-type in nature. During the doping process In atoms, which function as donor atoms, would have diffused into the CdS matrix. In order to validate that In dopant atoms are present in the CdS lattice the "Hot Probe" method was employed. Hot probe measurements on In-doped CdS films indicated that the majority carriers were electrons, and . Hence the In-doped CdS films are n-type. The x-ray diffraction patterns ([2] and [4] of Figure 7.2) also show the presence of a (101) indium reflection at $2\Theta \approx 32.85°$ in In-doped (unannealed) films.

This newly formed extrinsic material would have additional trapping centers (E_t) to trap photogenerated holes at the negatively charged grain boundaries. While the initial increase in the photocurrent upon illumination is due to the photocarrier generation, the slowly increasing component of the photocurrent could be due to the photoenhanced mobility as a consequence of the lowering of the intergrain barrier height (band bending) (Bhushan & Sharma, 1990).

The observed photocurrent decays are slower at increasing In doping concentrations, (see curves [2] and [3] compared to the undoped films of curve [1]). It is suggested by Bhushan and Sharma (1990), that this prolonged decay time of the photo-induced mobility is due to impurity trapping centers. Since photocurrent decay is associated with the decay of photoexcited electrons, and is prolonged by electrons excited thermally by from electron traps to the conduction band, it is a likely suspect. Thus, release of trapped holes

usually results in quenching effects, and the trap depth can be calculated using a modified version of a decay law.

The improvement of photosensitivity after In doping can be explained by considering the increase in Cd and In vacancies due to the increased indium concentration. The In vacancies associated with the Cd and S vacancies lead to formation of photosensitization centers in the CdS matrix. Since the Cd and S vacancy sensitization centers are present due to lattice defects in the untreated films, the increase in photosensitivity in the film must be due to the formation of additional In vacancies in the films after doping.

8.3 Influence of Air Annealing on Photoconductive Properties

Figures 8.3 and 8.4 show the photoresponse curves for deposited and annealed films. The annealing temperatures investigated varied from 100 to 395°C and the annealing time in all cases was approximately 60 minutes. A summary of the calculations involving the determination of dark and photoconductivities (σ_d and σ_p) respectively for the various conditions is given in Table 8.2.

Table 8.2: Dark and photoconductivity parameters of Air Annealed CdS thin films

Ann. Temp (°C)	Ann. Time (min)	R_d (Ω)	σ_d (Ω^{-1} cm^{-1})	R_p (Ω)	σ_p (Ω^{-1} cm^{-1})	S (σ_p/σ_d)
As Prep	60	7.22×10^{11}	3.12×10^{-7}	3.68×10^{6}	0.0612	1.96×10^{5}
100	60	2.84×10^{10}	7.94×10^{-6}	1.80×10^{6}	0.125	1.57×10^{4}
150	60	1.47×10^{10}	1.54×10^{-5}	4.21×10^{5}	0.535	3.47×10^{4}
202	60	1.59×10^{6}	0.142	8.06×10^{4}	2.80	19.7
242	60	1.83×10^{7}	0.0124	1.87×10^{5}	1.20	97.2
360	60	4.85×10^{11}	4.65×10^{-7}	1.41×10^{8}	1.60×10^{3}	3.43×10^{3}
395	60	6.29×10^{11}	3.59×10^{-7}	4.64×10^{8}	4.86×10^{-5}	135

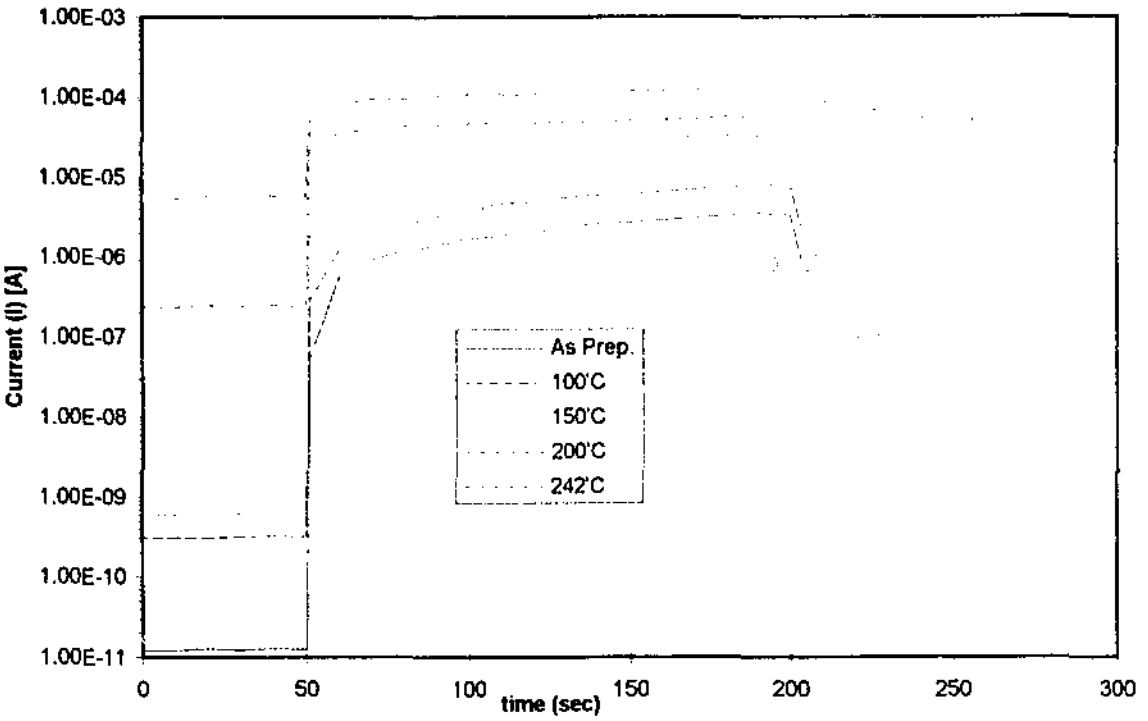

Figure 8.3: Photoresponse curves for chemically depositied CdS thin films after air annealing for 60min.

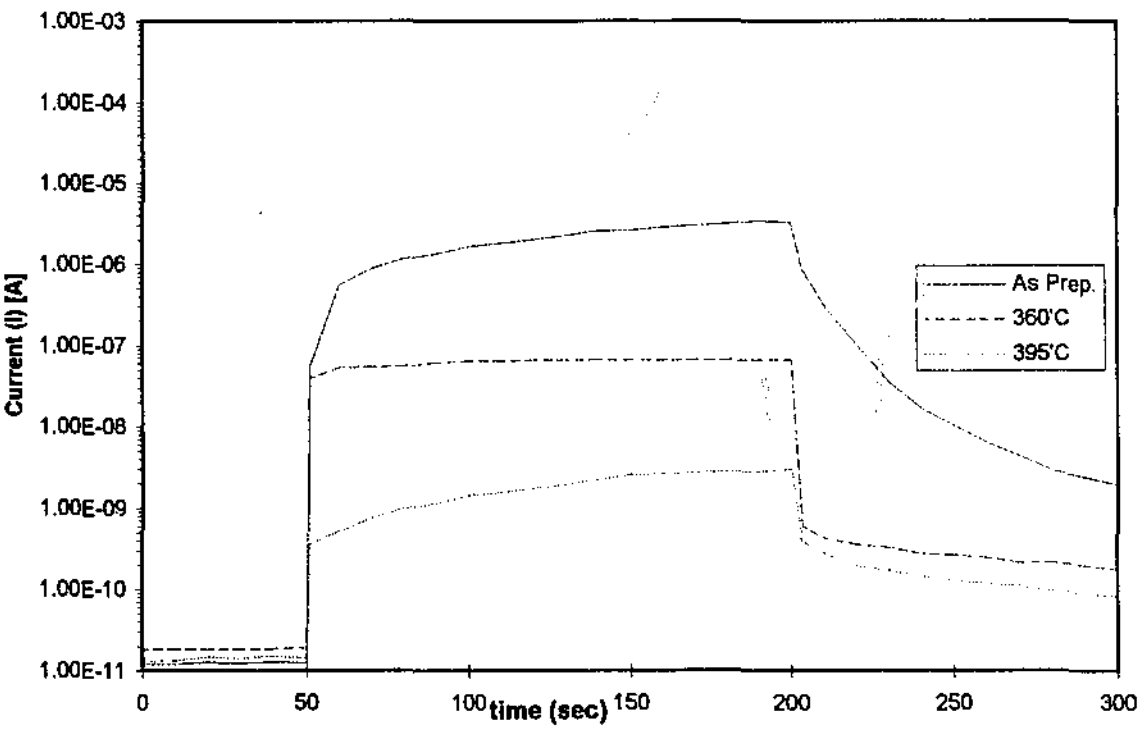

Figure 8.4: Photoresponse curves for chemically deposited CdS thin films after air annealing at temperatures T > 242°C.

As shown in Figures 8.3 and 8.4 the dark and photocurrents respectively and hence the photosensitivity of the films depends on annealing temperature. It is evident that as-deposited films and films annealed temperatures < 200°C, exhibit high dark currents and the shape of the photoresponse curves change with a prolonged photocurrent decay. However, films annealed at temperatures > 202°C have reduced photosensitivity and dark currents.

As observed from the photoresponse curves (Figures 8.3 & 8.4), annealing the films at temperatures from 100 to 395°C has had a significant impact on the dark photoconductivity. Compared to the untreated film of curve [1], the dark conductivity increases steadily from $3.12 \times 10^{-7}\ \Omega^{-1}\cdot cm^{-1}$ to a maximum in curve [2] of about $0.142\ \Omega^{-1}\cdot cm^{-1}$. This increase in magnitude of 10^5 tends to saturate at about $T \approx 200°C$. Further increases in temperature above 200°C causes a reduction in the dark conductivity characteristics, leading to a significant decrease in magnitude.

Similarly, the photoconductivity region of the curves also exhibit a change in the conductivity under illumination. The photoconductivity increases dramatically from $6.13 \times 10^{-2}\ \Omega^{-1}\cdot cm^{-1}$ for the untreated film to about $2.80\ \Omega^{-1}\cdot cm^{-1}$ at $T \approx 200°C$. Once again further increases in annealing temperature above 200°C results in the film undergoing a conductive degradation process.

Since the dark conductivity increases more rapidly than the photoconductivity counterpart (i.e. $^{\Delta\sigma d}/_{\Delta T} >> ^{\Delta\sigma p}/_{\Delta T}$), the films become increasingly photo-insensitive at annealing temperatures $T \leq 200°C$. This photosensitivity degradation process is observed in the specified range and is characterized by a decrease in magnitude of about 10^5 units. However this phenomena also undergoes an additional change, reversing at temperatures $T > 200°C$. This reversal suggests that photosensitivity could be related an impurity concentration gradients.

Curves [2] to [4] (Figure 8.3 & 8.4) show a change in the photoresponse shape and photocurrent decay as a consequence of increased temperature. As seen in curves [2] and [3], once the film is illuminated it is slow to respond in reaching a stable photocurrent of 5 x 10^{-6}A and 2.14 x 10^{-5} A, respectively. The annealed film at 200°C, corresponding to curve [4], has an enhanced photoresponse and is also quick to obtain a stable photocurrent of 1.12 x 10^{-4}A. It is also seen that the photocurrent decay times are of curves [2] to [4], corresponding to annealed films at 100, 150 and 200°C, are significantly greater that the untreated film.

Generally for the annealed films at temperatures T ≤ 200°C, the increased conductive characteristics can be attributed to structural and compositional changes.

The increased conductivity of the films in relation to film structure, can be correlated to the improved crystallinity of the film at annealing temperatures. This increase in film crystallinity after annealing is evident by observing the XRD patterns in Figure 7.1, which reveals the progressive sharpness increase of the CdS peak at $2\Theta \approx 26.5°$.
In addition, the fact that the hexagonal phase of CdS becomes increasingly prominent is also a contributing factor.

Since oxygen diffuses into the material due to the temperature it interacts with Cd vacancies that arise from lattice defects or thermal breakdown of CdS to form a conductive CdO. This compound, and reaction mechanism discussed earlier, is present within the CdS matrix. This was latter identified through x-ray diffraction in Figure 7.1, as the (200) hexagonal reflection at $2\Theta \approx 38.4°$.

Interestingly, at annealing temperatures T ≥ 242°C, curves [1] to [3] show that the dark conductivity of the films decrease. The subsequent analysis revealed it reduced from the untreated value 0.0124 $\Omega^{-1}\cdot cm^{-1}$ to 4.65 x10^{-7} $\Omega^{-1}\cdot cm^{-1}$ and 3.59 x 10^{-7} $\Omega^{-1}\cdot cm^{-1}$ for films

annealed at 360 and 395°C. This decrease in magnitude of about $\approx 10^4$ begins to saturate close to the value of the untreated film.

In addition, the photoconductivity characteristics of the film also decrease significantly from 1.20 $\Omega^{-1}\cdot cm^{-1}$ to 0.00160 and 4.86 x 10^{-5} $\Omega^{-1}\cdot cm^{-1}$ for the films annealed at 360 and 395°C. Another reproducible phenomena corresponding to the temperature increase is that the photosensitivity shows evidence of increase by a factor of $\approx$ 10 at 360°C and then a subsequent decrease at 395°C. This would imply that within the CdS matrix an impurity may have developed for T $\geq$ 242°C and was latter purged from the film through diffusion. As mentioned previously, this highlights the need for further examination using differential thermal analysis.

As indicated by curves [6] and [7], corresponding to films annealed at 360 and 396°C, the photoresponse degrades and is slow to reach a stable photocurrent of $\approx$ 6.37 x 10^{-8} A.

As the annealing temperature was increased above 100°C, the dark photoconductivity also increased. This increase in σ_d appeared to saturate at a maximum value of the order of 0.1 Ω^{-1} cm^{-1} at about 202°C. However, further increases in annealing temperature caused the σ_d to decrease to a minimum value of 10^{-7} Ω^{-1} cm^{-1} at 395°C. The apparent magnitude change in conductivity of the order or 10^6 over the temperature range supports previous works by Sebastian *et al.* (1993). In addition, this dramatic change in magnitude, due to the annealing conditions, indicates the possibility of a change in film structure and composition due to oxidation.

Generally the air annealed films displayed a quick photoresponse after annealing at temperatures about T > 360°C, a reduction in photosensitivity at higher temperatures and a very slow photocurrent decay for films with higher dark conductivities.

As a consequence of these experiments it can be deduced that, at annealing temperatures in excess of 350°C, the films become increasingly photo-insensitive. This apparent

desensitization trend is probably due to the formation of CdO and $CdSO_4$ related impurities in the air annealed films which are consistent with the observed XRD patterns.

The higher dark conductivity after annealing may be related to the chemisorbed oxygen in the grain boundaries of the film due to grain growth. It is known that impurities such as oxygen effects the band structure of the films by forming both trapping and recombination centres. It is this equilibrium between trapping and recombination centers that determines the photoresponse of the films under illumination.

As the annealing temperature was increased above 100°C, the dark conductivity and photosensitivity of the film decreased and the photocurrent decay was quicker. The quicker response of the films annealed at 360°C is related to the predominance of recombination centers over trapping centers. The general characteristic of photoconductors, that the predominance of recombination centers is associated with a reduction in the photosensitivity is supported by these experiments.

These results may be explained by a closer examination of the phase changes that occur in the film between 200 to 400°C, as indicated by the XRD results. At 200°C, owing to the predominance of conducting CdO and to a smaller extent $CdSO_4$ phase, the film is more conductive. It is these film impurities that show high dark current and slow photoresponse characteristics as a result of more trapping centers in the film owing chemical changes (see Equations [7-1] & [7-2]).

The high dark conductivity shown in chemically deposited CdS films after air annealing is useful as far as its application as a window layer in heterojunction solar cells is concerned. This helps to reduce the series of resistance of a layered solar cell structure.

9. MORPHOLOGICAL BEHAVIOUR OF CdS

9.1 FILM MORPHOLOGY AND MICROSTRUCTURE

It has been observed in the XRD patterns (Figure 7.1 & 7.2) that CdS coexists in both the hexagonal and cubic structures. The presence of different independent phases in the films as a result of different deposition times have been detected by AFM. Figures 9.10 to 10.4 present the AFM micrographs of films deposited between 20 to 80 minutes respectively. The main feature of these micrographs is the presence of two clearly different microstructures.

In Figure 9.1 we can see what is a uniform structure that covers the substrate surface. In addition, there is also an observable presence of a grain or film boundary, characterized by a dark relief or depression. This implies that there is a lattice mismatch related to the CdS film. It is this mismatch that causes a higher proportion of nucleation sites to populate this area preferentially (Auciello & Engemann, 1982).

At a deposition time of 40 minutes (Figure 9.2), we can see dispersed spherical like structures consisting of clusters of microparticles covering the initial compact layer developed at 20 minutes. These regular spherical shaped like structures show a compact nucleus and a less compact shell. In this case growth appears to be a mixed mode in which the film initially nucleates in two dimensions and, then transforms to three dimensional growth. This growth mode of CdS is in agreement with the Stranski-Krastanov nulceation growth model (Auciello & Engemann, 1982). Micrographs of surfaces deposited at times $\geq$ 40 minutes (Figures 9.3 and 9.4) clearly indicate an increasing degree of CdS grain coalescence and vertical growth.

In order to verify this trend in other concentration ranges, further in depth studies using this extremely powerful tool is recommended.

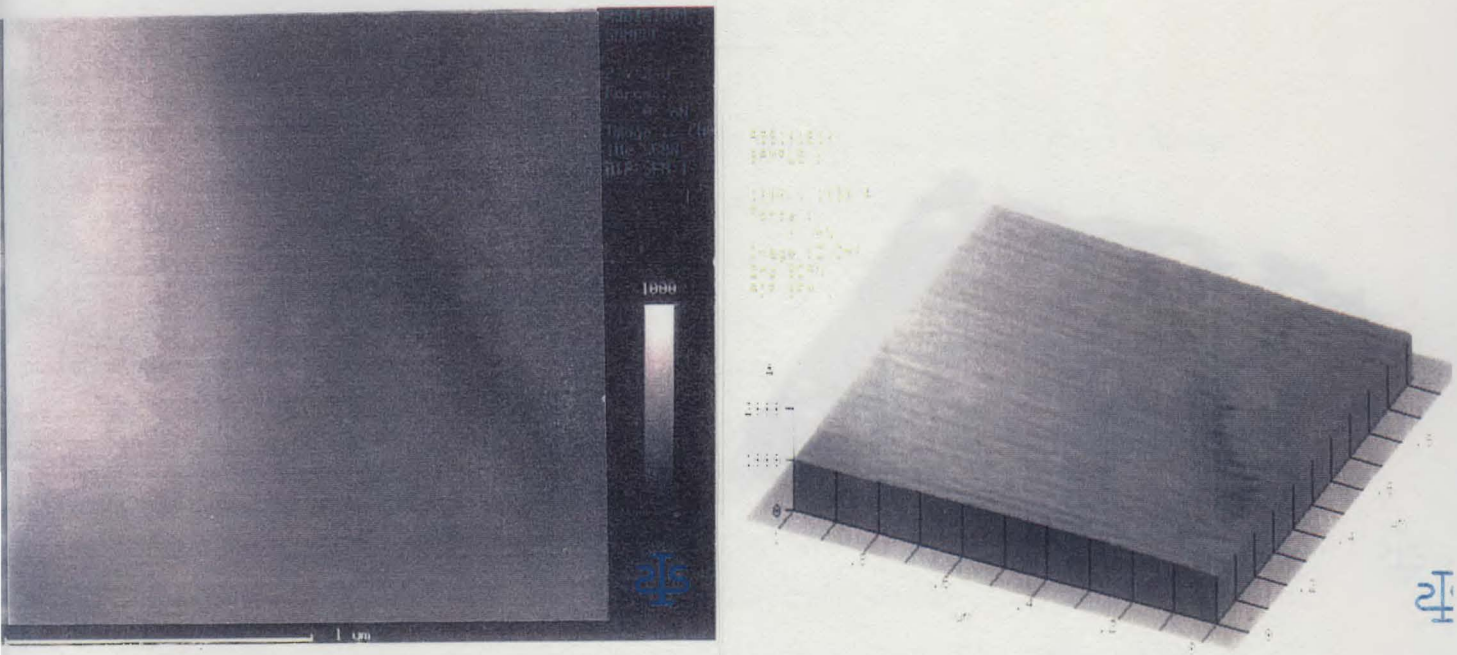

(a) (b)

Figure 9.1: (a) AFM image of CdS film deposited at 20min (scan 1.2 x 1.2 μm^2),
(b) 3 dimensional AFM image (scan 1.2 x 1.2 μm^2).

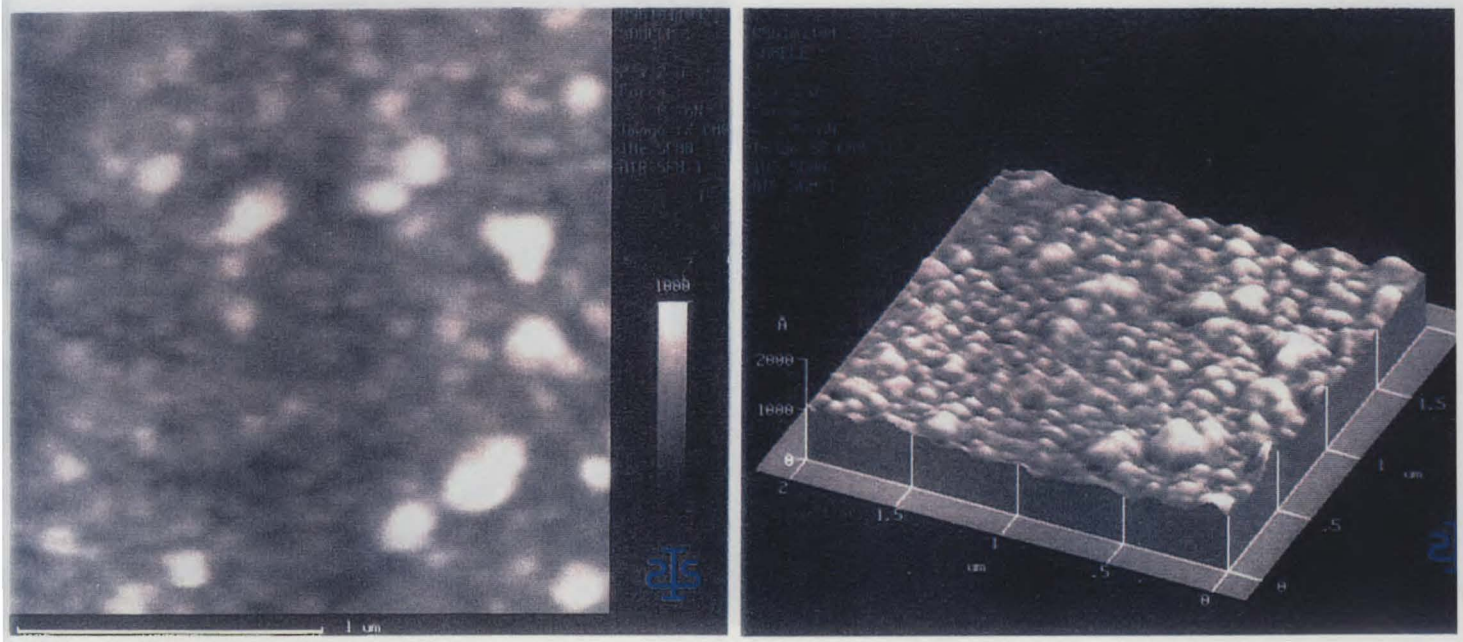

(a) (b)

Figure 9.2: (a) AFM image of CdS film deposited at 40min (scan 1.20 x 1.20 μm^2),
(b) 3 dimensional AFM image (scan 2.0 x 2.0 μm^2).

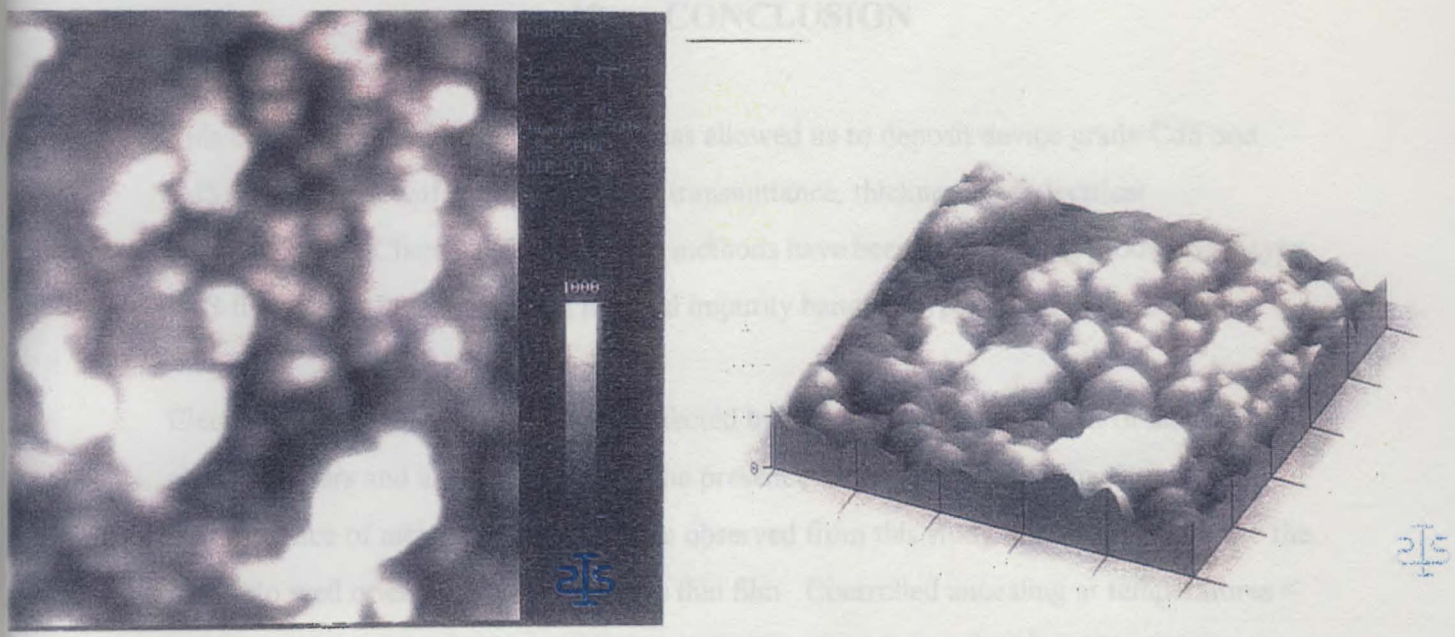

(a) (b)

Figure 9.3: (a) AFM image of CdS film deposited at 60min (scan 1.20 x 1.20 μm^2), (b) 3 dimensional AFM image (scan 1.0 x 1.0 μm^2).

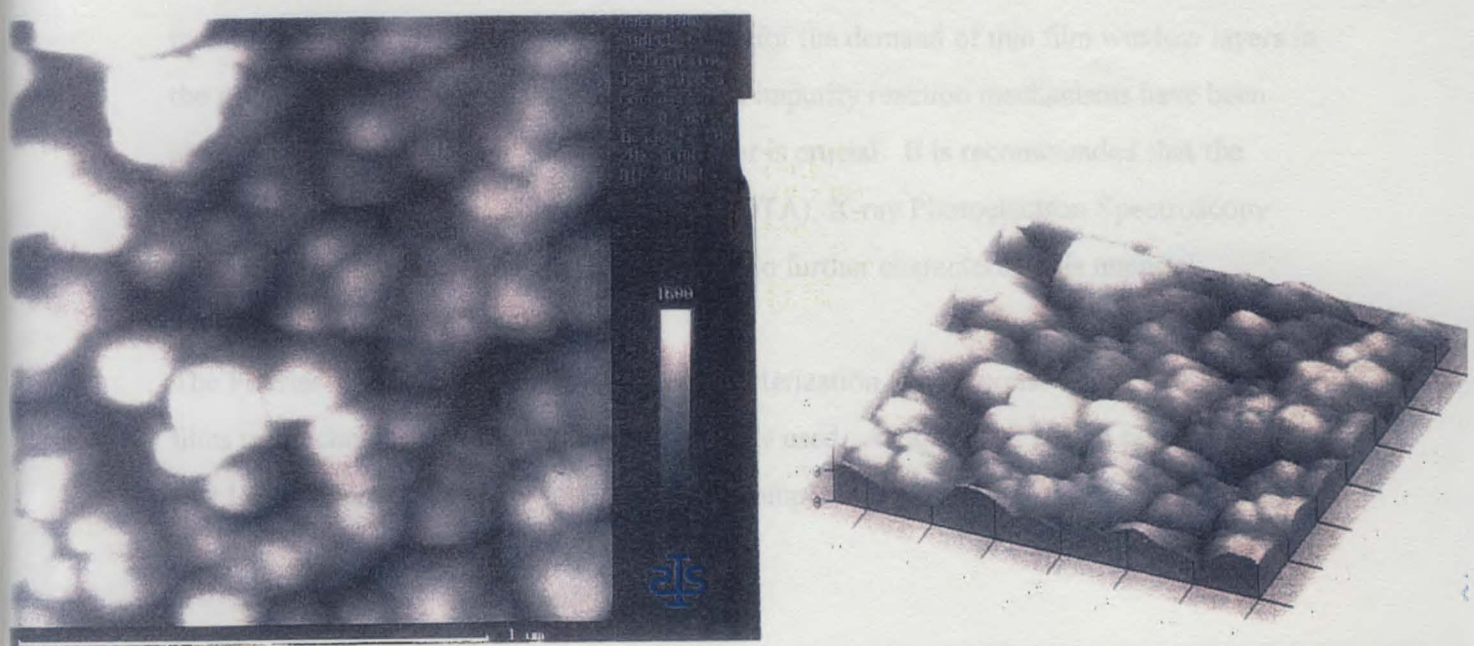

(a) (b)

Figure 9.4: (a) AFM image of CdS film deposited at 80min (scan 1.20 x 1.20 μm^2), (b) 3 dimensional AFM image (scan 1.20 x 1.20 μm^2).

10. CONCLUSION

This chemical bath deposition method has allowed us to deposit device grade CdS and CdS:In thin films with controllable film transmittance, thickness and electrical characteristics. Chemical doping *insitu* methods have been successful in producing n-type CdS films using In dopants with minimal impurity band absorption and the band edge.

Electrical properties are significantly affected by doping with In as a result of additional charge carriers and annealing through the presence of oxygen related impurity phases. The presence of metallic impurity atoms observed from this study helps to recrystallize the CdS into well orientated polycrystalline thin film. Controlled annealing at temperatures < 242°C can increase the photosenstivity of the films by a factor of 10^5 making them applicable for device applications.

We consider this form thin film deposition is compatible with any thin film device technology. This area will only grow to cater for the demand of thin film window layers in the microelectronics industry. Since probable impurity reaction mechanisms have been identified further studies of this semiconductor is crucial. It is recommended that the techniques of Differential Thermal Analysis (DTA), X-ray Photoelectron Spectroscopy (XPS) and Electron Diffraction (ED) be used to further characterize this material.

The Fourier Transform Infrared (FTIR) characterization and response of the CdS thin films is a technique that has not been previously used. As a result it is also recommended that this technique be further investigated to compliment the study.

11. REFERENCES

1. Auciello O. & Engemann J. (1992). Multicomponent and Multilayered Thin Films for Advanced Microtechnologies: Techniques, Fundamentals and Devices. NATO ASI Series., Vol. 234, pg. 9

2. Ashour, A., El-Kadry, N. & Mahmoud S.A. (1995). The Electrical an optical properties of CdS films thermally deposited by a modified source. Thin Solid Films. Vol. 269, No. 1-2 pg.117 - 120

3. Ashour, A., El-Kadry, N., Ebid, M.R., Farghal, M. & Ramadan A. A. (1996). The electrical properties of CdTe films of different preparation conditions in correlation with microstructure changes. Thin Solid Films. Vol. 279, No. 1-2 pg. 242 - 247

4. Bushan S. & Sharma S. K. (1990). Photoconductivity of chemically deposited CdS:Y films. Applied Physics Letters. Let 57 (9) pg. 884 - 887

5. Chu, T.L., Chu S.S., Schulta, N., Wang, C., & Wu, C.Q. (1992). Solution-grown cadmium sulfide films for photovoltaic devices. Electrochemical Society, Inc. Vol. 139, No. (9).

6. Boer K.W. (1990). Survey of semiconductor physics. Van Nostrand Reinhold. New York. pg. 46 - 47

7. Borges R.O. & Lincot D. (1993). Mechanism of chemical bath deposition of cadmium sulfide thin films in the ammonia-thiourea system. The Electrochemical Society, Inc. Vol. 140, No. (12)

8. Borges R.O., Froment M., Vedel J. & Lincot D. (1994). Growth mechanism and properties of chemically deposited cadmium sulfide thin films. Solid State Phenomena. Vols. 37-38, pg.492 - 502

9. Chopra K.L. & Das S.R. (1983). Thin film solar cells. Plenum Press. New York & London. pg.221 - 230

10. Chopra K.L. & Kaur I. (1983). Thin film device applications. Plenum Press. New York & London. pg.31 - 33

11. Dona J.M. & Herrero J. (1995). Chemical bath codeposited CdS-ZnS film characterization. Thin Solid Films. Vol. 268, No. 1-2 pg.5-12

12. George P. J., Sanchez, A. & Nair P. K. (196). Modification of electrical, optical and crystalline properties of chemically deposited CdS films by thermal diffusion of indium and tin. Semiconductor Science and Technology. Vol. 11, pg. 1090 - 1095.

13. Herzndez L., de Melo O., Zelaya-Angel O. & Lozada-Morales R. (1994). Electro-optical characterization of sulfur-annealed chemical bath deposited CdS films. The Electrochemical Society, Inc. Vol. 141, No. (11), pg.3239-3241

14. Jayakrishnan R., Nair J.P., Kuruvilla B.A., Kulkarni S.K., & Pandey R.K. (1996). Composition, structure and morphology of dip-coated rapid thermal annealed CdS and non-aqueous electrodeposited CdTe. Semiconductor Science Technology. Vol. 11, pg.116-123

15. Joshi N.V. (1990). Photoconductivity. Marcel Dekker, Inc. New York & Basel pg.34-8

16. Kiteav G.A., Uritskaya A.A. & Morkrushin S.G. (1965). Conditions for the chemical deposition of thin films of cadmium sulfide on a solid surface. Russian Journal of Physical Chemistry. Vol. 39, No.8, pg.1101-1102

17. Lanning B. R. & Armstrong J.H. (1992). Behavior of solution grown CdS for thin-film solar cell technologies. International Journal of Solar Energy. Vol. 12, No. 1-4, pg.247-255

18. Moller H.J. (1993). Semiconductors for solar cells. Artech House, Boston & London. pg. 17

19. Nakanishi T. & Ito K. (1994). Properties of chemical bath deposited CdS thin films. Solar Energy Materials and Solar Cells. Vol.35, pg171-178

20. Perkowitz S. (1993). Optical characterization of semiconductors: Infrared, Raman and photoluminescence spectroscopy. Academic Press, Harcourt & Company, Publishers. pg.12-21

21. Saito S., Hashimato Y. & Ito K. (1994). Efficient ZnO/CdS/InP hetergenous solar cells. Proceedings of the first World Conference on Photovoltaic Conversion. (Dec 5-9) Hawaii.

22. Sebastian P.J., Sanchez A. & Nair P.K. (1993). Modification of the dark and photoconductivity and the optical transmittance of solution-grown CdS thin films. Advanced Materials for Optics and Electronics. Vol. 2, pg.

23. Smyntyna V.A, Gerasutenko V., Kashulis S., Mattogno G. & Reghini S. (1994) The causes of thickness dependence of CdSe and CdS gas-sensor sensitivity to oxygen. Sensors and Actuaors B [Chemical]. Vol. 319, Iss.1-3, pg.464-5

24. Sebastian P.J. & Hu H. (1994). Identification of the impurity phase in chemically deposited CdS thin films. Advanced Materials for Optics and Electronics. Vol. 4 pg.407-412

25. Sebastian P.J. (1995). ZnCdS films for solar cell and photodetector applications deposited by *in situ* chemical doping of CdS with Zn. Advanced Materials for Optics and Electronics. Vol. 5, pg.269-275

26. Sebastian P.J., Hu H. & Fernandez A.M. (1995). Growth modes of solution grown CdS thin films. Advanced Materials for Optics and Electronics. Vol. 5 pg.11-17

27. Skoog, D.A. West, D.M. Holler, F.J. (1992) Fundamentals of analytical chemistry. 6th Ed. Saunders College Publishing. pg.523-528

28. Streetman B.G. (1990). Solid state electronic devices. 3rd Ed. Prentic-Hall Int., Inc. pg.56-70

29. Tepehan F. & Ozer N. (1993). A simple method for the determination of the optical constants, n and k of cadmium sulfide films from transmittance measurements. Solar Energy Materials and Solar Cells. Vol. 30, pg.353-365

APPENDIX I

```
DECLARE SUB CONVT ()
COMMON SHARED A

CLS 0
PRINT
PRINT
PRINT "    ************XRD CONVERSION PROGRAM************"
PRINT "    * PROGRAM CONVERTS 4 XRD FILES TO TWO ROWS   *"
PRINT "    * (2 THETA AND COUNTS) FOR INPUT INTO        *"
PRINT "    * EXCEL FOR PLOTTING                         *"
PRINT "    ************************************************"
PRINT
PRINT
PRINT
CALL CONVT
END

SUB CONVT
DIM X(7000)
DIM COUNT1(4000), COUNT2(4000), COUNT3(4000), COUNT4(4000)
REM*************************************************************
CLS 0
PRINT
PRINT
PRINT " THIS ROUTINE CONVERTS  XRD PATTERNS"
PRINT " WITH AN I2, I6 FORMAT"
PRINT
PRINT
REM ********************************************************
REM READ FILE NAMES AND DATA
PRINT
PRINT
INPUT " TYPE FILENAME#1(MEASURED [.DAT])"; FILE1$
PRINT
INPUT " TYPE FILENAME#2 (MEASURED [.DAT])"; FILE2$
PRINT
INPUT " TYPE FILENAME#3  (MEASURED [.DAT])"; FILE3$
PRINT
INPUT " TYPE FILENAME#4 (MEASURED [.DAT])"; FILE4$
PRINT
INPUT " TYPE IN NEW FILENAME [.ASC]"; NFILE$
OPEN FILE1$ FOR INPUT AS #1
INPUT #1, START, TEEP, SEEP
NSTEP = FIX((SEEP - START) / TEEP + 1)
FOR I = 1 TO NSTEP
X(I) = START + (I - 1) * TEEP
INPUT #1, COUNT1(I)
NEXT I
CLOSE #1
OPEN FILE2$ FOR INPUT AS #2
INPUT #2, START, TEEP, SEEP
```

```
NSTEP = FIX((SEEP - START) / TEEP + 1)
FOR I = 1 TO NSTEP
X(I) = START + (I - 1) * TEEP
INPUT #2, COUNT2(I)
NEXT I
CLOSE #2
OPEN FILE3$ FOR INPUT AS #3
INPUT #3, START, TEEP, SEEP
NSTEP = FIX((SEEP - START) / TEEP + 1)
FOR I = 1 TO NSTEP
X(I) = START + (I - 1) * TEEP
INPUT #3, COUNT3(I)
NEXT I
CLOSE #3
OPEN FILE4$ FOR INPUT AS #4
INPUT #4, START, TEEP, SEEP
NSTEP = FIX((SEEP - START) / TEEP + 1)
FOR I = 1 TO NSTEP
X(I) = START + (I - 1) * TEEP
INPUT #4, COUNT4(I)
NEXT I
CLOSE #4
FOR I = 1 TO NSTEP
COUNT2(I) = COUNT2(I) + 500
COUNT3(I) = CGUNT3(I) + 1500
COUNT4(I) = COUNT4(I) + 2500
NEXT I

REM OUTPUT FILENAME
OPEN NFILE$ FOR OUTPUT AS #5
FOR I = 1 TO NSTEP
PRINT #5, X(I); ",", COUNT1(I); ",", COUNT2(I); ",", COUNT3(I); ",", COUNT4(I)
NEXT I
END SUB
```

APPENDIX II

Symbols	Description	Units
A	Area	(cm^2)
c	concentration	(M, mol L^{-1})
e^-	electron	(C)
ξ	electric field strength	(V/cm)
E	Energy	(J, eV)
E_a	acceptor energy level	(J, eV)
E_{act}	Activation energy level	($J \cdot mol^{-1}$, $eV \cdot mol^{-1}$)
E_d	donor energy level	(J, eV)
E_f	equilibrium Fermi level	(J, eV)
E_t	trapping energy level	(J, eV)
g_i	EHP generation rate	($cm^{-3} \cdot s^{-1}$)
h	Plancks Constant	(J-s, eV-s)
$h\nu$, E_p	photon energy	(J, eV)
h^+	hole	(C)
I	current	(A)
J	current density	(A/cm^2)
k	Boltzmann Constant	(J/K, eV/K)
k	wavevector	(cm^{-1})
l , L	length	(cm)
m	mass	(Kg)
m^*	effective mass	
n_o	equilibrium e- concentration	(cm^{-3})
n	conduction band e- concentration	(cm^{-3})
n_i	intrinsic electron carrier concentration	(cm^{-3})
p	momentum	($Kg\text{-}ms^{-1}$)
p	valence band hole concentration	(cm^{-3})
p_o	equilibrium hole concentration	(cm^{-3})

q	electron charge magnitude	(C)
r_i	EHP recombination	($cm^{-3}\cdot s^{-1}$)
R, R_d & R_p	Resistance, dark and photo-resistance	(Ω)
t	mean free time between scattering	(s)
T	Temperature	(K)
x	spatial dimension	
S	Photosensitivity	
α	Absorption Coefficient	(m^{-1})
α_r	recombination coefficient	($cm^3\cdot s$)
λ	wavelength	(m, Angst)
Δx, δx	incremental change in parameter x	
δn, δp	excess electron and hole concentration	(cm^{-3})
μ	mobility	(cm^2/V-s)
ν	frequency of light	(s^{-1})
ρ, ρ_d & ρ_p	resistivity, dark & photo-resistivity	($\Omega\cdot$cm)
σ, σ_d & σ_p	conductivity, dark and photoconductivity	($\Omega\cdot$cm)
τ_n	electron recombination lifetime	(s)
τ_p	hole recombination lifetime	(s)
Φ	photon intensity	(photons/$cm^2\cdot$s)
Ψ	time dependent wavefunction	
ψ	time independent wavefunction	
$\langle\rangle$	average of enclosed variable	